HIGH-PERFORMANCE OPTOELECTRONIC DEVICES BASED ON NOVEL FUNCTIONAL MATERIALS

LIU CHUN KI

PhD

The Hong Kong Polytechnic University

2023

The Hong Kong Polytechnic University

Department of Applied Physics

High-Performance Optoelectronic Devices Based On Novel Functional Materials

LIU Chun Ki

A thesis submitted in partial fulfilment of the requirements for the degree
of Doctor of Philosophy

December 2022

CERTIFICATE OF ORIGINALITY

I hereby declare that this thesis is my own work and that, to the best of my knowledge and belief, it reproduces no material previously published or written, nor material that has been accepted for the award of any other degree or diploma, except where due acknowledgement has been made in the text.

___________________________(Signed)

_________LIU Chun Ki_______(Name of student)

Abstract

Photodetectors (PDs) transform incident optical energy into electronic signal. It has been successfully integrated into various engineering systems and applications like optical communications, environmental monitoring and scientific research. However, the traditional semiconductors and devices fail to support emerging applications such as artificial eyes and low-cost wearable electronics, mainly due to their rigidity and high fabrication cost. Intensive research effort has been put in developing next-generation semiconductors and device structures to fulfil the new requirements. Among those materials, organic-inorganic hybrid perovskites (OIHPs) and two-dimensional conjugated metal–organic frameworks (2D c-MOFs) show huge potential due to their unique physical properties.

In this thesis, high-performance PDs based on novel OIHPs and 2D c-MOFs are fabricated through solution processing. Comprehensive device measurements are provided with detailed materials characterizations. The device physics are carefully studied. Those materials include a Sn-based perovskite, a quasi-2D perovskite and two promising new 2D c-MOF materials.

A low-cost solution-processed high-performance PD based on Sn-based perovskite/organic semiconductor vertical heterojunction is developed. The device exhibits broadband response from UV to NIR. The responsivity and gain are up to 2.6×10^6 A/W and 4.7×10^6, respectively. Moreover, much faster response speed and higher detectivity can be achieved by reducing the thickness of organic semiconductor. This work opens up a window for enhancing device performance of Sn-based perovskite PDs by vertical heterojunctions.

Then, another sensitive phototransistor based on quasi-2D perovskite/single-walled carbon nanotubes (SWCNTs) have been fabricated. The high optical absorption, direct band gap nature and self-constructed gradient heterojunction of the quasi-2D perovskite synergize well with the high mobility of SWCNTs. The resultant responsivity and detectivity are as high as 2×10^6 A/W and 7×10^{14} Jones, respectively. In addition, high on/off ratio of ~103 is obtained. The promising potential of such phototransistors for next-generation PDs has been demonstrated.

Next, high-quality wafer-scale thin film of a promising 2D c-MOF, $Cu_3(HHTT)_2$ (HHTT: 2,3,7,8,12,13-hexahydroxytetraazanaphthotetraphene) is demonstrated. Its semiconducting nature and charge transport mechanism are carefully studied by various temperature direct current (DC) and frequency dependent alternating current (AC) measurements. Ultrabroadband flexible photoconductor based on $Cu_3(HHTT)_2$ is fabricated. Reliable response from UV to mid-IR can be obtained, outperforms previous solution-processed broadband PDs. The device also shows typical synaptic properties and outstanding data recognition efficiency in an artificial neural network (ANN). Furthermore, ultrathin $Cu_3(HHTT)_2$ thin films can be used as hole transporting layer (HTL) for perovskite solar cells, which significantly enhances the power conversion efficiency (PCE). This work paves the way for developing high-performance optoelectronic devices based on 2D c-MOFs.

Finally, the thin film form of another novel 2D c-MOF, $Cu_3(HHHAT)_2$ (HHHAT: Hexahydroxy-hexaaza-trinapthylene). Materials characterizations clearly show that high quality oriented thin film is obtained. Broadband PDs from UV to NIR based on $Cu_3(HHHAT)_2$ is fabricated with reliable photo-response. The field-effect modulation of channel conductivity and more importantly ferroelectric memory effect is then demonstrated through top-gated device structure for the first time. This work opens up a window for the development of high-performance (opto)electronic devices based on $Cu_3(HHHAT)_2$ thin film.

List of Publications

1. Liu, C.-K., Piradi, V., Song, J. J., Wang, Z. R., Wong, L.-W., Tan, E.-H.-L., Zhao, J., Zhu, X. J., Yan, F., 2D Metal–Organic Framework Cu$_3$(HHTT)$_2$ Films for Broadband Photodetectors from Ultraviolet to Mid-Infrared. *Adv. Mater.* **2022**, 34, 2204140.
2. Liu, C.-K., Loi, H.-L., Cao, J., Tang, G., Liu, F., Huang, Q., Liang, X., Yan, F., High-Performance Quasi-2D Perovskite/Single-Walled Carbon Nanotube Phototransistors for Low-Cost and Sensitive Broadband Photodetection. *Small Struct.* **2021**, 2, 2000084.
3. Liu, C.-K., Tai, Q., Wang, N., Tang, G., Hu, Z., Yan, F., Lead-Free Perovskite/Organic Semiconductor Vertical Heterojunction for Highly Sensitive Photodetectors. *ACS Appl. Mater. Interfaces* **2020**, 12, 16, 18769–18776.
4. Cao J., Liu, C.-K., Piradi V., Loi H.-L., Wang T., Cheng H., Zhu X., Yan F., Ultrathin Self-Assembly Two-Dimensional Metal–Organic Framework Films as Hole Transport Layers in Ideal-Bandgap Perovskite Solar Cells. *ACS Energy Letters* **2022**, 7, 3362.
5. Cheng, H., Liu, C.-K., Zhuang, J., Cao, J., Wang, T., Wong, W.-Y., Yan, F., KBF$_4$ Additive for Alleviating Microstrain, Improving Crystallinity, and Passivating Defects in Inverted Perovskite Solar Cells. *Adv. Funct. Mater.* **2022**, 32, 2204880.
6. You, P., Tang, G., Cao, J., Shen, D., Ng, T.-W., Hawash, Z., Wang, N., Liu, C.-K., Lu, W., Tai, Q., Qi, Y., Lee, C.-S. and Yan, Y., 2D materials for conducting holes from grain boundaries in perovskite solar cells. *Light Sci Appl* **2021**, 10, 68.
7. Xie, C., Liu, C.-K., Loi, H.-L., Yan, F., Perovskite-Based Phototransistors and Hybrid PDs. *Adv. Funct. Mater.* **2020**, 30, 1903907.

List of Publications

8. Wang, T., Tai, Q., Guo, X., Cao, J., Liu, C.-K., Wang, N., Shen, D., Zhu, Y., Lee, C.-S., and Yan, F., Highly Air-Stable Tin-Based Perovskite Solar Cells through Grain-Surface Protection by Gallic Acid. *ACS Energy Letters* **2020**, 5, 1741.
9. Loi, H.-L., Cao, J., Guo, X., Liu, C.-K., Wang, N., Song, J., Tang, G., Zhu, Y., Yan, F., Gradient 2D/3D Perovskite Films Prepared by Hot-Casting for Sensitive PDs. *Adv. Sci.* **2020**, 7, 2000776.
10. Ding, R., Liu, C.-K., Wu, Z., Guo, F., Pang, S.-Y., Wong, L.-W., Io, W.-F., Yuan, S., Wong, M.-C., Jedrzejczyk, M. B., Zhao, J., Yan, F., and Hao, J., A General Wet Transferring Approach for Diffusion-Facilitated Space-Confined Grown Perovskite Single-Crystalline Optoelectronic Thin Films. *Nano Letters* **2020**, 20, 2747.

Acknowledgements

The work I carried out as a PhD student in Department of Applied Physics of the Hong Kong Polytechnic University in Prof. Yan Feng's group from 2020 to 2023 contributes to the content of this thesis. I am very grateful to the Research Grants Council of Hong Kong SAR government for financial support. As a research postgraduate student, I am also thankful for various support provided by the university and my host department.

First of all, I would like to thank Prof. Yan Feng, my supervisor, for his countless supporting, advising and encouragement during my PhD study. During the study period, I often struggled in various technical and theoretical issues. Every time I seek help from him, he is always willing to guide me patiently. I learned not only the way of doing research, but also analyzing various problems with creative and critical thinking from this guidance which are very beneficial for my future life. Moreover, with the strong support from Prof. Yan, I was lucky to be awarded the Hong Kong PhD Fellowship by Research Grants Council, which allows me to focus on my study without financial stress.

Furthermore, I would like to thank the technicians in Department of Applied Physics and University Research Facilities: Dr WONG Hon Fai (Pai) for instruments training; Mr. CHAN Tsz Lam (Lam Two) and Ms. Ho Wing Man (Henrietta) for chemical ordering and lab safety management; Mr. LAM Kwan Ho (Vincent) for information technology assistance; Dr. WONG Tai Lun (Terence) and Ms. LAU Joyce for guidance and maintenance of the facilities in clean room; Dr. Hardy Lui for guidance and maintenance of the facilities in Materials Research Center. Their help greatly facilitates my research.

Acknowledgement

Many thanks to my colleagues in Department of Applied Physics, especially those in Prof. Yan's group previously and currently: Dr. Tai Qidong who impressed me with his enthusiasm and ability of conducting experiments under strict conditions; Mr. Loi Hok-Leung, with whom we always solve technical issues together; Dr. Piradi Venkatesh who provides me excellent ligands for metal-organic frameworks; Dr. Cao Jiupeng, Dr. Wang Tianyue, Dr. Zhuang Jing, Mr. Cheng Haiyang who collaboration of perovskite solar cells; and many more people whom I spend countless meaningful hours with both in and outside the laboratory.

Finally, I would like to send my sincerest gratitude to my wife, Sandy, who provides me countless love, patient and understanding during the time. I would also like to express my heartfelt gratitude to my family for their support and care during my study.

Table of Contents

Table of Contents

List of Figures

List of Figures

List of Tables

Chapter 1: Introduction

1.1 Background

PDs are exemplary optoelectronic devices that transform optical signals (energy-carrying electromagnetic radiations) into electrical signals (often in the form of photocurrents or photovoltages) based on various mechanisms.[6] For a wide range of scientific and commercial applications, including optical communication, medicinal and video imaging, space exploration, environmental monitoring, military and security, this class of optoelectronic devices serves as essential building blocks.[7] The performance of such devices are strongly rely on the functional semiconductor material to effectively absorb incident optical energy and create electron-hole pairs in the material based on photo-electric effect. After that, an internal or external electric field are used to effectively separate photo-carriers to provide an electrical output.[8] PDs based on traditional inorganic semiconductors currently dominate the commercial market in the ultraviolet (UV)-visible to near-infrared (NIR) spectrum range nowadays. For instance, GaN detects light efficiently in the UV region between 250 and 400 nm, Si responds in the visible-NIR range between 400 and 1100 nm strongly, and InGaAs as well as the related heterostructures are responsible for the NIR regime between 900 and 1700 nm.[9] Despite the success of the traditional devices in the market, they have severe limitations for emerging demands which require more advanced functionalities. First, due to the limited optical absorption coefficient and optoelectrical conversion efficiency, the devices usually need a relatively thick film to absorb enough light, which make the devices bulky and fragile so they are not suitable for emerging applications like wearable integrated systems, which require electronic devices to be flexible, stretchable and lightweight. Moreover, the large amount of materials used, and the complicated fabrication procedures heighten the overall cost.[10]

A great deal of research has been conducted to search for next-generation optoelectronic materials to fulfil the modern demand of PDs. Numerous new optoelectronic materials, including as organic semiconductors, 0D, 1D and 2D nanomaterials, were developed in recent years to serve as photoactive layers for optoelectronic devices.[11] It is undeniable that these materials, despite their unique qualities, have drawbacks of their own. For instance, 1D and 2D nanomaterials have problems with unsatisfactory uniformity and reproducibility, organic semiconductors have issues with poor thermal/long-term stability and low charge carrier mobility.[12] In order to overcome the challenges, more novel materials with all-rounded properties are desperately needed. These novel materials must exhibit properties including high optical absorption efficiency across a wide wavelength range, high charge carrier mobility, simplicity in production, solution processability and stability towards mechanical stress and moisture.

In the past few years, halide perovskites emerged as a brand-new family of ground-breaking optoelectronic materials which have huge potential for next-generation optoelectronics.[13] The huge research interest of these materials was triggered by the first report of perovskite solar cell with only less than 4% efficiency.[14] The efficiency rapidly enhanced to 11% in 2012.[15] Since then, significant research effort has been put into developing perovskite materials and solar cells as well as understanding basic material properties as well as device operating principles. Up till now, more than 25% of efficiency has already been achieved.[16] Other optoelectronic devices, such as light-emitting diodes (LEDs), semiconductor lasers, and PDs, have also shown great promise for this group of extraordinary materials in addition to their enormous success in photovoltaics.[9] This is mainly due to their appealing optoelectronic properties, including tunable bandgap, high optical absorption coefficient in the UV-NIR regime, high charge carrier motilities, and long charge carrier diffusion length.[17] More importantly, the high defect tolerance enables the thin film to be easily formed by simple solution processes, which make it particularly suitable for emerging applications.[18] In particular, halide perovskites have been extensively used in PDs with various geometries and working on a variety of operational mechanisms (such as photoconductors, phototransistors, and photodiodes).[19] Excellent device performance surpassing that of similar devices based on commercial Si and traditional photosensing materials has already been reported.[9] However, the typical perovskites still have several severe drawbacks which largely limit their further applications. For instance, the common perovskites contain a large amount of toxic Pb element, which are extremely harmful for human body and the environment. Moreover, their thin films are extremely unstable in ambient environment, which largely hinder their practical applications. In view of this, lead-free perovskites which avoids the use of Pb and quasi-2D perovskites which are much more stable are developed to tackle the problems.[20] However, the study of these materials and their optoelectronic applications, especially in PDs, are still in early stage. More in-depth research should be conducted in order to realize satisfactory device performance and understand the underlying device mechanisms.

Besides the halide perovskites, a different class of materials, known as 2D c-MOFs, are also considered as a potential candidate for next-generation optoelectronics.[21] MOFs are a significant type of porous crystalline materials in which organic ligands are interconnected by metal nodes. Due primarily to their large porosity, great specific surface area, and largely adaptable chemistry[22], they have long been regarded as attractive candidates for a variety of applications, including catalysis[23], gas sensor[24], and storage[25]. However, the low conductivity of traditional MOFs precludes them for the (opto)electronic applcations.[26] Fortunately, the newly developed 2D c-MOFs display remarkable electrical transport capabilities in addition to their distinctive qualities of ordinary MOFs, such as high porosity and tailorability of crystal structure owing to their strong in-plane conjugation and tight inter-layer stacking.[27] Despite their tremendous potential in optoelectronic applications, only a handful of research works have been conducted so far.

The above-mentioned candidates successfully fulfil many of the requirements for next-generation optoelectronic materials, but their tremendous potential has not been fully revealed. Therefore, the research on developing of high-performance PDs based on those materials is urgent.

1.2 Objectives

As mentioned above, the traditional semiconductors reach their limit in providing desired PD performance and functionalities. Novel materials and device designs are urgently demanded to fulfil the ever-growing and changing demand of people. The major motivation of this thesis is therefore to develop high-performance PDs with various functionalities based on novel functional materials, including lead-free perovskite and 2D c-MOFs. The fundamental device and material physics is studied, and the performance is optimized, by utilizing various processing technologies, characterization methods, and materials combination strategies.

Particularly, the first objective of this thesis is to develop a highly sensitive PD based on a Sn-based lead-free perovskite by a vertical heterojunction with an organic semiconductor. With the suitable hand alignment, excellent optical properties of the Sn perovskite and high mobility of organic semiconductor, much enhanced performance than controlled devices would be expected. The second objective is to fabricate a low-cost and sensitive broadband phototransistor based on quasi-2D perovskite/SWCNTs heterostructure. The unique gradient type-II heterojunction combined with strong broadband light absorption and excellent transport properties of SWCNTs would lead to superior device performance. The third objective is to study the fundamental physics, especially the thin film transport mechanisms, of a newly developed 2D c-MOF $Cu_3(HHTT)_2$ and utilizing it for applications including ultra-broadband PD, synapse, and solar cell. The study would shed light on further exploration of high-performance optoelectronics based on 2D c-MOFs. The last chapter is to develop high-quality thin film of another novel 2D c-MOFs, $Cu_3(HHHAT)_2$, and fabricate PDs as well as top-gated ferroelectric transistor based on $Cu_3(HHHAT)_2$. The high electrical conductivity of $Cu_3(HHHAT)_2$ and the use of high-k dielectric would lead to high-performance optoelectronic devices.

1.3 Outline of Thesis

The organization of this thesis is shown as following:

Chapter 1: Introduction. A brief explanation on PDs and the limitations of commercial PDs are discussed. Then, hybrid perovskites and 2D c-MOFs are introduced. The objectives and outline of this thesis are presented.

Chapter 2: Literature review. The general working mechanism of PDs is presented. After that, important parameters are listed and explained. Then, different common device designs are reviewed. Next, a brief summary on material properties and historical development of perovskites and 2D c-MOFs as well as previous effort of PDs based on those materials are given.

Chapter 3: Lead-Free Perovskite/Organic Semiconductor Vertical Heterojunction for Highly Sensitive PDs. In this chapter, comprehensive materials characterization for the Sn-based perovskite thin film and the vertical heterojunction are provided. Then the device performance is measured and the device physics are studied. Finally, flexible devices are also demonstrated.

Chapter 4: High-Performance Quasi-2D Perovskite/Single-Walled Carbon Nanotube Phototransistors for Low-Cost and Sensitive Broadband Photodetection. In this chapter, materials characterization has been conducted. Especially, the existence of vertical gradient heterostructure in the Quasi-2D Perovskite film has been confirmed. Then, the gate-voltage dependent photodetection performance is measured.

Chapter 5: 2D Metal–Organic Framework $Cu_3(HHTT)_2$ Films for Broadband PDs from Ultraviolet to Mid-Infrared. The growth mechanics of $Cu_3(HHTT)_2$ Films is discussed along with extensive material characterization. Next, the transport physics in the thin film $Cu_3(HHTT)_2$ is carefully studied. Then, ultrabroadband PDs are fabricated. Flexible PDs and optical synapses are then demonstrated. Perovskite solar cell with $Cu_3(HHTT)_2$ Film as hole transporting layer (HTL) and related first-principle simulation is also presented.

Chapter 6: 2D Metal–Organic Framework $Cu_3(HHHAT)_2$ films for broadband PD and ferroelectric memory. The $Cu_3(HHHAT)_2$ thin film is characterized carefully. Broadband PDs with response from visible to NIR are subsequently fabricated. More importantly, top-gated resistive memory effect has been demonstrated for the first time with the aid of an organic ferroelectric dielectric.

Chapter 7: Conclusions and Perspectives. In this chapter, summary of the work in this thesis is presented. Then, remaining challenges and opportunities are discussed.

Chapter 2: Literature Review

2.1 Introduction

PDs are critical sensing components in modern engineering systems. It bridges optical signal to electric current and enables various functionalities, such as optical communication, environmental monitoring, healthcare and scientific research.[20] Although such research field has been started since 1990s,[6] it still attracts tremendous research attention nowadays due to the ever-growing technological needs. The development of PDs is closely related to the evolvement of novel functional materials. The device performance of PDs is heavily driven by device design and the optoelectronic properties of the functional material(s). Depending on the type of devices and functional materials used, different performance could be achieved. To accomplish the increasing requirements of modern society, the traditional semiconductors for photodetectors need to be replaced by novel functional materials for achieving cost-effective, high-performance and multi-functional photodetectors which are wearable and flexible. Among different kinds of novel materials, OIHPs and 2D c-MOFs show the most promising potential as functional layer for next-generation photodetectors.

In this review, the device classification and their working mechanisms will be first introduced. Then, the material properties and development of novel OIHPs and related devices will be review. Next, the physical properties and evolvement of 2D c-MOFs will be discussed.

2.2 Working Mechanisms of Photodetectors

There are two major categories of PDs: thermal detectors and photon detectors.[6] Thermal detectors detect the temperature difference when optical energy is absorbed on their dark surface.

They are suitable for some specific applications like far-infrared detection. The photo detectors are on the other hand based on quantum photoelectric effect, in which a photon excites a photo-carrier and generate photo-current. Photon detectors are majority of PDs in the market nowadays and are suitable for broader applications. This thesis will focus on photon detectors based on semiconductors.

PDs are semiconductor-based devices which can detect optical signals through a series of electronic processes.[6] Generally, a PD works through the following three fundamental processes: 1) photo-carrier generation by incident optical signal, 2) carrier transport and/or multiplication by gain mechanism if any, 3) collection of photo-carriers and generate output photo-current.

The quantum photoelectric effect in semiconductor is based on a photon with sufficient energy to excite a carrier to its excited state. The relationship between wavelength and transition energy can be expressed as:[6]

$$\lambda = \frac{hc}{\Delta E} = \frac{1.24}{\Delta E\ (eV)},$$

where λ is wavelength, h is planck constant, c is vacuum light speed, ΔE is transition energy. The photo-response drops dramatically when the energy of incoming photon is less than transition energy. The transition energy is generally the band gap energy in a typical semiconductor. However, it may be the barrier height in a metal-semiconductor photodiode, energy between impurity level and one of the band edges in a PD based on extrinsic semiconductor or even the energy between highest occupied molecular orbital (HOMO) and lowest unoccupied molecular orbital (LUMO) in organic semiconductors.[6, 28] The device type and functional materials are optimized depending on the specific requirements.

2.3 Important Parameters

As will be mentioned in the coming section, different types of PDs or materials exhibit their respective advantages and disadvantages. It is therefore important to objectively quantity those performance using a series of performance indicators. PDs are usually characterized by photoresponsivity, gain, specific detectivity, response time and spectral response.

Photoresponsivity (R) is an indicator of sensitive of a PD under a given optical power. It is defined as the ratio between photocurrent and incident optical power:[29]

$$R = \frac{I_{ph}}{P_{in}},$$

where I_{ph} is photocurrent and Pin is incident optical power.

Gain (G) is a parameter which closely related to photoresponsivity and is a measurement of how many photo-carriers are generated per incident photon. It can be calculated by the following equation:[30]

$$G = \frac{Rhc}{e\lambda},$$

where e is Elementary charge.

Specific detectivity (D*) is a figure-of-merit to quantify the sensitivity of a PD and can be considered a generic performance indicator. It normalizes signal-to-noise ratio (NEP), device active area and the bandwidth (B):[9]

$$D^* = \frac{\sqrt{AB}}{NEP},$$

$$NEP = \frac{\overline{i_n^2}^{1/2}}{R},$$

where A is the active region of the PD, B is bandwidth, $\overline{\imath_n^2}^{1/2}$ is root mean square value of noise current. NEP is generally defined as the signal power which gives a signal-to-ratio of one at bandwidth of 1Hz. If the dark current is dominated by shot noise, D* can be expressed as:

$$D^* = \frac{R}{\sqrt{2e(\frac{I_d}{A})}}$$

where Id is dark current.

Response time measures the time needed for the channel current responses to incident light.[20] Rise (decay) time is usually defined as the time for photocurrent change from 10% (90%) to 90% (10%). The response time is closely related to carrier lifetime in the device. A longer carrier lifetime leads to higher photo-response but longer response time, and vice versa. Therefore, a trade-off between response and speed of a PD has to be made.

2.4 Device Classification

To accommodate various specific photodetection requirements like fast or sensitive detection, different design strategies are employed to fabricate PDs. Three major types of PDs will be introduced in this section, namely photoconductor, photodiode, and phototransistor. The schematic diagrams of three respective structures are shown in **Figure 2.1**.

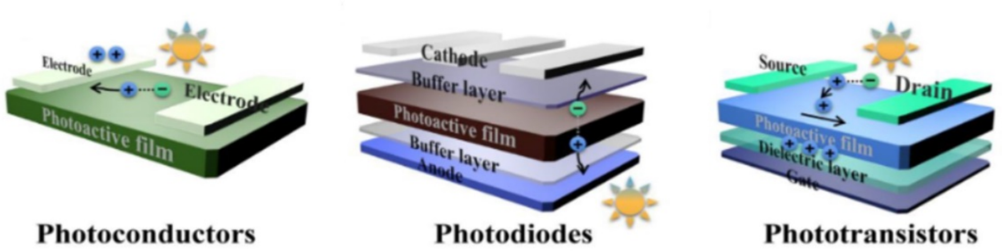

Figure 2.1. Device structures for photoconductors, photodiode and phototransistors. [1]

2.4.1 Photoconductor

A photoconductor is simply a slab of semiconductor in thin film or bulk form, with a pair of opposite ohmic contacts. When incident light falls onto the semiconductor surface, photo-carriers are generated either through band-to-band transition (intrinsic) or through transition involving impurity levels (extrinsic). It can be shown easily that the gain of a photoconductor can be expressed as:[6]

$$G = \tau(\frac{1}{t_{rn}} + \frac{1}{t_{rp}}),$$

where τ is carrier lifetime, τ_{rn} and τ_{rp} are electron and hole transit times between the two electrodes. To have a high gain, a long carrier lifetime is needed while short electrode spacing should be short and carrier mobility should be high. Notably, a gain of 1000-10^6 can be achieved in commercial devices. On the other hand, high response speed needs short carrier lifetime. A trade-off between sensitivity and response speed has to be made. Photoconductors usually exhibits much longer response time than photodiode.

When extrinsic semiconductors are used, mid-infrared or even longer wavelength detection can also be achieved without using very narrow band gap materials.

Overall, photoconductors have the advantages of simple structure, low cost and convenient fabrication, but suffer mainly from slow response speed.

2.4.2 Photodiode

Photodiode consists of a carrier depleted region where a high built-in electric field is used to effectively separate photo-generated electrons and holes.[31] For high-speed operations, the depleted region should keep thin so that a short carrier transit time is achieved. However, the depleted region must be thick to absorb more photons if a high responsivity is needed. Again, a trade-off between photo-response and speed has to be made.

For visible and near-infrared region detection, photodiode is usually operated in moderate reversed-biased such that a shorter transit time and lower diode capacitance can be obtained. Unlike photoconductors which have relatively high gain, the gain in photodiode is capped by unity due to the lack of any gain mechanism.

There are many types of photodiodes, including p-n photodiode, p-i-n photodiode, heterojunction photodiode and metal-semiconductor photodiode. They differ by how the depleted region is constructed. For instance, p-n photodiode consists of a p-n homojunction, and p-i-n photodiode consists of an additional insulator in between the p-n homojunction.

In summary, they are satisfactory candidates for high frequency and low noise applications where high sensitivity is not critical.

2.4.3 Phototransistor

Phototransistors are very similar to ordinary transistor. In phototransistors, not only electrical gate, but also the incident light can be used to modulate the channel conductivity.[9] The electrical gate can be open-circuited or applied to control the channel conductivity in addition to incident light. They are generally characterized by very high gain and gate-tunable performance.

There are two major kinds of phototransistors: photo-field-effect transistor (photo-FET) and photo-bipolar junction transistor (photo-BJT).

In photo-FETs, one kind of carriers is purposefully frozen in the device, whilst another type is free to move and contribute to photocurrent, depending on the material characteristics and device design. This is called photo-gating effect and is considered special case of photoconductive effect.[31] In the simplest case, the device structure is similar to typical FET. In this case, the channel semiconductor must simultaneously exhibit high carrier mobility, optical absorption coefficient and direct band gap. Moreover, the channel material must be a thin film so that full depletion of carriers can be achieved by applying electrical gate voltage, such that low dark current can be obtained. In some devices, there is an additional photo-absorbing layer on top of a carrier transporting layer, such that the optical and transport properties of the channel material can be decoupled.[32] However, such design requires on the other hand a type-II band alignment between the two materials to achieve the photo-gating effect.

On the other hand, photo-BJT is similar to normal BJT. It is actually a BJT without the base lead, but instead has a window and lens for incident light as well as a much wider depletion region at base-collector junction for photo-carrier generation. The photocurrent generated in the depletion region then acts as base current in normal BJT and subsequently get amplified according to the gain of the device.[6]

To sum up, phototransistors usually have very high sensitivity with easily tunable performance, but the fabrication processes are relatively complicated.

2.5 Organic-Inorganic Hybrid Perovskites

OIHPs are represented by the general chemical formula ABX_3, where A stands for an organic or inorganic cation (for example, methylammonium (MA), formamidinium (FA), cesium, or rubidium), B for a divalent metal cation (for example, lead, tin, or germanium), and X for a monovalent halide (for example, chlorine, bromine or iodine) anion.[33] They have easily tunable direct band gap, high optical absorption coefficient, superior intrinsic carrier mobility and also excellent defect tolerance (which allows them to be easily prepared by solution processes).[34] All of these properties allow them to be excellent candidate as functional material for next-generation PD. Indeed, intensive research has been done for typical perovskites. For instance, Hu and his colleagues developed a first photoconductor based on $MAPbI_3$ with a responsivity of 3.49 A/W.[35] Later, a great deal of research has been conducted to improve the device performance and understand the device physics. Lately, responsivity of 10^9 A/W, specific detectivity of 10^{16} Jones and response time of nano-second can be achieved.[9] However, the typical perovskites contain toxic lead and are very unstable in ambient air.[36]

To replace the toxic Pb in perovskites, Sn has been proposed to be the most appropriate candidate since it has the most similar properties with Pb. PDs based on Sn perovskites are still in its blooming stage. For instance, Waleed et. al reported a $MASnI_3$ photoconductor with porous aluminum template.[37] The responsivity and detectivity are only 0.47 A/W and 8.80×10^{10} Jones. Tong and his group developed a red-light photoconductor based on CsBi3I10 with a responsivity of 21.8 A/W.[38] Notably, we fabricated a high-performance photoconductor based on $FASnI_3$ with exceptional responsivity and detectivity of 10^5 A/W and 10^{12} Jones, much higher than that based on typical perovksites.[20] However, more advanced device designs like phototransistors have not been demonstrated yet, leaving a large research space for further improving the device performance.

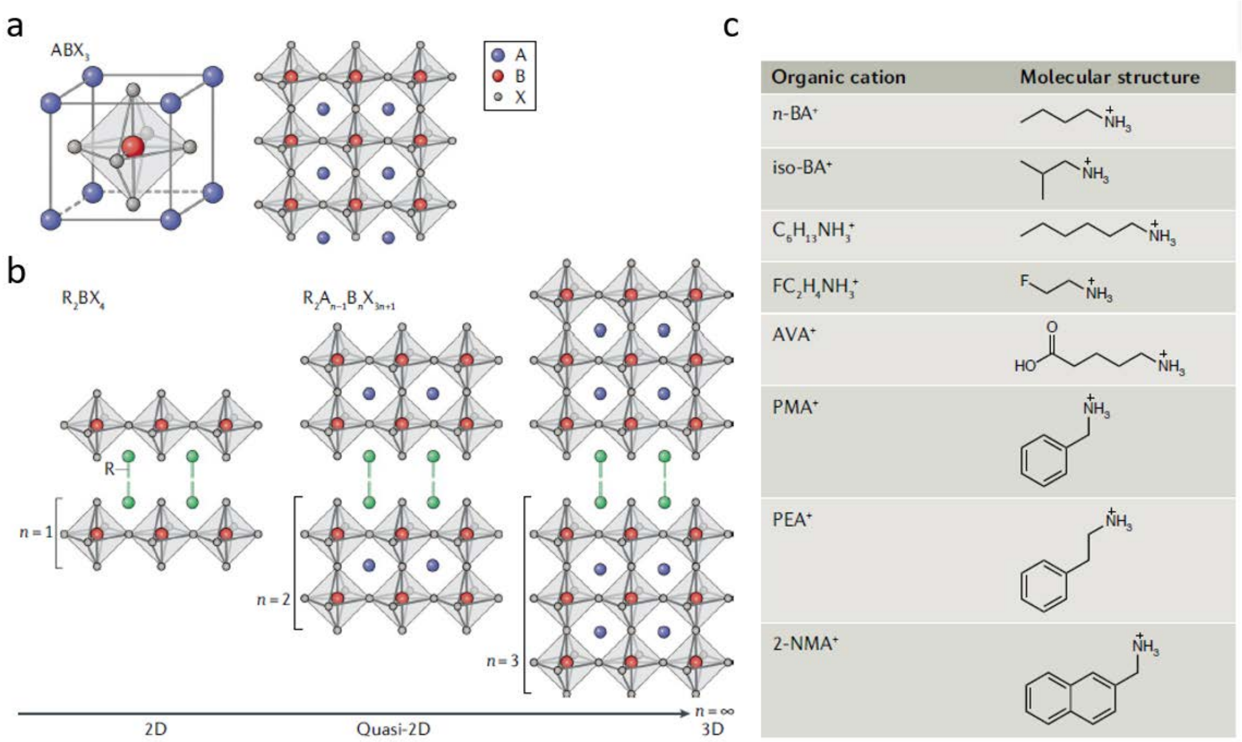

Figure 2.2. Structure of 3D and 2D perovskites. Typical crystal structure of (a) 3D perovskites and (b) 2D as well as quasi-2D perovskites. (c) Common spacer cations used in previous reports.[2]

On the other hand, quasi-2D perovskites are developed for improving the stability of perovskites. Their general formula can be expressed as $(RNH_3)_2A_{n+1}B_nX_{3n+1}$, where RNH_3 is a large organic spacer cation to encapsulate n layers of $[BX_6]^{4-}$ octahedral layers within it.[36] **Figure 2.2** shows the typical crystal structure of normal 3D perovskites and quasi-2D perovskites as well as the typical spacer cations used in previous reports. The band structure and therefore optoelectronic properties are highly dependent on the number of n. **Figure 2.3** reveals the detection range and band structure of different perovskites as well as the comparison of performance for PDs based on different novel functional materials. The air stability dramatically improved due to the encapsulation of water- and oxygen-unstable $[BX_6]^{4-}$ octahedral layers by the hydrophobic spacers. The transport and optical properties can be resolved due to the ordered arrangement of the $[BX_6]^{4-}$ octahedral layers.[39] It is also worth noting that these perovskites tend to form vertical gradient heterojunction upon spin-coating because of the relatively heavy spacer cation. Intensive research on PDs based on these perovskites are ongoing. For instance, Wang and his coworkers developed a series of $(C_4H_9NH_3)_2$ $(CH_3NH_3)_{n-1}Pb_nI_{3n+1}$ single crystal membranes for PD applications.[40] When n = 1, very low dark current and high on/off ratio of ~10^4 along with relatively low responsivity (~0.01 A/W). Shao et al. reported a $(BA)_2(MA)_{n-1}Pb_nI3_{n+1}$/graphene phototransistor ($BA^+ = CH_3(CH_2)_3NH_3^+$) with decent responsivity of ~10^5 A/W along with response time of <200ms and relatively low detectivity (~10^{10} Jones).[41] Wei et. al developed a flexible quasi-2D perovskite/indium gallium zinc oxide (IGZO) phototransistor with responsivity of ~10^5 A/W and detectivity of 10^{16} Jones.[17] Although phototransistors based on vertical heterojunctions are fabricated, low-cost solution-processable transporting layer which effectively couples with the quasi-2D perovskites is still yet to be developed, hindering the practical application of these materials.

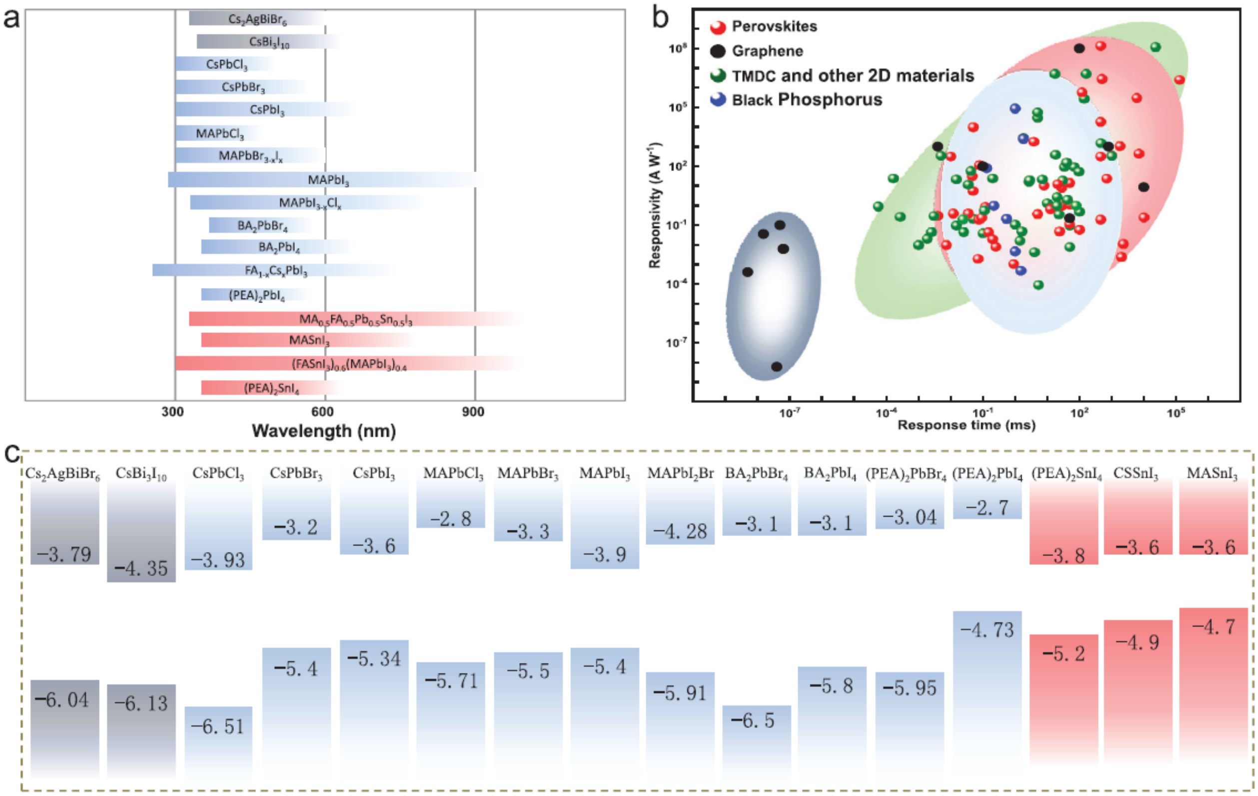

Figure 2.3. (a) Spectral range of different perovskite PDs. (b) Comparison of device performance of PDs and various 2D materials. (c) Band structures for some typical perovskites.[3]

2.6 Two-Dimensional Conjugated Metal-Organic Frameworks

MOFs have long been considered important materials for a series of applications, including electro/photo-catalysis, gas sensing and energy storage due to a number of their unique properties.[42] They are porous materials in which metal ion nodes interconnect organic ligands. Such structure grants them special properties, like high porosity, large specific surface area and extremely wide chemical tunability.[43] However, the lack of electrical conductivity in traditional MOFs significantly hinders their applications in optoelectronic devices.

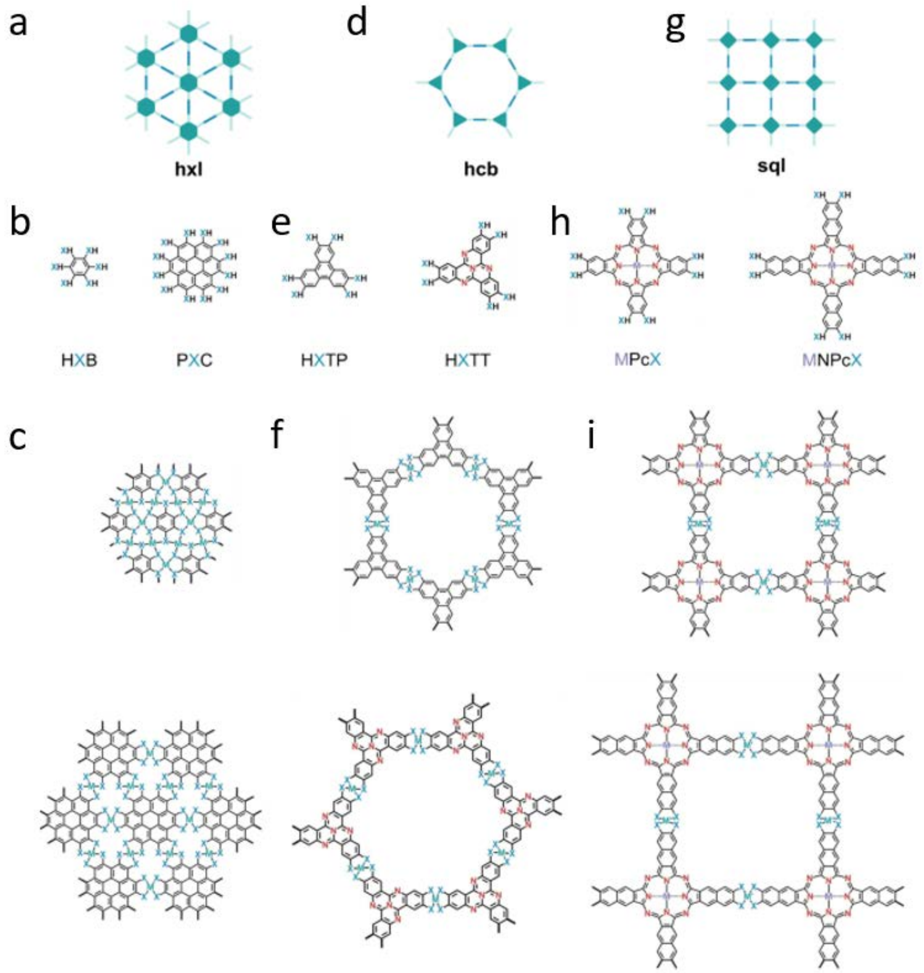

Figure 2.4. Various designs of 2D c-MOFs. (a) hexagonal lattice (hxl), (d) honeycomb (hcb) lattice, and (g) square lattice (sql). Common building blocks of 2D c-MOF networks. (b) benzene-based (HXB, X = H, A, T, and Se) and coronene-based (PXC, X = T) ligands for hxl lattice, e) triphenylene-based (HXTP, X = H, A, T, and Se) and tetraazanaphthotetraphene-based (HXTT, X = H) ligands for hcb lattice, h) phthalocyanine- (MPc(XH)$_8$, M = Fe, Ni, Cu, and Zn; X = O and NH) and naphthalocyanine-based (MNPc(XH)$_8$, M = Ni; X = O) ligands for sql lattice. The as-formed 2D c-MOFs, including c) M$_3$(HXB) (M = Cu and Ag) and M$_3$(PXC) (M = Fe, Ni, and Cu) with hxl lattice, (f) M$_3$(HXTP)$_2$ (M = Fe, Ni, Cu, Co, and so on) and M$_3$(HXTN)$_2$ (M = Cu) with hcb lattice, and (i) M'$_2$(MPcX$_8$) (M' = Fe, Ni, Cu, Co, and Zn) and M'$_2$(MNPcX$_8$) (M' = Ni, and Cu) with sql lattice.[4]

Lately, 2D c-MOFs have been developed for such applications. They not only have all the advantages of conventional MOFs like high porosity and rich chemical tailorability but also exceptional electrical conductivity. The superior electrical conductivity is primarily due to the in-plane-π-conjugation and compact interlayer π-π interaction.[44] **Figure 2.4** displays the common structure and network design of 2D c-MOFs. Most of the MOFs are synthesized in powder form by hydrothermal/ solvothermal methods, which are not compatible for optoelectronic applications.[45] To this end, various approaches have been developed to fabricate thin film 2D c-MOFs, such as liquid-liquid interface method, liquid-air interface method, face-to-face confined growth and liquid-solid layer-by-layer assembly.[4] **Figure 2.5** reveals different common fabrication methods for 2D c-MOF thin films. Layer-by-layer assembly is the most feasible method for growing large area 2D c-MOF thin film on a dielectric substrate thanks to the self-assembly feature of 2D c-MOFs on OH-functionalized surface.

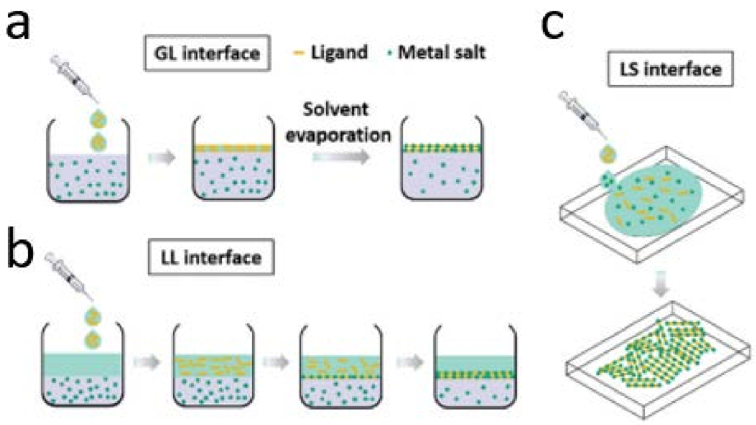

Figure 2.5. Examples of different fabrication methods for 2D c-MOF thin films. (a) Gas-liquid interface method. (b) Liquid-liquid interface method. (c) Liquid-solid interface method.[5]

Despite their huge potential, there are only very few reports on optoelectronic devices based on 2D c-MOFs up till now. Arora et al. first demonstrated a PD based on $Fe_3(THT)_2(NH_4)_3$ (THT: 2,3,6,7,10,11-triphenylenehexathiol) with broadband response from 400 to 1575nm and a detectivity of 7×10^7 Jones at 77K.[46] There are many emerging novel 2D c-MOFs which have promising physical properties in powder form synthesized through solvothermal method, but the thin film physical properties and optoelectronic device performance have not been studied yet.[5] For commercial solid state optoelectronics, thin films are the most important form of functional materials due to the feasibility of large-scale fabrication and component integration. Therefore, the study of thin film 2D c-MOFs is indeed critical for future applications.

Chapter 3: Lead-Free Perovskite/Organic Semiconductor Vertical Heterojunction for Highly Sensitive Photodetectors

In recent years, PDs based on organic-inorganic lead halide perovskites have been studied extensively. However, the inclusion of lead in those materials can cause severe human health and environmental problems, which is undesirable for practical applications. Here, we report high-performance PDs with a tin-based perovskite/PEDOT:PSS (poly-(3,4-ethylenedioxythiophene): poly(styrenesulfonate)) vertical heterojunction. The device demonstrates broadband photo-response from NIR to UV. The maximum responsivity and gain are up to 2.6×10^6 A/W and 4.7×10^6, respectively. Moreover, a much shorter response time and higher detectivity can be achieved by reducing the thickness of PEDOT:PSS. The outstanding performance is due to the excellent optoelectronic properties of the perovskite and the photo-gating effect originated from the heterojunction. Furthermore, devices fabricated on flexible substrates can demonstrate not only high sensitivity but also excellent bending stability. This work opens up the opportunity of using lead-free perovskite in highly sensitive PDs with vertical heterojunctions.

3.1 Introduction

OIHPs exhibit superior physical properties, such as high light absorption coefficient, long carrier lifetimes, suitable and tunable band gap.[47] Perovskite thin films can be prepared by low cost solution processes, which are beneficial to large-scale production.[48] Moreover, many studies indicated that flexible perovskite devices can be easily realized on plastic substrates.[35, 49] These features make OIHPs a promising candidate for next generation optoelectronic devices such as PDs (PDs), which are expected to be low-cost, high-performance and flexible. OIHPs possess a common chemical formula of ABX_3, where the monovalent A site cation can either be organic such as $CH_3NH_3^+$ (MA^+) and $(NH_2)_2CH^+$ (FA^+) or inorganic like Cs^+ and Rb^+, B denotes a divalent metal cation (e.g., Pb^{2+} and Sn^{2+}) and X represents a halide anion (e.g., Cl^-, I^- or Br^-).[50]

The first perovskite PD is based on $MAPbI_3$, which shows an initial responsivity of 3.49 A/W.[35] After that, many new methods were adopted to enhance the performance. A $MAPbI_3$ ambipolar phototransistor based on vapor-assisted solution process has developed by Li and his coworkers. The device exhibits an improved responsivity of 320 A/W.[51] Later on, hybrid structures was employed to achieve even higher responsivity. For instance, a $MAPbI_3$ nanowire/graphene hybrid phototransistor was fabricated, owing to the outstanding optoelectronic properties of perovskite, the engineered perovskite/graphene interface and high mobility of graphene, a responsivity of 2.6×10^6 A/W was obtained.[52] Our group also fabricated a PD based on a multi-heterojunction of $CH_3NH_3PbI_{3-x}Cl_x$/P3HT/graphene.[32] Upon illumination, the photo-generated holes transfer to graphene effectively, while electrons are blocked by P3HT. The reduced recombination and increased carrier lifetime leads to a very high responsivity of 1.91×10^9 A/W. Peng et al. reported a $MAPbI_3$–MoS_2 nanoflakes BHJ film/rGO phototransistor.[53] The MoS_2 flakes incorporated in the perovskite film act as electron accepter for more efficient photo-carrier separation. A responsivity of 1.08×10^4 A/W was measured. A Schottky barrier-controlled $MAPbI_{3-x}Cl_x$/black phosphorus phototransistor was recently developed by our group.[54] Owing to the pronounced photo-gating effect and a field-assisted detrapping process derived from the schottky barrier at source electrode, a superior responsivity up to 10^8 A/W along with a response time of ~10ms was obtained. Although PDs based on Pb-containing perovskites are studied widely and demonstrates excellent device performance, the high toxicity of Pb in those perovskites can severely hinder their potential for practical applications.[55] Thus, the development of high performance PDs based on lead-free perovskite is crucial.

Studies about PDs based on lead-free perovskites are very limited due to the challenge of preparing stable lead-free perovskite materials.[56] Waleed et. al presented a $MASnI_3$ nanowire-array PD by vapor phase chemical reaction method with porous alumina template, exhibiting a responsivity of only 0.47 A/W.[37] A $(TMHD)BiBr_5$ (TMHD = N,N,N,N-tetramethyl-1,6-hexanediammonium) double perovskite photoconductor was demonstrated with a low responsivity of only 0.15 A/W.[57] Qian et al. developed a flexible PD based on $(PEA)_2SnI_4$ 2D perovskite, which also exhibits a limited responsivity of 16 A/W.[49a] Yang et al. reported a PD based on $MA_3Sb_2I_9$ microcrystals with a slightly higher responsivity of 40 A/W.[58] The lead-free perovskite PDs reported so far has limited responsivity and the performance of the devices are far below the requirement of sensitive photo-detection. In addition, the concept of vertical heterojunction has not been employed to these devices, which are important for achieving ultra-high performance and multi-functional devices. Therefore, studies about this issue are urgently needed for developing ultrahigh-performance lead-free perovskites PDs.

Here, we report a lead-free perovskite PD based on a vertical heterostructure of $FASnI_3$ and PEDOT:PSS. Due to the photo-gating effect, the device demonstrates outstanding photo-response over a broad range of wavelength from 300nm to 1000nm. The maximum responsivity and gain of the device are 2.6×10^6 A/W and 4.7×10^6 respectively. In addition, shorter response time and higher detectivity can be obtained by decreasing the thickness of PEDOT:PSS layer. Besides, this PD can be assembled as a flexible PD on a polyimide (PI) substrate. The flexible PD exhibits excellent bending stability as well as high photo-response. This study paves the way for the further development on environmental-friendly PDs with ultrahigh performance.

3.2 Results and discussion

3.2.1 Working Mechanisms

Figure 3.1a shows the schematic diagram of the device. The PD is based on a vertical heterojunction of $FASnI_3$ and PEDOT: PSS. $FASnI_3$ has moderate band gap which enabling broadband detection and suitable band positions for forming type-II heterojunction with PEDOT:PSS. The perovskite layer is used as a light absorbing layer while PEDOT:PSS film is adopted as an efficient charge transport layer. **Figure 3.1b** illustrates the corresponding energy level diagram. A type-II band alignment is obtained for the perovskite/PEDOT:PSS heterojunction. Upon incident light, electron-hole (e-h) pairs and excitons are generated in the perovskite film. Due to the low exciton binding energy of perovskite, excitons would dissociate into e-h pairs rapidly.[59] The photo-generated holes would then diffuse into PEDOT:PSS since the highest occupied molecular orbital (HOMO) of PEDOT:PSS has lower energy than valence band maximum (VBM) of perovskite for holes.[60] On the other hand, the electrons would be locked in the perovskite because the lowest unoccupied molecular orbital (LUMO) of PEDOT:PSS is much higher than the conduction band maximum (CBM) in perovskite for electrons. The diffusion of photo-carriers is typically fast enough so that the lateral carrier transport in the light absorbing layer can be neglected.[61] Due to the efficient carrier separation achieved by the vertical built-in electric field at perovskite/PEDOT:PSS interface, the carrier lifetime could be significantly increased. In addition, the hole mobility of PEDOT:PSS is much higher than that of the underneath perovskite films.[49c, 62] Thus, holes transport in PEDOT:PSS channel for multiple times before recombining with electrons being trapped in perovskite, leading to a high gain and responsivity.

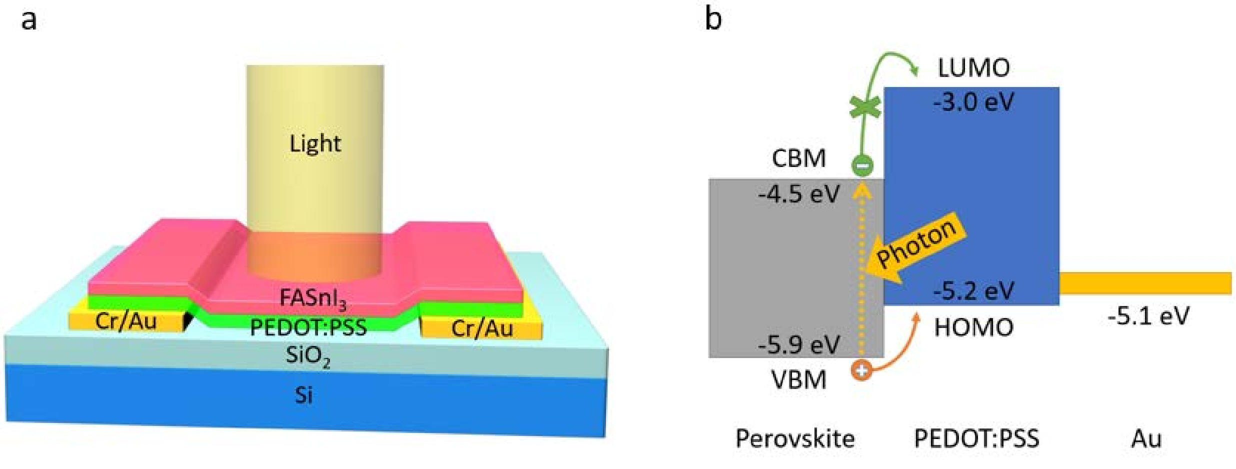

Figure 3.1. Device schematics and material characterizations. (a) Schematic diagram of the $FASnI_3$/PEDOT:PSS PD. (b) Relative energy band diagram of the PD and illustration of carrier transfer mechanism in it.

3.2.2 Materials Characterization

To reveal its optical properties, $FASnI_3$ perovskite films were characterized by photo-luminescent (PL) and Ultraviolet-Visible (UV-Vis) spectroscopy. **Figure 3.1c** displays the corresponding spectrums. As expected, the absorption spectrum displays a sharp rising edge near 890nm. the PL peak also occurs around the same position. These results indicate that the band gap of the $FASnI_3$ is ~1.4 eV, which is consistent with that reported in literature.[63] To obtain the structural information, a $FASnI_3$ perovskite film on glass substrate was also characterized by X-ray diffraction (XRD), as shown in **Figure 3.1d**. The XRD pattern indicates that the perovskite is in α-phase of Orthorhombic structure, with lattice parameters a = 6.33 Å, b = 8.96 Å, c = 8.95 Å, which is the desirable phase for PDs.[47c] Scanning Electron Microscopy (SEM) was also employed to study the surface morphology and estimate the thickness of each layer. As displayed in **Figure 3.1e** and **3.2**, the grain size for perovskite film coated on PEDOT:PSS is ~200nm, while that coated on SiO_2/Si is ~500nm. This can be attributed to the higher wettability of the perovskite precursor solution on the PEDOT:PSS surface than on the SiO_2/Si.[64] The smaller grain size here should not severely affect the device performance since the photo-generated holes in perovskite transport to PEDOT:PSS vertically and the photo-current contributed by electrons in perovskite is negligible. The cross-sectional SEM image (**Figure 3.1f**) reveals that the thicknesses of perovskite films are ~80nm. On the other hand, the thicknesses of PEDOT:PSS films were measured by surface profiler. The thickness of the PEDOT:PSS layer is controlled to be 30 nm unless otherwise specified.

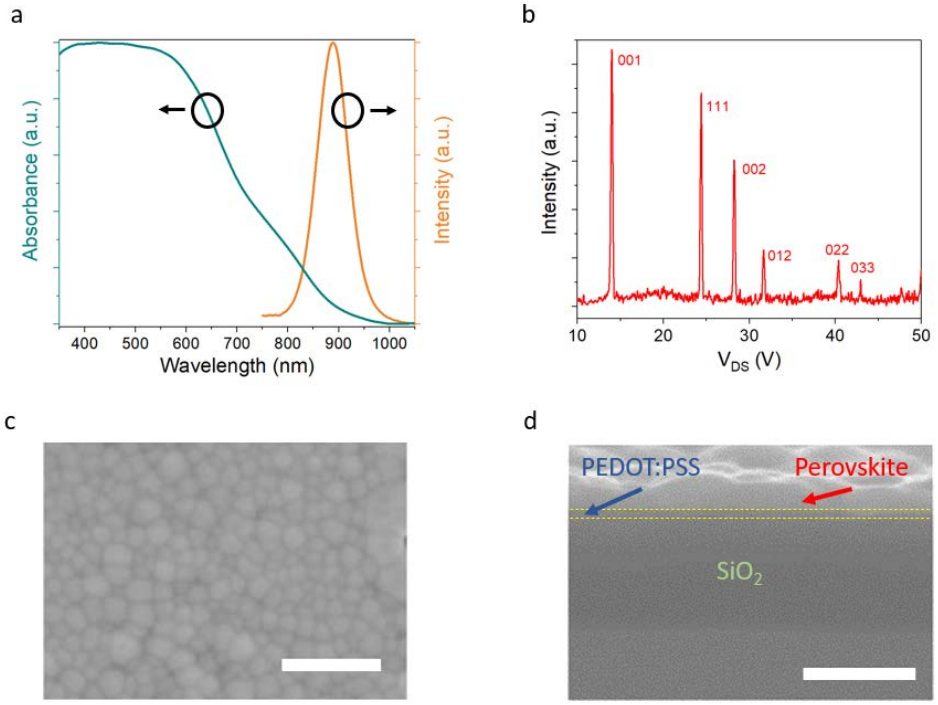

Figure 3.1. (a) PL and absorption spectra of perovskite film. (b) XRD pattern of the perovskite film. (c) SEM image of a $FASnI_3$ film coated on PEDOT:PSS. (Scaler bar: 1 μm) (d) Cross-sectional SEM image of a $FASnI_3$/PEDOT:PSS bilayer coated on SiO_2/Si. (Scaler bar: 300 nm)

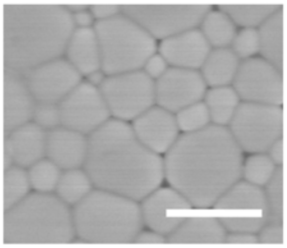

Figure 3.2. SEM image of perovskite surface for a film coated on SiO_2/Si. (Scaler bar: 1 μm)

3.2.3 PD Performance

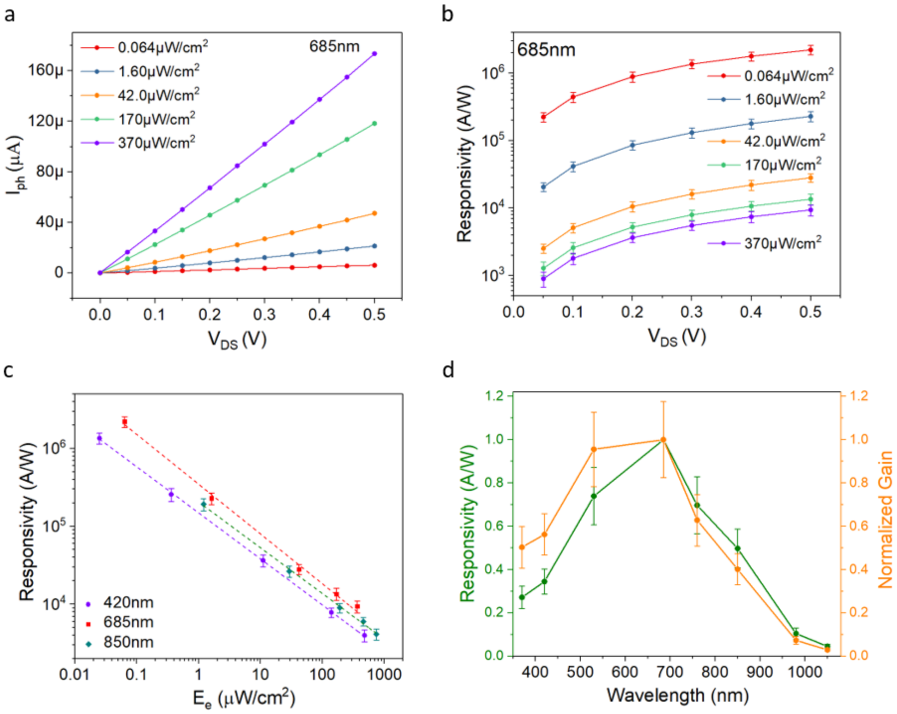

Figure 3.3. Device performance of a $FASnI_3$/30 nm-PEDOT:PSS PD. (a) Photo-current vs. drain voltage and (b) average responsivity vs. drain voltage under various intensity of light. Wavelength: 685nm. (c) Average responsivity as a function of light intensity for three different wavelengths. The dashed lines are fitting curves using equation (3). (d) Average normalized spectral responsivity and gain of the PD. Error bar was calculated from the standard deviation.

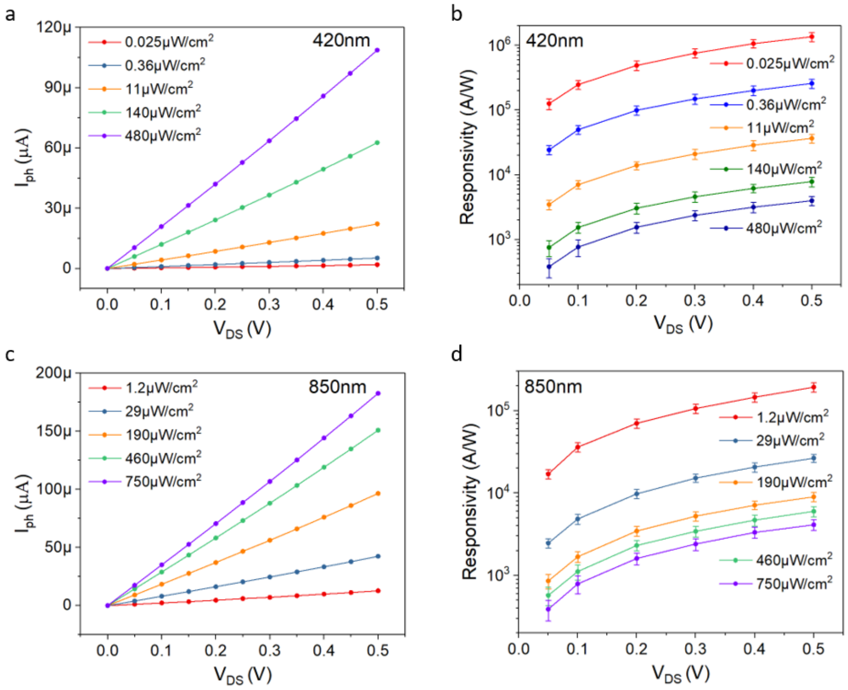

Figure 3.4. Supplementary device performance of the $FASnI_3$/30 nm-PEDOT:PSS PD. (a) Photo-current vs. drain voltage and (b) average responsivity vs. drain voltage under various intensity of 420nm wavelength light. (c) Photo-current vs. drain voltage and (d) average responsivity vs. drain voltage under various intensity of 850nm wavelength light. Error bar indicates the standard deviation.

Figure 3.3a shows the photo-current as a function of drain voltage under various light intensities for a $FASnI_3$/30 nm-PEDOT:PSS device. The wavelength of the light is 685nm. At different light intensities, the photo-current increases linearly with applied bias voltage. This means that ohmic contact is obtained in the device. It is observed that the transistor transfer characteristics cannot be measured, which could be due to the dipole disorder and gate screening from surface charge-trapping sites. Further study of interfacial properties using transmission electron microscopy (TEM) and computer simulation would lead to more insight, like surface energy and interface binding energy.

Responsivity is one of the most important parameters to quantify the photo-response. **Figure 3.3b** displays the responsivity as a function of drain voltage. The maximum responsivity of the device is 2.6 × 10^6 A/W, which is the highest among PDs based on lead-free perovskites reported so far.[20, 37, 49a, 57-58] The photo-current and responsivity of the same device under light with wavelengths of 850nm and 420nm are presented in **Figure 3.4**. Actually, such responsivity value is even higher than or comparable to many PDs based on Pb-containing perovskites employing vertical heterojunctions.[41, 52, 65] The highest gain is 4.7 × 10^6. Such high gain can be attributed to the photo-gating effect induced by the $FASnI_3$/PEDOT:PSS type-II heterojunction.

The relationship between responsivity and light intensity for three different wavelengths of light are shown in **Figure 3.3c**. Notability, the responsivity of the device exponentially decays with increased illumination intensity according to a relation:[66]

$R \propto E_e^{\alpha}$,

where α is fitting constant which is typically negative. Because high light intensity dramatically increase photo-carriers accumulated in perovskite film, the high density of accumulated carriers greatly increases the recombination rate in perovskite layer before the holes can transfer to PEDOT:PSS, leading to the lower responsivity.

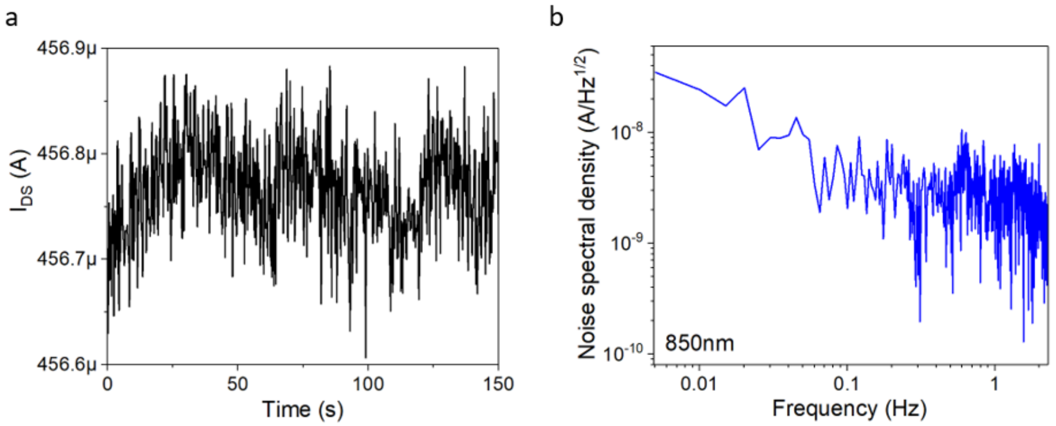

Figure 3.5. Noise measurement and analysis of a perovskite/30-nm PEDOT:PSS PD. (a) Current as a function of time in dark. (b) Analysis of noise spectral density of the device based on the FFT of the dark current noise.

Detectivity is also an important parameter for PDs. To obtain NEP of the PD, the time domain noise current was measured (**Figure 3.5a**). Subsequently, Fast Fourier Transform (FFT) was performed to acquire the noise spectral density as a function of frequency (**Figure 3.5b**). The noise current at bandwidth of 1Hz can be found to be 2.9 nA. The corresponding NEP is 8.4×10^{-14} W/Hz$^{1/2}$. A detectivity of 3.2×10^{12} Jones can be therefore calculated, which is comparable to or higher than many other perovskite-based PDs.[41, 65b, 67] As will be discussed later, the detectivity can be further improved.by reducing the PEDOT:PSS thickness in the device.

Another key concern for PDs is their spectral photo-response. **Figure 3.3d** shows the spectral responsivity and gain. The PD exhibit broadband photo-response from UV to NIR. Notably, there is an obvious extension of photo-response for wavelength beyond bandgap (>890nm), which can be attributed to light absorption by the trap states in the bandgap.[68] These trap states are originated from the detects within the perovskite crystals or at the grain boundaries. Electrons are activated by NIR photons from the valence band to the traps states of the perovskite film and generate holes that transfer to PEDOT:PSS. Since the perovskite layer has abundant deep states, significant amount of photons with energy smaller than band gap can still be absorbed and converted to photo-carriers.[49c] Similar effect has been reported before in some perovskite-based lateral PDs.[20, 49c]

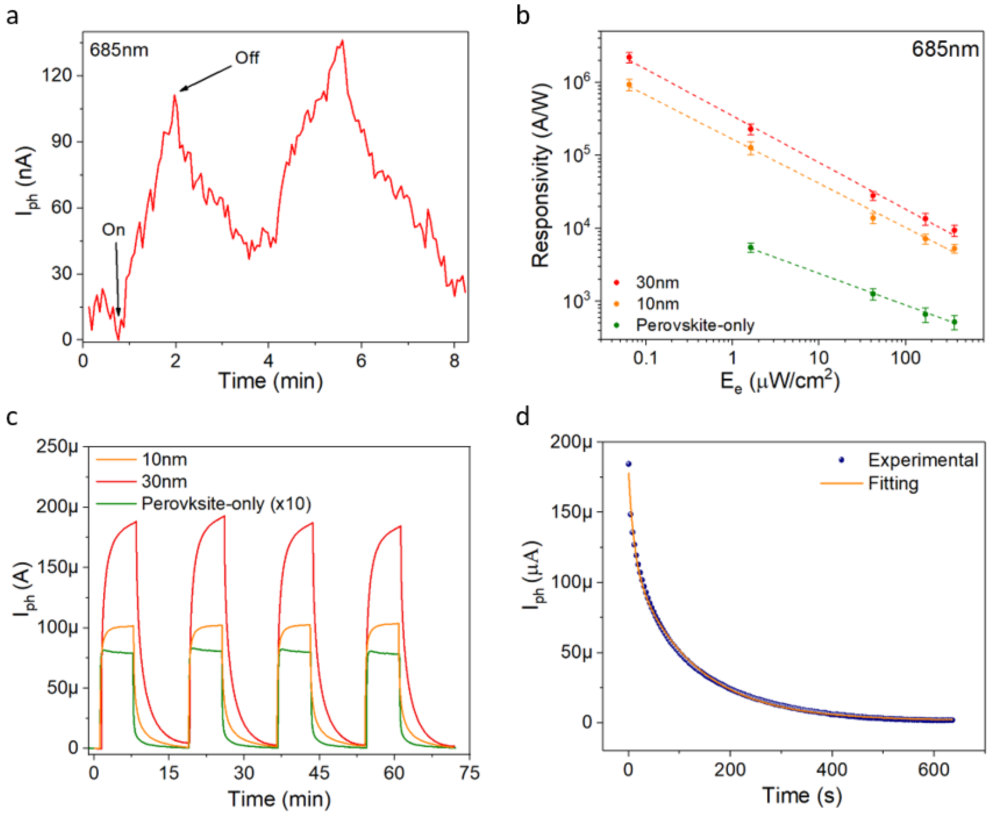

Figure 3.6. (a) Temporal response of PEDOT:PSS device under two on-off illumination cycle of 685nm wavelength light with 370 μW/cm^2. (b) Average responsivity as a function of light intensity of light with 685nm wavelength for FASnI$_3$/PEDOT:PSS with different PEDOT:PSS thicknesses and perovskite PD. Error bar represents the standard deviation. The dashed lines are fitting curves using equation (3). (c) Temporal response for various FASnI$_3$/PEDOT:PSS and FASnI$_3$ PDs under four illumination on-off cycles. (d) enlarged view and fitting of falling edge of the temporal response of the FASnI$_3$/30-nm PEDOT:PSS device.

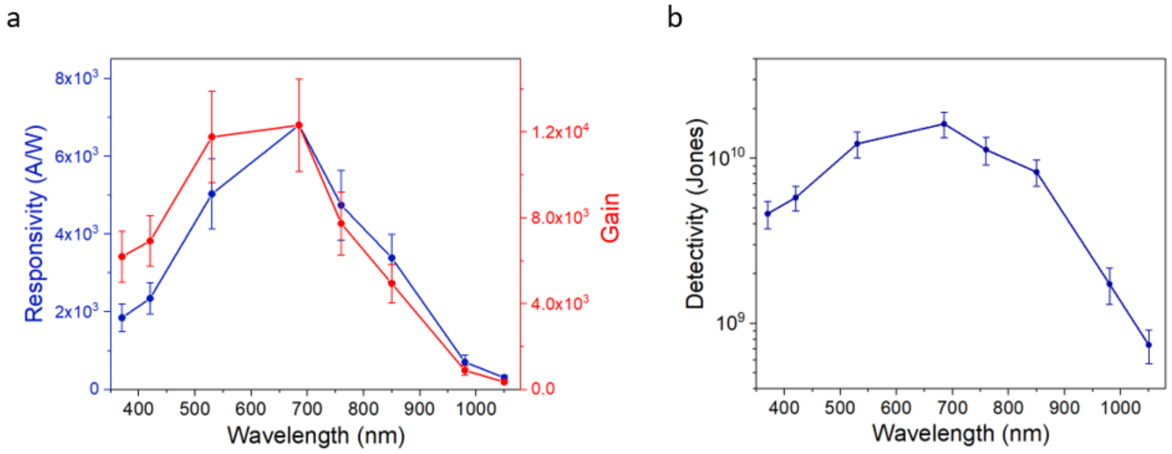

Figure 3.7. (a) Average spectral responsivity and gain as well as (b) detectivity in real scale for a perovskite/30-nm PEDOT:PSS PD. Intensity used for the measurement is ~500µW/cm^2. Error bar represents the standard deviation.

Table 3.1. Device performance of perovskite/PEDOT:PSS PDs with different PEDOT:PSS thicknesses and perovskite-only PDs. Three devices for each conditions were characterized.

Device structure	R (10^6 A/W)	D* (10^{12} Jones)	Rise/Fall time (s)
#1 Perovskite/10 nm-PEDOT:PSS	1.1	9.6	48/169
#2 Perovskite/10 nm-PEDOT:PSS	0.91	8.4	59/182
#3 Perovskite/10 nm-PEDOT:PSS	0.77	7.3	41/153
#1 Perovskite/30 nm-PEDOT:PSS	2.6	3.2	128/226
#2 Perovskite/30 nm-PEDOT:PSS	2.2	4.3	115/205
#3 Perovskite/30 nm-PEDOT:PSS	1.9	3.6	107/188
#1 Perovskite	0.0063	0.22	9/61
#2 Perovskite	0.0054	0.29	11/71
#3 Perovskite	0.0047	0.19	8/57

To verify the role of the heterojunction, control devices with only PEDOT:PSS or perovskite layers are characterized. As displayed in **Figure 3.6a**, the PEDOT:PSS device demonstrated a photo-current of only ~100nA, which is several orders of magnitude lower than the bilayer device under the same light intensity. The control device with only a perovskite layer also shows a much lower responsivity than the device with the vertical heterojunction (**Table 3.1**). Therefore, the high photo-response is not contributed solely by the organic semiconductor or the perovskite layer. To have a more comprehensive understanding on the hybrid PD, we fabricated devices with a thinner PEDOT:PSS layer (~10nm). The performance of the devices is listed in **Table 3.1**. The detectivity is improved up to 9.6 × 10^{12} Jones due to the decreased noise level.

Table 3.2. Mean and standard deviation (Mean ± SD) of the performance parameters for different devices.

Device structure	R (10^6 A/W)	D* (10^{12} Jones)	Rise time (s)	Fall time (s)
Perovskite/10 nm-PEDOT:PSS	9.3 ± 0.17	8.4 ± 1.2	49 ± 9.1	168 ± 15
Perovskite/30 nm-PEDOT:PSS	2.2 ± 0.35	3.7 ± 0.56	117 ± 11	206 ± 19
Perovskite	0.0055 ± 0.00080	0.23 ± 0.051	9 ± 1	63 ± 7

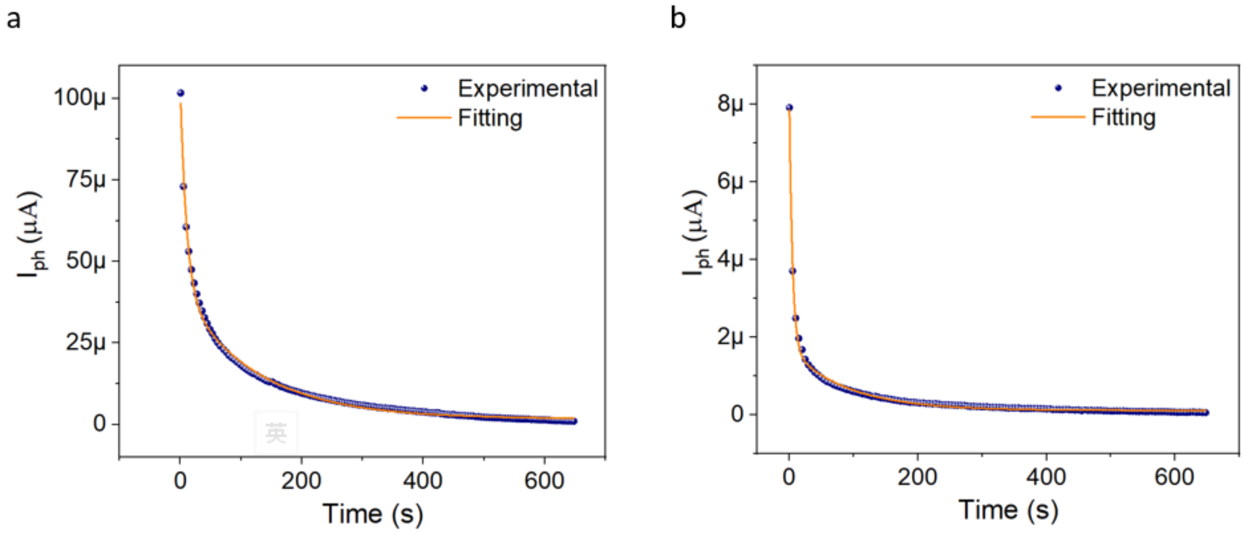

Figure 3.8. Enlarged view and fitting of falling edge of the temporal response of a (a) perovskite/10-nm PEDOT:PSS PD and (b) perovskite-only device.

Table 3.3. Falling times for representative perovskite/PEDOT:PSS and perovskite devices.

Device structure	τ_1 (s)	τ_2 (s)
Perovskite/10 nm-PEDOT:PSS	9	110
Perovskite/30 nm-PEDOT:PSS	11	130
Perovskite	5	90

Figure 3.6b shows responsivity as a function of light intensity for the devices with different PEDOT:PSS thicknesses and pure perovskite. The devices for each condition are measured and represented by the data points with error bars. It can be found that the responsivity is enhanced by at least two orders after introducing PEDOT:PSS as a transporting layer. Such improvement is due

to the synergetic effect of the vertical heterojunction that leads to a photo-gating effect of the devices. The devices with 10 nm-thick PEDOT:PSS show relatively lower responsivity than that with 30nm-thick PEDOT:PSS.

Figure 3.6c shows the transient behavior of three types of devices measured at the same condition. Notably, the response time reduces with the decrease of PEDOT:PSS thickness (See **Table 3.1**), which can be attributed to more rapid carrier recombination in a thinner device. With the same light intensity, thinner PEDOT:PSS film should have higher carrier density and the balance between hole injection and recombination thus occurs earlier, leading to a lower responsivity and a shorter response time.[49c] The transient behavior can be fitted with a double exponential falling function:

$$I_{ph} = A_1\, exp\left(-\frac{t}{\tau_1}\right) + A_2\, exp\left(-\frac{t}{\tau_2}\right),$$

where τ_1 and τ_2 are fast and slow time constants and A_1 and A_2 are magnitudes for the two decay components. As shown in **Figure 3.6d** and **Figure 3.8**, the falling process can be fitted very well with equation (6). The falling times of the PDs are extracted and shown in **Table 3.3**. The short falling time in the first stage is due to the rapid recombination of the photo-carriers under built-in electric field by accumulated carriers. After that, recombination of remaining carriers was slowed down for decreased built-in electric field. For a thinner film, more rapid recombination of carriers occurs since most of the holes are near the vertical heterojunction, causing a shorter falling time.

The trade-off between gain and response time of the device can be reflected by gain-bandwidth product (GBP) given below:[69]

$$GBP = G \times f_{3dB},$$

$$f_{3dB} \approx \frac{0.36}{\tau_r},$$

where f_{3dB} and τ_r are the 3dB bandwidth and rise time from 10% to 90% of saturated photo-current. The maximum GBP for the hybrid PDs with PEDOT:PSS thicknesses of 10nm and 30nm are 15kHz and 14kHz, while that for the perovskite-only device is 0.4kHz. The much higher GBPs for the hybrid PDs than the perovskite-only device once more indicate the overall performance enhancement brought by the PEDOT:PSS transporting layer. Although the values of GBP for our hybrid devices are relatively low compared with some high-performance PDs, they are already higher than many perovskite-based PDs.[70]

For a phototransistor, the gain is given by $G = \frac{\tau_r}{L/\mu_h E} = \frac{\tau_r \mu_h V_d}{L^2}$, where μ_h is the hole mobility in PEDOT:PSS, E is the electric field in the channel and V_d is the drain voltage.[6] Thus the GBP is given by: $GBP = 0.36\frac{\mu_h V_d}{L^2}$. So it is reasonable to find that the value of GBP is not related to the thickness of the PEDOT:PSS layer. To further improve the GBP value, we can increase the drain voltage V_d or decrease the channel length L of the device. On the other hand, the incorporation of an organic semiconductor layer with a high hole mobility in the device can result in a higher GBP of the device.

3.2.4 Flexible PD Performance

In recent years, flexible optoelectronic devices have attracted much attention due to many potential applications, such as artificial eyes and sensory skins.[71] To fully demonstrate the potential of the perovskite/PEDOT:PSS PD, a flexible device was fabricated on a PET substrate. **Figure 3.9a** shows the photo-current vs. bias voltage under different light intensity for 685nm wavelength. **Figure 3.9b** displays the responsivity as a function of drain voltage under various light intensity before and after bending test. **Figure 3.9c** shows the responsivity vs. light intensity under fixed applied voltage of 0.5V before and after a bending test. The maximum responsivity of the flexible is measured to be ~8.7× 10^5 A/W, which is comparable to the device prepared on a rigid substrate. The slightly lower photo-response of the flexible device than that on SiO_2/Si may be due to the lack of back-scattered light from the substrate.

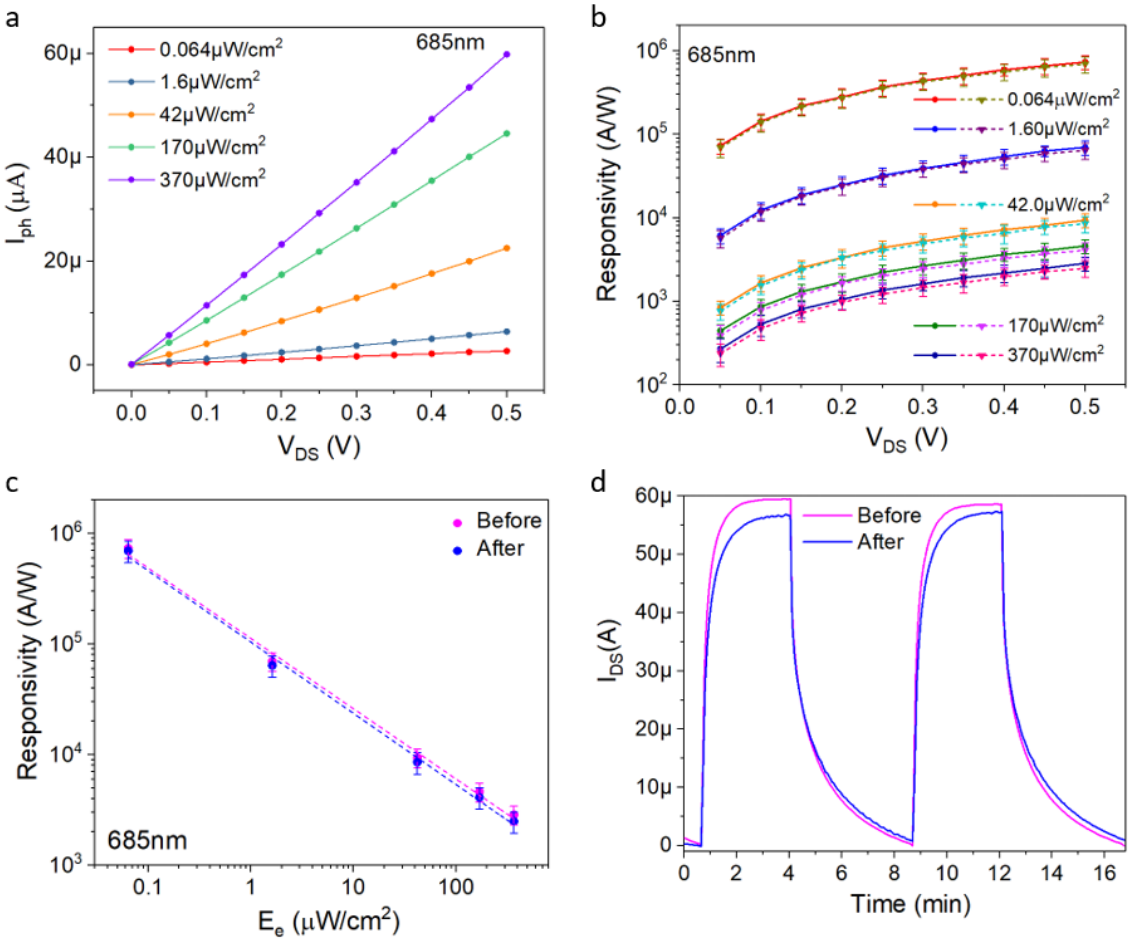

Figure 3.9. Device performance of the $FASnI_3$/PEDOT:PSS PD fabricated on flexible substrate. (a) photo-current vs. drain voltage of the as-fabricated device. (b) Average responsivity as a function of applied voltage for the PD before and after bending test. Circle dots and solid lines are for device before bending, while triangular dots and dash lines are for device after bending test. (c) Average responsivity vs. light intensity for the flexible device before and after bending test. The dashed lines are fitting curves using equation (3). Error bar indicates the standard deviation. (d) Temporal response of the PD before and after the bending test for two illumination on-off cycles.

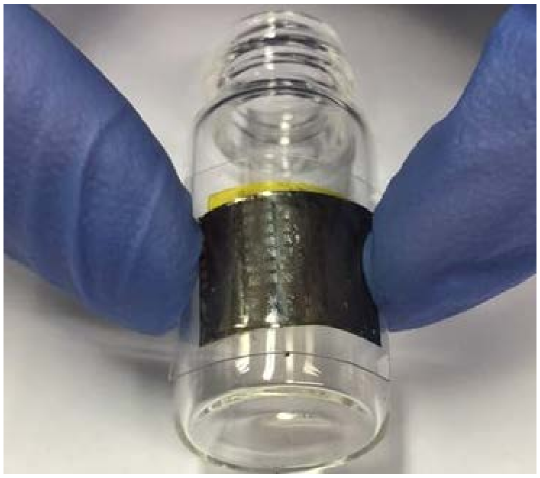

Figure 3.10. Illustration of the bending test for the flexible PD.

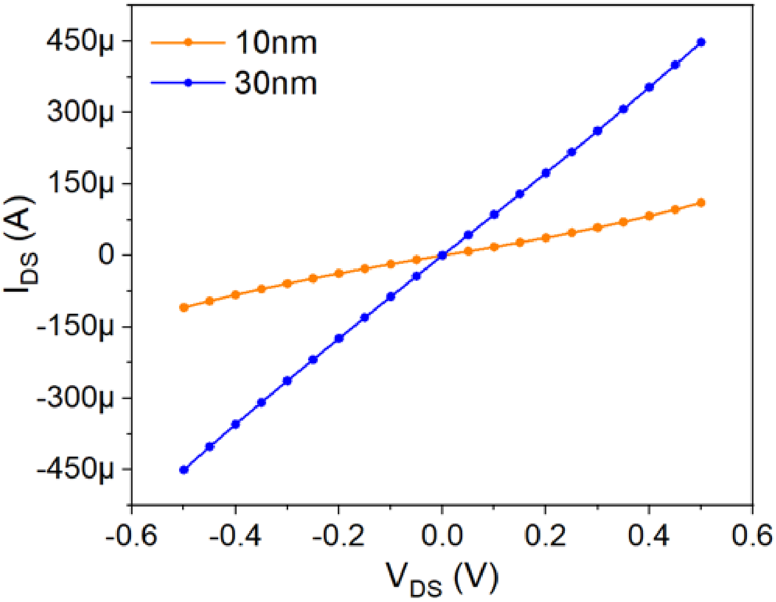

Figure 3.11. Dark current for perovskite/PEDOT:PSS PDs with different PEDOT:PSS thicknesses.

The bending test is done by curving the flexible device to the surface of a bottle with 8-mm radius (which corresponds to a bending degree of 8.6° for an individual device) for 300 times, as illustrated in **Figure 3.10**. Notably, responsivity at low intensity remains almost unchanged. **Figure 3.9d** displays the temporal response of the device before and after bending, respectively. The shape of the response curve and magnitude of photo-current also keep unchanged. Therefore, the bilayer PD fabricated on flexible substrate can maintain the high photo-response as well as excellent bending stability, which can be promising for future applications.

3.3 Conclusion

In summary, a high-performance lead-free perovskite PD has been realized based on a vertical heterojunction of $FASnI_3$ and PEDOT:PSS. Owing to the photo-gating effect, the device exhibits a high responsivity up to 2.6×10^6 A/W, gain of 4.7×10^6, specific detectivity of 3.2×10^{12} Jones. The PD also exhibits a broadband photo-response from UV to NIR. Notably, it maintains reasonable responsivity even at NIR light illumination (980nm and 1050nm) where the photon energy is lower than band gap of perovskite, which could be attributed to the traps in the bandgap of perovskite films. Additionally, higher detectivity and faster response speed can be achieved by simply reducing the PEDOT:PSS thickness in the device. Moreover, this PD can be fabricated on flexible plastic substrates and shows robust stability upon bending tests and high responsivity. This work demonstrates the feasibility of utilizing lead-free perovskites in environmentally friendly, low-cost, sensitive and flexible PDs in various applications.

3.4 Experimental Section

3.4.1 Materials Characterization

The thickness of PEDOT:PSS films were measured using Dektak XTL Stylus Profiler System. X-Ray diffraction (XRD) patterns of the perovskite films were measured using Rigaku SmartLab X-Ray diffractometer. JEOL JSM 6335F SEM (SEM) was employed to capture the SEM images. The absorbance of the $FASnI_3$ film was recorded with Hitachi UH5300 spectrophotometer. PL spectra was recorded using Edinburgh FLSP920 fluorescence spectrophotometer with an excitation wavelength of 635 nm.

3.4.2 Device Fabrication

Deposition of electrodes: First, 10-minute Ultrasonication baths of deionized water, acetone and IPA were applied to 300nm-SiO_2/Si or 50 μm-PI substrates. Then, nitrogen gas was used to dry those substrates. After that, the electrode area was defined by photolithography. Finally, Cr/Au (10nm/100nm) electrodes were deposited by thermal evaporation followed by an acetone lift-off process. The channel width (W) and length (L) were 6 and 800 μm, respectively.

Formation of PEDOT:PSS films on SiO_2/Si or PI: A PEDOT:PSS aqueous solution (Clevios PH 500, Heraeus Precious Metals GmbH & Co. KG, Leverkusen, Germany) was used as PEDOT:PSS source for this work. To enhance the wettability for PEDOT:PSS solution, the patterned substrates were first subjected to an oxygen plasma treatment for 10 minutes. Then, The PEDOT:PSS films were formed by spin coating the solution onto the substrates in ambient environment. The thicknesses of the PEDOT:PSS films can be controlled by changing the spinning speed and concentration of the PEDOT:PSS aqueous solution. After that, the substrate was taken into glovebox which filled with high purity nitrogen gas and annealed at 120°C for 30 minutes.

Formation of $FASnI_3$ film: To obtain the precursor solution, 1M Tin(II) Iodide (SnI_2) (Youxuan tech., 99,99%), 1 M Formamidinium iodide (FAI), 0.1 M Tin(II) Chloride ($SnCl_2$) (Aladdin, 99%), 0.1 M Dimethyl sulfoxide (DMSO) and 0.015M hydroquinone sulfonic acid (KHQSA) was mixed in a suitable amount of N,N-dimethylformamide (DMF). The two additives, namely KHQSA and excess $SnCl_2$, are used to improve the air stability of perovskite film. The detailed mechanism has been studied by our group before.[16] Briefly, the Sn^{2+} ion can interact with sulfonate group in KHQSA, inducing a $SnCl_2$-additive complex layer. The layer can encapsulate the perovskite grains and dramatically enhance the antioxidant ability for the perovskite film. Then, the solution was magnetically stirred for several hours to produce the perovskite precursor solution. After that, spin-coating for 30 seconds at 5000rpm was used to form a uniform film. 10s after the spin-coating started, 100μL of Chlorobenzene was dropped onto the substrate. Finally, the sample was annealed at 70 °C for 5 minutes.

3.4.3 Device Measurements

A semiconductor characterization system (Keithley 4200) was used to measure the electrical and opto-electrical performance of the devices. The light sources used to measure the photo-response of the devices are LEDs with wavelengths of 370, 420, 530, 685, 760, 850, 980 and 1050 nm. The measurement was conducted in a Nitrogen-filled glovebox. The light intensity used for the spectral responsivity, gain and detectivity measurement was ~500μW/cm^2.

The device performance of the flexible device was first measured using the above-mentioned equipment. After that, the devices were subjected to a bending test. They were curved against a glass bottle with 8-mm radius for 300 times. The corresponding bending degree for one individual device is 8.6 °. After that, the same measurement was conducted again. Notably, all the measurements for the flexible PD were performed in glove box to make sure the degradation of the device was solely caused by the bending test.

Chapter 4: High-Performance Quasi-2D Perovskite/Single-Walled Carbon Nanotube Phototransistors for Low-Cost and Sensitive Broadband Photodetection

quasi-2D Ruddlesden–Popper perovskites (RPPs) have emerged as promising functional materials for optoelectronics due to the highly tunable optoelectronic properties and have been considered as alternative candidates for semiconductors in PDs. However, RPPs normally show low carrier mobilities, which is unfavorable for the performance of PDs. Here, a solution-processed hybrid phototransistor based on RPP/SWCNT heterostructure is reported. A vertical composition gradient is formed upon RPP film preparation, which leads to a gradient type-II heterojunction in the film. More importantly, the high carrier mobility of SWCNTs can result in ultrahigh responsivity and detectivity of 2 x 10^6 A W^{-1} and 7 x 10^{14} Jones, respectively. In addition, high on/off ratio of ~10^3 can be achieved in the phototransistors. This work demonstrates the high potential of RPP/SWCNT hybrid phototransistors as next-generation PDs with superior sensitivity.

4.1 Introduction

PDs play a crucial role in many modern systems, such as optical communication, wearable electronics, healthcare and environmental monitoring.[1, 72] Due to expensive fabrication and material cost, high fragility and rigorous operating condition, the traditional PDs based on III-V semiconductors and Silicon fail to meet the ever increasing requirement of those applications.[9, 73] In recent years, OIHPs have emerged as promising candidate materials for next-generation PDs because of their unique properties, such as high optical absorption coefficient, easily tunable band gap, high carrier diffusion length and excellent defect tolerance.[1, 9, 74] However, the simple photoconductors based on typical OIHPs are relatively limited due to the absence of external gain mechanism and the abundant grain boundaries in perovskite thin films, despite the fact that they can be fabricated very conveniently.[9, 35, 75] For instance, Hu and his co-workers developed a photoconductor based on $MAPbI_3$ with a responsivity of 3.49 A W^{-1}.[35] Besides, the low formation energy of typical perovskites lead to highly unstable devices in ambient condition.[76]

A feasible way to introduce the external gain mechanism to the perovskite PDs is to construct a hybrid phototransistor by inserting an additional transporting layer with higher carrier mobility.[31, 70b, 77] The photo-gating effect induced by suitable band alignment between the functional materials can effectively prolong the carrier lifetime. Such hybrid phototransistors thus generally exhibit much higher photo-response than simple photoconductors, with certain sacrifice on response speed. Actually, many 2D materials have been adopted as transporting layers, such as graphene, 2D Transition Metal Dichalcogenides (TMDs) and black phosphorus.[31-32, 41, 67b, 78] Impressive responsivity of 10^9 A W^{-1} and detectivity of 10^{16} Jones can be achieved in some devices.[32, 79] Although excellent results were obtained, lack of low cost and large area fabrication techniques of 2D materials in those devices limits their potentiality towards practical applications.[49c] On the other hand, a great deal of research effort has been put on improving the stability of perovskite, such as compositional engineering and the development of all-inorganic perovskites.[18, 80] Recently, a new type of perovskites has been developed, namely quasi-2D quasi-2D RPPs, which share a common chemical formula of $(RNH_3)_2A_{n-1}M_nX_{3n+1}$, where RNH_3 represents an organic long-chain spacer cation, A is a regular monovalent organic cation, M is a divalent metal cation and X is a halide anion.[36, 81] The number of *n* indicates how many $[MX_6]^{4-}$ octahedral layers are inserted between the two large spacer cations. The quantum well structure due to the encapsulation of $[MX_6]^{4-}$ layers by the spacers not only leads to a series of unique optoelectronic properties, but also ensures the excellent photo- and chemical stability.[41] More importantly, the RPP thin films tend to consist of phases with gradient n values throughout the whole film,[41, 82] which can significantly enhance the optoelectronic properties of the resultant PDs. Since the large insulating spacer groups can hinder the carrier transport, organic intercalation engineering has been performed to shorten the interlayer distance between the inorganic layers and thereby improving the mobility.[37] However, the RPPs in those cases are still polycrystalline, which limits the carrier lifetime. A more serious gate-field screening effect may also exist due to the lighter spacer cations, which hampers the observation of field-effect transistor (FET) behaviors in those RPPs.[83] Therefore, the incorporation of high mobility transporting layer is still necessary to obtain excellent device performance.

In this work, a solution-processed high performance hybrid phototransistor based on RPP/SWCNT heterostructure has been developed. It is found that the occurrence of vertically conpositional gradient heterojunction nature in RPP thin film effectively enhances the carrier separation. Together with the high quality RPP film on SWCNTs and the excellent transport properties of SWCNT thin film, excellent device performance is achieved. The resultant phototransistors have decent responsivity and detectivity of up to 2×10^6 A W^{-1} and 7×10^{14} Jones, which are one order of magnitude higher than those of a hybrid phototransistor based on a typical 3-dimensional (3D) provksite $MAPbI_3$ and SWCNT. Furthermore, the maximum transistor and PD on/off ratio are measured to be as high as $\sim 10^3$. This work sheds light on the development of high-performance and low-cost PDs for practical applications based on RPPs and SWCNT thin films.

4.2. Results and discussion

4.2.1 Working Mechanisms

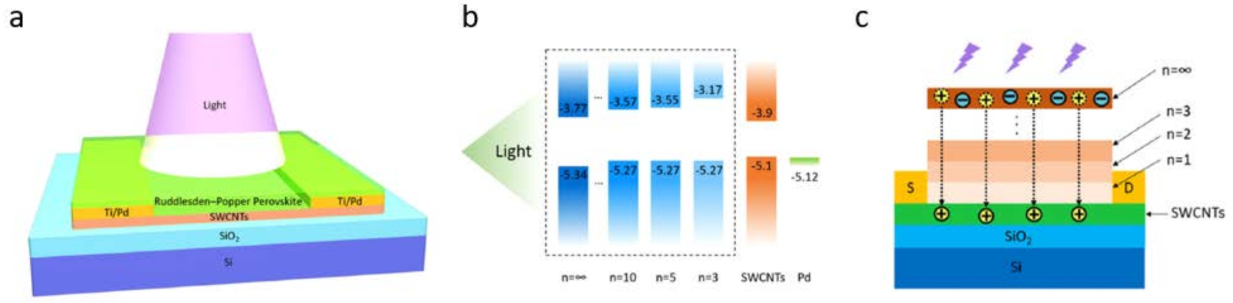

Figure 4.1. Illustration of device mechanism for RPP/SWCNT hybrid phototransistor and SEM images for RPP films. (a) Device design of the RPP/SWCNT hybrid phototransistor. (b) Band alignment of SWCNTs and the RPP with different layer numbers. (c) Schematic diagram for explaining photo-carrier transport mechanism in the device.

As illustrated in **Figure 4.1a**, the device channel consists of a layer of SWCNT at the bottom as a charge transport layer and a RPP layer at the top as photosensitive layer. The RPP used here is $(PEA)_2(MA)_{n-1}Pb_nI_{3n-1}$ (PEA = Phenethylamine) with a stoichiometric n value of 3, which has been optimized for efficient charge separation and film quality in our recent work.[82] During film formation, the inorganic $[MX_6]^{4-}$ octahedral network tends to spread parallel to the substrate, while the large heavy spacer cations tend to diffuse from top to bottom. The resultant RPP film consists of RPP layers with decreasing n values towards the film rear. **Figure 4.1b** displays the schematic band alignment between RPPs and SWCNTs. The band energy levels of different RPPs and SWCNTs are referenced from previous studies.[84] The RPPs in the film tend to form a gradient type-II heterojunction with n value decreases from top to bottom. Such effect significantly enhances the photo-carrier separation and hence the carrier recombination lifetime. The schematic diagram in **Figure 4.1c** illustrates the charge transport in such hybrid phototransistor. Upon light illumination, most of the incident photons absorbed within tens of nanometres beneath the perovskite film surface owing to the high optical absorption coefficient of the perovskites. Afterwards, excessive electron-hole pairs near the film surface are rapidly generated owing to low exciton binding energy and efficient photoelectric conversion.[36] According to the relative band alignment, the photo-generated electrons will be trapped near the perovskite surface while holes can be effectively transferred into SWCNT layer due to strong built-in electric field provided by the band alignment. The carrier lifetime is therefore prolonged significantly. Since the vertical travelling distance for the photo-carriers are relatively short, most of the photo-generated holes are transferred to SWCNTs before recombining at the grain boundaries of perovskite layer. On the other hand, the carriers in SWCNT layer can have a short transit time owing to its high mobility. The gain (G) of a PD can be represented by: $G = \tau/t_{tran}$, where τ and t_{tran} are carrier lifetime and carrier transit time in the channel.[85] Therefore, increasing τ and reducing t_{tran} can effectively improve the gain in the devices.

4.2.2 Materials Characterization

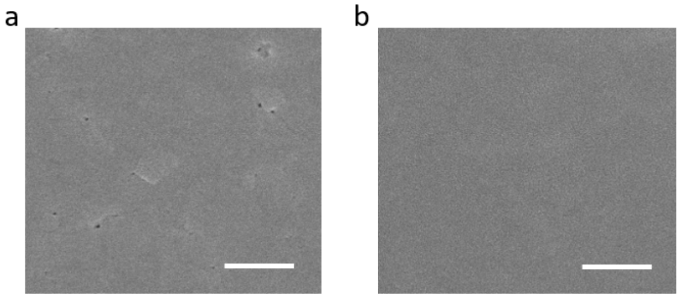

Figure 4.2. SEM images of RPP films spin-coated on (a) SiO_2/Si and (b) SWCNTs. Scale bars are 500nm.

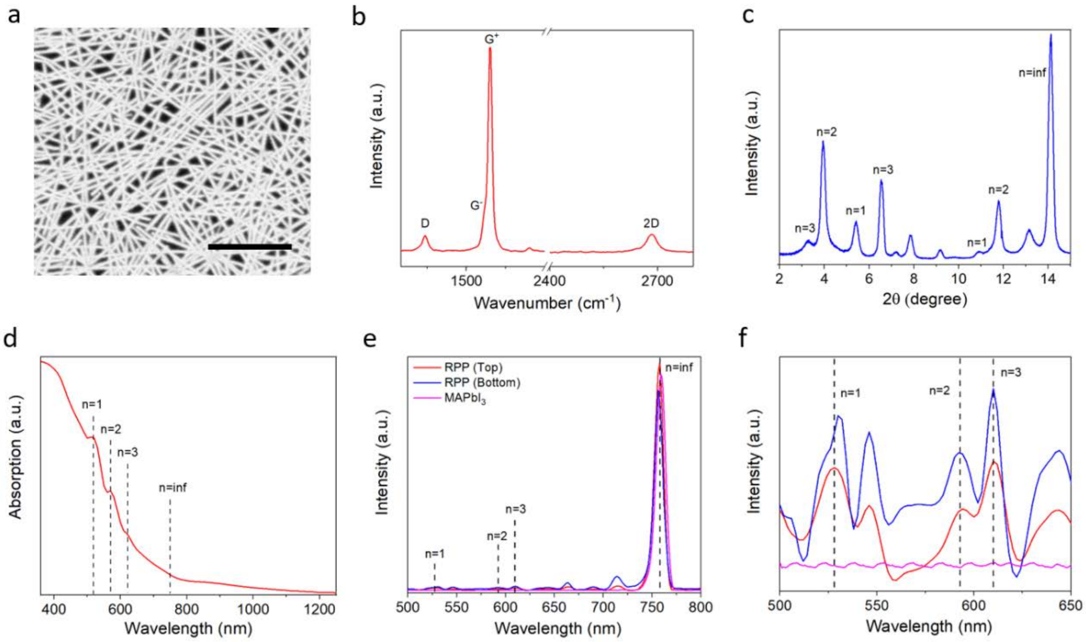

Figure 4.3. Materials characterization. (a) SEM image and (b) Raman spectra of SWCNT thin film on SiO_2/Si. Scale bar is 500 nm. (c) XRD spectra and (d) absorption spectra of RPP films. (e) PL spectra of a RRP film excited from top or bottom as well as that of a typical 3D perovskite $MAPbI_3$ film. (f) The zoomed view of the same PL spectrums for wavelengths below 650nm. The excitation source is a 488 nm laser.

The SEM images (**Figure 4.1d**) for a RPP film spin-coated on SiO_2/Si directly reveals that such film contains some pin holes and large grains. These makes the film relatively rough. On the other hand, the film spin-coated on SWCNTs are much smoother and without any pinhole (**Figure 4.1e**), which is highly desirable for photo-electric conversion and carrier transport.[41,42] The smoother RPP film on SWCNTs than on SiO_2/Si surface may be due to the more uniform nucleation. The SWCNTs are uniformly distributed on SiO_2/Si surface and tend to attract MA^+ and PEA^+ ions when precursor solution is spin-coated on it.[86] Those evenly and densely attached ions then act as nucleation seeds so that the grown RPP crystals can have uniform grain size and specific phase distribution after annealing. Finally, a dense RPP film can be formed. On the other hand, the RPP crystals nonuniformly grow without uniform nucleation seeds on SiO_2/Si, resulting in a rougher surface with many pinholes and relatively random distribution of RPP phases. To ensure the excellent FET performance, SWCNTs with >99.9% semiconducting purity is used.[87] Moreover, the SEM image of a SWCNT layer (**Figure 4.2a**) reveals that the SWCNTs are densely connected to form a conductive network, which is necessary for high performance FETs.[87b, 88] The length and diameter of a single nanotube are about 1-2 μm and 1.2-1.7 nm, respectively. Raman spectra of the SWCNT thin film is displayed in **Figure 4.2b**. The characteristic peaks are consistent with previous studies.[89] In the X-ray diffraction (XRD) spectra of RPP film (**Figure 4.2c**), diffraction peaks for RPP phases of different *n* values are measured in a single sample, indicating the multiphase characteristics of the perovskite film. Similar conclusion can be drawn from the absorption spectra (**Figure 4.2d**), where multiple absorption peaks for RPPs with different *n* numbers can be found. PL spectra were acquired from both top and bottom of a RPP film as well as a typical 3D perovskite $MAPbI_3$ film (**Figure 4.2e and 4.2f**). It can be noted that the PL response for RPP film is highly dependent on excitation direction, that is, the intensities of the important peaks are different when the film is excited from top or bottom.[82] Specifically, an intensive 3D peak and weak 2D peaks are acquired when the film is excited from the top, whereas a weaker 3D peak and stronger 2D peaks are acquired when it is excited from the bottom. Such observations are consistent with the gradient multiphase nature of the film. The thicknesses of RPP and $MAPbI_3$ on the SWCNTs was measured to be ~1 μm.

4.2.3 Phototransistor Performance

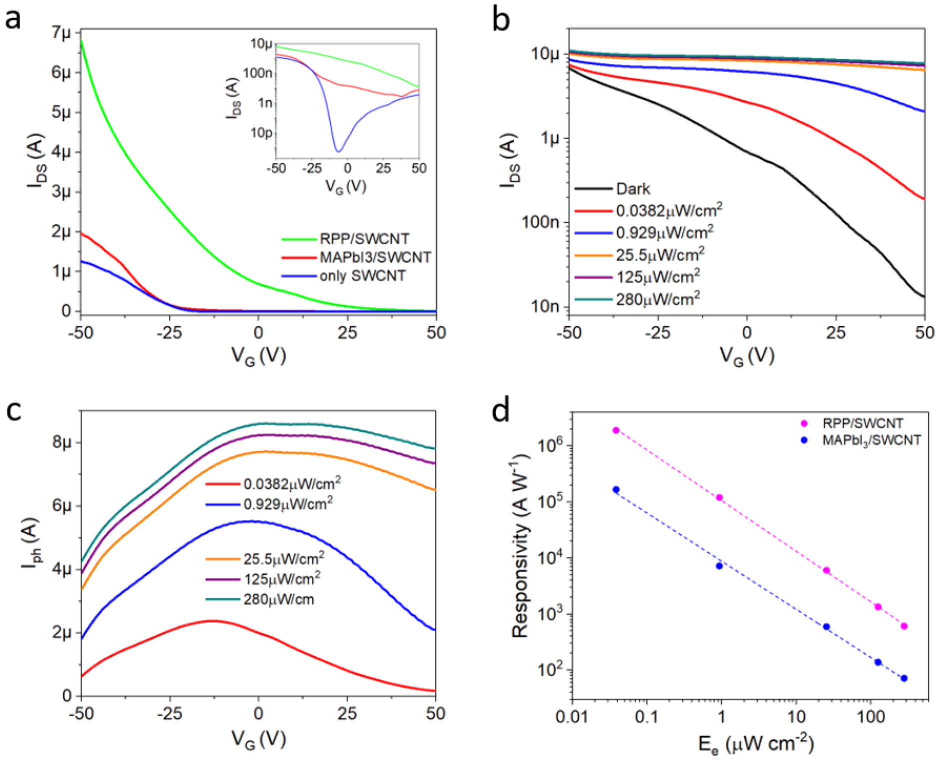

Figure 4.4. (a) linear plot of transfer curves in dark for different kinds of devices. Inset graph is the semi-log plot for the transfer curves. (b) Transfer curves and (c) Photocurrent vs. applied gate voltage for a RPP/SWCNT phototransistor under 598 nm light illumination of various intensities. (d) Responsivity as a function of light intensity for devices under 598 nm light illumination.

For all the device measurements, the drain voltage was fixed at 0.5V unless otherwise specified. As displayed in **Figure 4.3**a, the pristine SWCNT FET has a well-defined ambipolar transfer characteristics. The field-effect mobility can be calculated according to the equation:[6]

$$\mu = \frac{L}{W \times C_{OX} \times V_{DS}} \times \frac{dI_{DS}}{dV_G},$$

where L, W and C_{OX} are channel length, width and specific capacitance of SiO_2, respectively. The hole and electron mobility are calculated to be 17.5 and 1.2×10^{-2} $cm^2V^{-1}s^{-1}$, respectively. The high hole mobility is beneficial for photo-electron transport in the channel. After the incorporation of perovskites onto the SWCNTs, the charge neutrality point shifts from the negative to the positive side, indicating p-type doping in the SWCNT (**Figure 4.3a**). The obviously higher p-doping in RPP-based sample than that in $MAPbI_3$-based sample is due to the gradient heterojunction which favours the hole transporting to SWCNTs. The mobility values of RPP/SWCNT and $MAPbI_3$/SWCNT devices can be extracted from Figure 3a and calculated to be 9.7 and 7.4 $cm^2V^{-1}s^{-1}$, respectively. These values are much higher than those in previously reported FETs with perovskite-only channels.[51, 90] The slightly reduced mobility after perovskite coating may be due to partial gate-field screening in perovskite films. The higher mobility in RPP/SWCNT device than that in $MAPbI_3$/SWCNT could thus be attributed to the suppressed field-induced ion migration in RPP film by the large spacer cations. The additional SWCNT thin film underneath the perovskite films can enhance mobility of the system. Since the hole mobility of SWCNT is much higher than perovskites and the holes in perovskites spontaneously transfer to SWCNTs, the SWCNT film becomes the dominant channel to determine the mobility of the system and the carrier transport in perovskites is negligible.

The device performances for RPP/SWCNT and $MAPbI_3$/SWCNT were measured and compared carefully. It was found that RPP/SWCNT device exhibits the obviously better overall PD performance. **Figure 4.3b** shows the transfer curves for a representative RPP/SWCNT phototransistor in dark and under 598nm light illumination with different light intensity. The photocurrent increases monotonically with light intensity and the transistor on/off ratio gradually reduces from $\sim 10^3$ to ~2 as light intensity increases. This is due to the increased number of holes accumulated in the SWCNT channel, which leads to p-doping in the channel. Notably, under a gate voltage of 50V, the PD has an on/off ratio of $\sim 10^3$.

The relation between photocurrent (I_{ph}) and gate voltage can be extracted from **Figure 4.3b** and has been plotted in **Figure 4.3c**. The gate voltages for maximum photocurrent gradually shift to positive side as light intensity increases, which indicates the higher photo-doping in the SWCNT layer. Responsivity (R) is a direct parameter to quantitatively characterize the photo-response of a phototransistor. **Figure 4.3d** reveals the maximum responsivity as a function of light intensity for devices based on RPP and $MAPbI_3$. Notably, the responsivity of RPP/SWCNT device reaches its maximum value at 2×10^6 A W^{-1}. Such value is impressive even comparing to other reported perovskite-based hybrid devices.[41, 91] The gain represents how many effective photo-carriers can be generated upon absorbing one photon. The corresponding maximum gain for RPP/SWCNT device can be calculated to be 4.1×10^6. Notably, the responsivity and gain for the RPP/SWCNT device are one order of magnitude higher than that for the $MAPbI_3$/SWCNT device (1.6×10^5 A/W for responsivity and 3.6×10^5 for gain). The much higher performance for RPP/SWCNT phototransistor is due to the existence of multiple type-II heterojunction formed by vertical RPP composition gradient, which significantly enhances the photo-gating effect. Although typical 2D RPPs has larger exciton binding energy than $MAPbI_3$ and consist of insulating spacer cations, the surface of our RPP film is actually 3D perovskite. Since the photo-electric conversion happens near the film surface due to the high absorption coefficient and the photo-carriers are separated immediately by the vertical built-in electric field, the large exciton binding energy of 2D RPPs is actually irrelevant. On the other hand, although the density of spacer cation increases as the holes drift drift from film surface towards bottom, the band bending near RPP/SWCNT interface is strong enough to drive the holes to tunnel from RPP to SWCNTs. Therefore, the higher responsivity and gain in RPP/SWCNT device compared to $MAPbI_3$/SWCNT device is not surprising. It is also notable that the responsivity and hence the gain reduces with increasing light intensity. Such phenomenon can be attributed to the increased accumulated holes in SWCNT and electrons in perovskites. The greater number of carriers in respective layers, the higher the recombination rate, leading to the lower responsivity and gain.

Detectivity (D*) is a figure of merit to measure the sensitivity of a PD. The stable time-dependent dark current is plotted for V_G at -13V (**Figure 4.4a**) and 50V (**Figure 4.4b**), which are corresponding to the points where highest responsivity and lowest dark current, respectively. Noise level per unit bandwidth at 1Hz can be found by performing FFT to the dark current (**Figure 4.4c**). The resultant detectivity for V_G = -13V and 50V are calculated to be 1 x 10^{14} and 7 x 10^{14} Jones, respectively. Such detectivity values are also superior to many other reported perovskite-based hybrid devices.[24,53,54,56] The enhancement of detectivity at a more positive gate voltage is due to the lower dark current, which is originated from the less p-doping in the SWCNT transporting layer.

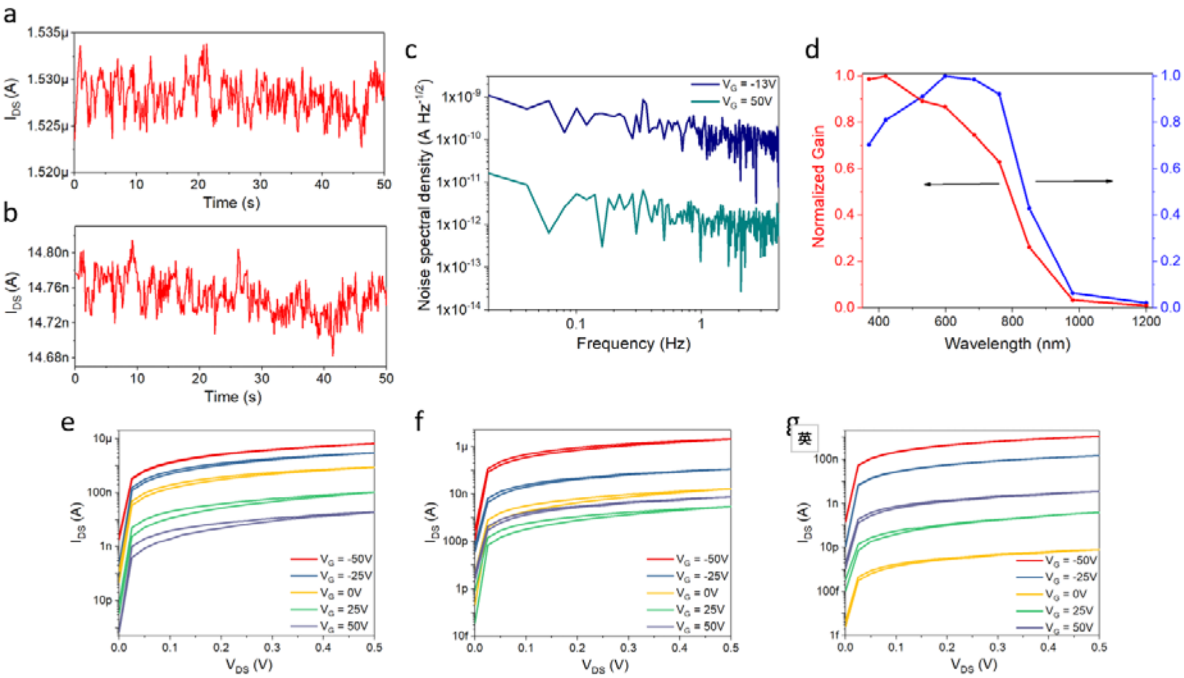

Figure 4.5. Dark current analysis for detectivity characterization, spectral response for RPP/SWCNT device and supplementary electrical characterization of the devices. Stable dark current vs. time for V_G = -13V (a) and V_G = 50V (b). (c) Noise spectral density as a function of frequency extracted from (a) and (b) by FFT. (d) Spectral gain and responsivity. I-V curves under various gate voltages for (e) RPP/SWCNT, (f)$MAPbI_3$/SWCNT and (g) SWCNT devices, respectively.

Spectral response is also an important characteristic for a phototransistor. **Figure 4.4d** reveals the normalized gain and responsivity as a function of wavelength. The phototransistor exhibits photo-response across UV to NIR (370 nm to 1200 nm). Notably, the gain rapidly increases from 980nm to 760nm, revealing the band edge of 3D perovskite. This is because the perovskite film surface consists of mainly 3D perovskite and most of the incident light is absorbed near it. After that, it keeps increasing up to 420 nm. On the other hand, the responsivity reaches its maximum at 598 nm and then gradually reduces for shorter wavelengths. This is because the number of higher energy photon is less than that of lower energy ones in a given optical power. Therefore, even though the gain near UV region is higher, the number of absorbed photons is actually lower, leading to a lower responsivity in higher energy region. Additionally, it can be noted that there is an obvious extension of photo-electric conversion even beyond the band gap of 3D perovskite. This can be attributed to the excitation of electrons from the traps close to the valence band to the conduction band or from the valence band to the traps near the conduction band.[92] Since shallow traps typically have high capture cross-section, the response is stronger near the band edges and rapidly decays for longer wavelengths.[6]

Figure 4.5a shows the time-dependent photo-response of the RPP/SWCNT and $MAPbI_3$/SWCNT phototransistors, respectively. The devices exhibit stable and repeatable photo-response under periodic light on/off cycles. Response time is the standardized parameter to characterize the dynamic response of a phototransistor. The rise (decay) time can be defined as the time width between 10% and 90% of the rising (decaying) edge of the dynamic response (Figure 5b). The response times of the devices are listed in **Table 4.1** together with other performance parameters. It can be noted that the RPP/SWCNT phototransistor has longer rising and decay time. This is due to the much longer carrier lifetime in the devices caused by the gradient heterostructure in RPP film.[32, 49c, 91b] High gain PDs typically exhibit relatively slow response.[20, 49c] Incidentally, although the gain in MAPbI3/SWCNT device is much lower than that in RPP/SWCNT device, it is still higher or comparable to other $MAPbI_3$-based hybrid phototransistors.[65a, 93] To have a deeper understanding on this phenomenon, the decaying edge of the dynamic response for the three devices are fitted with a double exponential function with two relaxation times:

$$I_{ph} = A_f \exp\left(-\frac{t}{\tau_f}\right) + A_s \exp\left(-\frac{t}{\tau_s}\right),$$

where A_f and τ_f are magnitude and time constant for the fast component of the decay process, while A_s are τ_s are magnitude and time constant for the slow component of the decay process. As revealed in **Figure 4.5c and d**, the curves are fitted very well by this exponential function. In the first stage of the decaying process, a large number of excessive photo-carriers accumulated in respective layers can screen the internal electric of the vertical heterojunctions. The carriers thus undergo rapid recombination, which is represented by the first component of the fitting function. After that, the screening effect is gradually weakened due to reduced excessive photo-carriers. Hence, the electric field builds up again and reduces the recombination rate. This is represented by the second component of the function. The time constants for different devices are summarized in **Table 4.1**. The two time constants of 3D perovskite-based device are smaller than that of the RPP-based one, which is due to the different characteristics of the two films. The gradient heterojunction in RPP-based sample results in a stronger vertical internal electric field. Thus, the internal electric field in such sample builds up immediately after the first decaying stage. The remaining trapped carriers are strongly prohibited for recombination at perovskite/SWCNT interface. By contrast, there is only a single $MAPbI_3$/SWCNT heterojunction in $MAPbI_3$-based sample. The internal electric field is thus weaker, and the carriers are less prohibited from recombination.

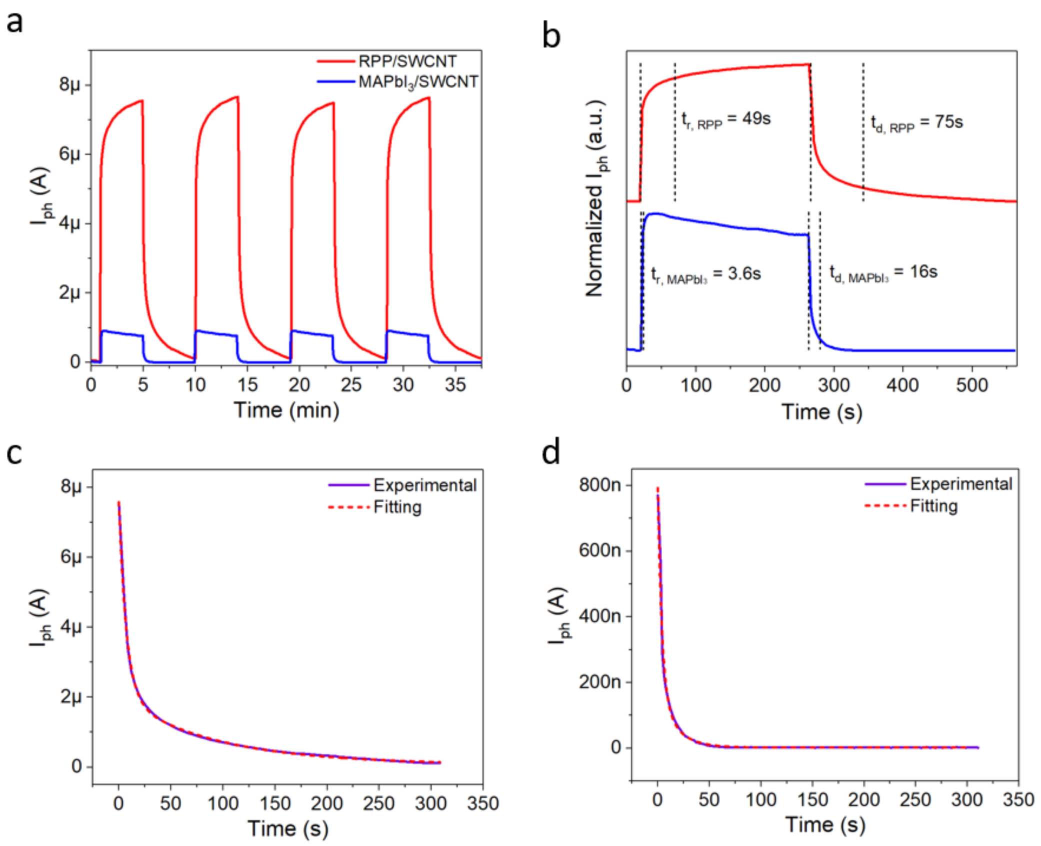

Figure 4.6. Transient response of the phototransistors. (a) Photocurrent vs. time under four on-off cycles of 598 nm light illumination. (b) Normalized photocurrent vs. time under one on-off illumination cycle. Experimental and fitting curves for the time-dependent photo-response decaying edge of (c) RRP/SWCNT and (d) MAPbI$_3$/SWCNT phototransistors.

Table 4.1. Performance parameters of the devices.

Device Architecture	Responsivity (A/W)	Detectivity at depletion (Jones)	Rise/Decay time (s)	τ_f (s)	τ_s (s)
RPP/SWCNT	2.0×10^6	7.1×10^{14}	49/75	7.2	91
MAPbI$_3$/SWCNT	1.6×10^5	1.9×10^{13}	3.6/16	3.9	17

4.3. Conclusion

To conclude, a solution-processed high performance RRP/SWCNT broadband phototransistor has been developed. Owing to the spontaneously formed vertical composition gradient in the RPP film, a gradient type-II heterojunction can be obtained. The resultant device exhibits responsivity and detectivity of up to 2 x 10^6 A W^{-1} and 7 x 10^{14} Jones, which are one order of magnitude higher than those of 3D perovskite/SWCNT device. Moreover, transistor and photo-response on/off ratio of ~10^3 can be achieved. The outstanding performance is primarily due to the vertically gradient heterojunction in RRP film and the high carrier mobility of SWCNT thin film. This work paves the way towards solution-processed high-performance PDs based on RRPs and semiconducting CNTs for next-generation PDs.

4.4 Experimental Section

4.4.1 Materials Characterization

The crystal structure information was acquired by an X-Ray diffractometer (Rigaku SmartLab). The surface morphology of RPP and SWCNT films on SiO_2/Si were obtained using a field-emission SEM (Hitachi S-4300) and a SEM (Zeiss Supra 55), respectively. The Photoluminescence measurements were performed fluorescence Spectrometer (Edinburgh FLSP920) with a 485 nm laser as excitation light source. The absorption spectra were collected with a UV–vis–NIR spectrometer (Perkin elmer). The thicknesses of RPP and $MAPbI_3$ films on SWCNTs was measured using a Bruker DektakXT Surface Profiler.

4.4.2 Phototransistor Fabrication

SWCNT FET fabrication: SWCNT FETs were fabricated with a method described in previous studies.[87b] Briefly, high quality semiconducting SWCNT solution (Beijing Huatan Technology Co., Ltd., China) was first dispersed in chloroform. After that, CNTs were dip-coated on SiO_2 (300 nm)/Si substrates cleaned by standard procedure. Next, FETs were fabricated by typical photolithography process. SiO_2 and Si is used as gate dielectric and electrode, respectively. The channel area was patterned using oxygen plasma etching. Ti/Pd (0.3 nm/40 nm) electrodes were deposited onto the CNT film by electron beam evaporation. Finally, a conventional lift-off process was performed.

Perovskite precusor solution preparation: 1.5M $(PEA)_2(MA)_2Pb_2I_{10}$ precursor solution was prepared by dissolving stochiometric amount of PEAI (Greatcell Solar Ltd), MAI (Greatcell Solar Ltd), and PbI_2 (Sigma-Aldrich) in a mixed solvent of DMSO (Sigma-Aldrich)/DMF (Alfa Aesar) (1:14 volume ratio). The obtained precursor solution was subsequently magnetically stirred at 70 ^{o}C overnight. On the other hand, 1.5M $MAPbI_3$ precursor solution was prepared by dissolving stochiometric amount of MAI (Greatcell Solar Ltd), and PbI_2 (Sigma-Aldrich) in a mixed solvent of DMSO (Sigma-Aldrich)/DMF (Alfa Aesar) (1:8 volume ratio). The obtained precursor solution was subsequently magnetically stirred at room temperature overnight. The processes mentioned above were all performed in a glove box filled with N_2 gas.

Hybrid phototransistor fabrication: For devices consist of RPP film, the precursor solution was preheated at 70 ^{o}C for 30 minutes prior to spin-coating. In the spin-coating process, about 60 μL of precursor solution was dropped onto a SWCNT film followed by spin-coating at 4000 rpm for 30s. After spin-coating, the samples with RPP and $MAPbI_3$ were annealed at 70 ^oC for 30 minutes and 100 ^oC for 20 minutes, respectively. Again, the processes were all conducted in a nitrogen-filled glove box.

4.4.3 Device Measurements

The device performance was recorded with a semiconductor parameter analyser (Keithley 4200) and a probe station equipped with LEDs of various wavelengths. All the devices are measured in a glovebox filled with nitrogen gas. When acquiring spectral gain and responsivity, the intensity for all measured wavelengths was fixed at about 500 µW cm^{-2}.

Chapter 5: 2D Metal–Organic Framework $Cu_3(HHTT)_2$ Films for Broadband PDs from Ultraviolet to Mid-Infrared

$Cu_3(HHTT)_2$ is a novel two-dimensional conjugated metal-organic framework (2D c-MOF) with efficient in-plane d-π conjugations and strong interlayer π-π interactions while the growth of $Cu_3(HHTT)_2$ thin films has never been reported until now. Here, we present the successful fabrication of highly oriented wafer-scale $Cu_3(HHTT)_2$ thin films with a layer-by-layer growth method on various substrates. Its semiconducting behavior and carrier transport mechanisms are clarified through temperature and frequency dependent conductivity measurements. Flexible PDs based on $Cu_3(HHTT)_2$ thin films exhibit reliable photo-response at room temperature in a wavelength region from ultraviolet (UV) to mid-infrared (MIR), which is much broader than those of solution-processed broadband PDs previously reported. Moreover, the PDs can show a typical synaptic behavior and excellent data recognition accuracy in artificial neural networks. This work opens a window for the exploration of high-performance and multi-functional optoelectronic devices based on 2D c-MOFs.

5.1. Introduction

MOFs represent an important class of porous crystalline materials, in which organic ligands are interconnected by metal nodes.[27, 43, 94] They have long been considered as promising candidates for a wide range of applications, such as catalysis[23, 44, 95], gas sensor[24, 95b, 96] and storage[23, 25, 97], mainly due to their high porosity, excellent specific surface area, and highly tailorable chemistry.[98] However, the low conductivity of conventional MOFs precludes them from optoelectronic applications.[94, 99] Recently, a new type of MOFs, namely two-dimensional conjugated MOFs (2D c-MOFs), was discovered. They have not only the unique properties of conventional MOFs like high porosity and tailorability of crystal structure but also outstanding electrical transport properties due to high in-plane-π-conjugation and compact interlayer π- π stacking in their crystals.[2, 13 them.[94, 100] Recently, various electronic devices based on 2D c-MOF thin films have been developed, such as field-effect transistors[42, 101], supercapacitors[102], chemiresistors[96, 103] and batteries[97d, 104]. Different bottom-up schemes have been adopted to grow 2D c-MOFs thin films, such as layer-by-layer assembly, liquid-air interface, liquid-liquid interface and face-to-face confined growth methods.[46, 96b, 101a, 105] 2D c-MOF $Cu_3(HHTT)_2$ (HHTT: 2,3,7,8,12,13-hexahydroxy tetraazanaphthotetraphene) has been reported to be an efficient electrocatalyst for CO_2 reduction and electrode materials for Li storage, [21, 44, 94] which features excellent in-plane and out-of-plane crystallinity due to the large ligand core with heteroatoms. The 2D c-MOF is expected to have high conductivity because of the efficient in-plane d-π conjugations and strong interlayer π-π interactions.[94] However, the preparation of $Cu_3(HHTT)_2$ thin films has never been reported until now, which prohibits the study of its transport mechanisms and applications in thin-film electronic devices.

Traditional PDs based on Si and typical III-V semiconductors suffer from high fabrication cost, narrow detection range and fragility. [9] Therefore, PDs with broadband detectable range, mechanical flexibility and convenient fabrication are highly desirable for many emerging applications like wearable electronics and medical imaging. On the other hand, optical synapse, which can receive external optical stimuli and transform the signal to postsynaptic current, is an essential building block of highly efficient neuromorphic computing, which cannot be realized based on conventional semiconductor PDs.[106] Considering the high tunability of their optoelectronic properties, 2D c-MOFs may have tremendous potential for these applications, which have been rarely reported until now. [46, 107]

Chapter 5

In this work, wafer-scale $Cu_3(HHTT)_2$ thin films are prepared by a convenient layer-by-layer solution growth technique for the first time. By optimizing the growth conditions such as precursor concentrations and solvents, highly oriented, smooth, and uniform $Cu_3(HHTT)_2$ thin films are obtained. A small band gap of 0.55 eV is acquired from light absorption spectrum. Based on temperature dependent conductivity measurements, the carrier transport mechanism in the films can be attributed to phonon-assisted hopping process. PDs based on $Cu_3(HHTT)_2$ thin films are fabricated, which exhibit reliable broadband photo-response from UV to mid-infrared (MIR) (370 nm to 3400 nm) at room temperature due to the small bandgap and broadband light absorption of the 2D c-MOF. The extended response to MIR light with a photon energy less than the bandgap is due to the activation of carriers from the mid-gap states, which may find applications in medical imaging and chemical monitoring. Moreover, $Cu_3(HHTT)_2$ thin films can be conveniently prepared on plastic substrates, leading to flexible PDs with excellent mechanical stability. Notably, an optical synapse based on a $Cu_3(HHTT)_2$ thin film is also demonstrated, which shows excellent synaptic responses and outstanding data recognition accuracy in an artificial neural network (ANN) simulation. This work paves a way for the applications of 2D c-MOF thin films in high-performance and multi-functional optoelectronics.

5.2 Results and Discussion

5.2.1 Thin Film Growth Mechanisms and Material Characterization

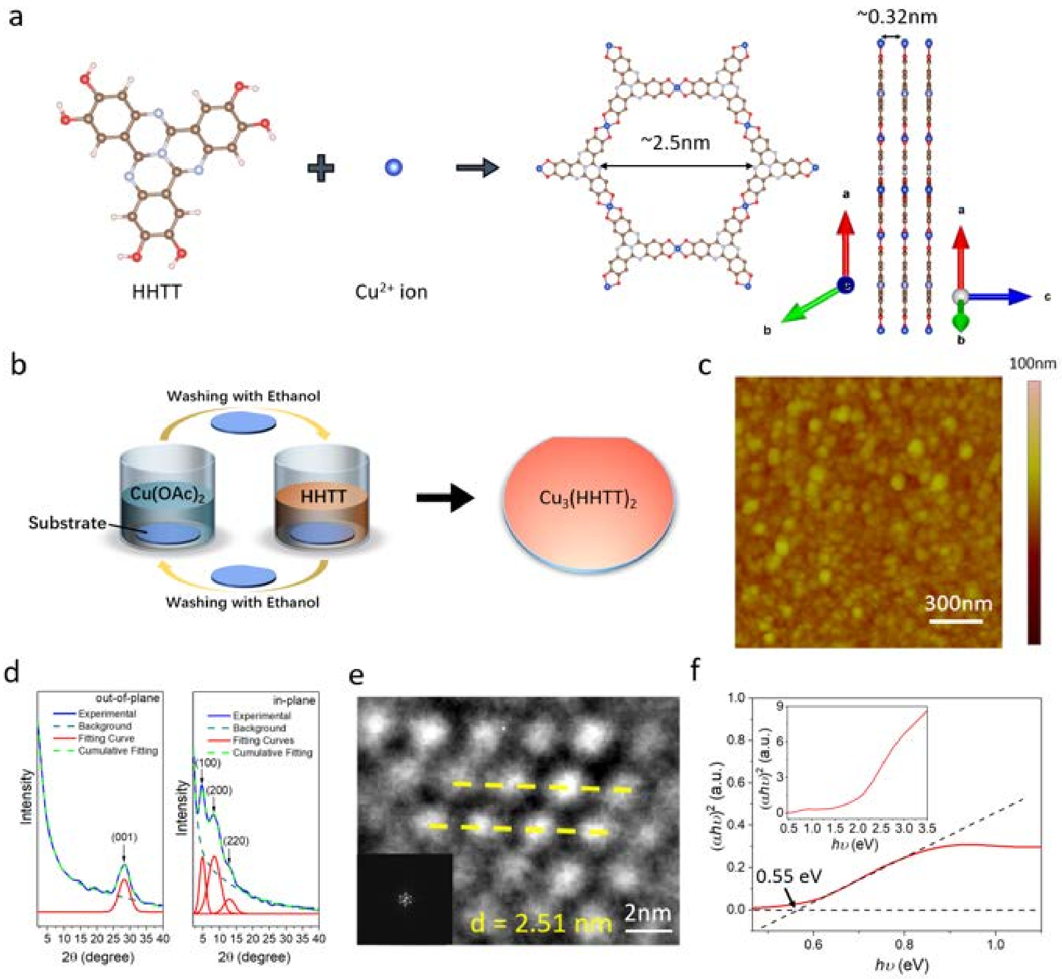

Figure 5.1. Fabrication and properties of $Cu_3(HHTT)_2$ thin films. (a) Synthetic route and crystal structure of $Cu_3(HHTT)_2$. (b) Fabrication procedure of $Cu_3(HHTT)_2$ thin films. (c) AFM image of a $Cu_3(HHTT)_2$ thin film with a thickness of 132 nm. (d) Out-of-plane (left) and in-plane (right) GIXRD patterns of a 132-nm thick $Cu_3(HHTT)_2$ thin film. (e) HRTEM image of a $Cu_3(HHTT)_2$ film and the corresponding FFT image (inset). (f) Tauc plot of the absorption spectrum of a 132-nm thick $Cu_3(HHTT)_2$ thin film.

Figure 5.1a shows the formation of $Cu_3(HHTT)_2$ through the reaction between HHTT ligands and Cu^{2+} ions by a layer-by-layer growth method.[42] The processing details are presented in Experimental Section and graphically illustrated in **Figure 5.1b**. Briefly, an -OH functionalized pre-patterned substrate is firstly immersed into a solution of $Cu(OAc)_2$, where the Cu ions are anchored by -OH groups. Next, the substrate is transferred to a HHTT solution to complete the formation of a $Cu_3(HHTT)_2$ film. Such processes are then repeated for many times until a desired film thickness is obtained. The resultant 2D c-MOF shows a planar honeycomb structure with a pore size of about 2.5 nm and an interlayer distance of about 0.32 nm according to the literature (**Figure 5.1a**).[44, 94] In comparison with the strong in-plane covalent bonds, the inter-planar interactions are dominated by π-stacking interactions,[94] which can enable well-oriented thin film growth from the substrate.

Table 5.1: Thickness, root mean square (RMS) surface roughness and roughness-to-thickness ratio of $Cu_3(HHTT)_2$ films prepared from same cycle number but different precursors concentration and solvent.

Condition	Thickness (nm)	RMS Surface Roughness (nm)	Roughness-to-Thickness Ratio (%)
5 mM ($Cu(OAc)_2$)/0.5 mM (HHTT) (Ethanol)	227	11.8	5.21
1 mM ($Cu(OAc)_2$)/0.1 mM (HHTT) (Ethanol)	132	4.86	3.68
0.2 mM ($Cu(OAc)_2$)/0.02 mM (HHTT) (Ethanol)	21	0.882	4.20
1 mM ($Cu(OAc)_2$)/0.1 mM (HHTT) (IPA)	71	4.12	5.80
1 mM ($Cu(OAc)_2$)/0.1 mM (HHTT) (DMF)	31	8.1	26.1

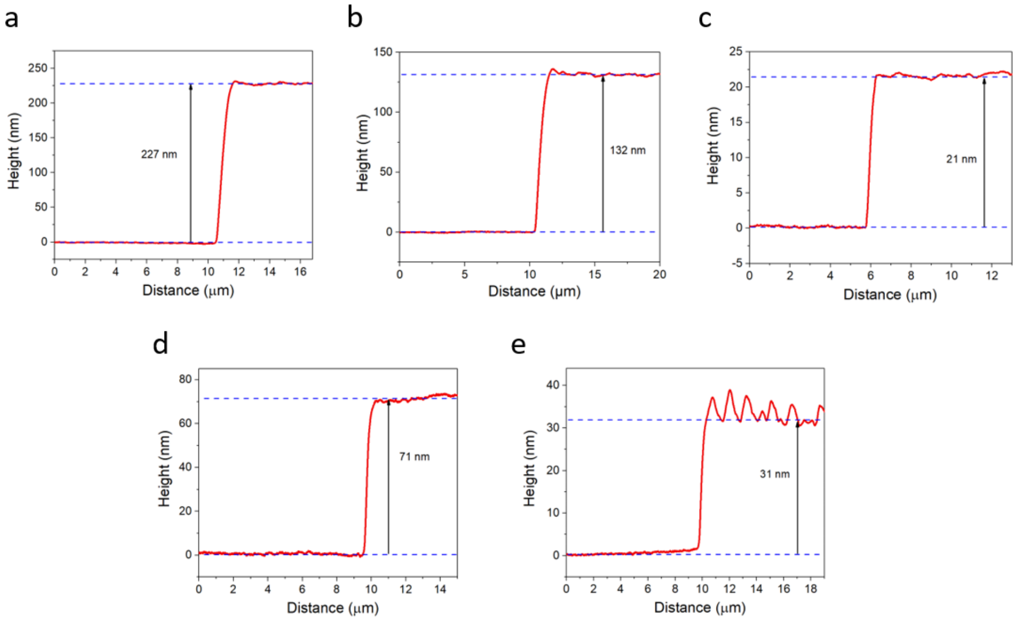

Figure 5.2. Thickness of 12-cycle $Cu_3(HHTT)_2$ thin films prepared from various conditions. (a) 5 mM ($Cu(OAc)_2$)/0.5 mM (HHTT) (Ethanol);(b) 1 mM ($Cu(OAc)_2$)/0.1 mM (HHTT) (Ethanol); (c) 0.2 mM ($Cu(OAc)_2$)/0.02 mM (HHTT) (Ethanol); (d) 1 mM ($Cu(OAc)_2$)/0.1 mM (HHTT) (IPA). (e) 1 mM ($Cu(OAc)_2$)/0.1 mM (HHTT) (DMF).

To obtain high-quality 2D c-MOF films, the processing conditions have been optimized. First, we used an ethanolic solution to prepare the films since ethanol is a common solvent for fabricating many 2D c-MOF thin films.[43, 108] The concentration of precursor solutions was tuned to three levels, including 5 mM ($Cu(OAc)_2$)/0.5 mM (HHTT), 1 mM ($Cu(OAc)_2$)/0.1 mM (HHTT) and 0.2 mM ($Cu(OAc)_2$)/0.02 mM (HHTT). Next, the solvent effect on thin film growth was studied by replacing ethanol with isopropyl alcohol (IPA) and DMF. The thicknesses of the films under various conditions after 12-cycle growth are depicted in **Figure 5.2** and listed in **Table 5.1**. It is reasonable to find that the film thickness increases with precursor concentrations. In terms of the solvent effect, the films prepared from ethanol show the fastest growth rate while DMF the slowest, which could be attributed to the difference in precursor solubility. It was found that it takes the longest time (~30 min) to completely dissolve HHTT in ethanol under continuous stirring, whereas HHTT can be dissolved almost instantaneously in DMF. The intermolecular forces experienced by precursor molecules in solvent can affect their tendency to adsorb on a substrate.[109] With a high solubility, the strong intermolecular interactions between precursor and solvent molecules make HHTT molecules more difficult to be adsorbed on a substrate. Therefore, it is reasonable to find that ethanol solvent provides the fastest grow rate among the three.

AFM images for the films are shown in **Figure 5.1c** and **5.3**. The thickness, surface roughness and roughness-to-thickness ratio of the films are presented in **Table 5.1** in the Supporting Information. Films prepared at different concentrations exhibit similar roughness-to-thickness ratios. Ethanol and IPA yield films with similar roughness-to-thickness ratios, while DMF results in a much higher roughness-to-thickness ratio. Such observation could be correlated to the different sizes of solvent molecules. It has been reported that the morphology of c-MOF films can be significantly changed by solvents with different molecular sizes.[110] During crystal growth, solvent molecules can incorporate into the pores of $Cu_3(HHTT)_2$ as guest molecules and act as a template.[110] Larger solvent molecules which have bigger steric hindrance lead to a more pronounced template effect. If the template effect is too large, uniform growth of the desired phase of 2D c-MOF could be significantly hindered and the resultant films would become highly inhomogeneous. Such effect explains the high roughness-to-thickness ratio in DMF-derived films.

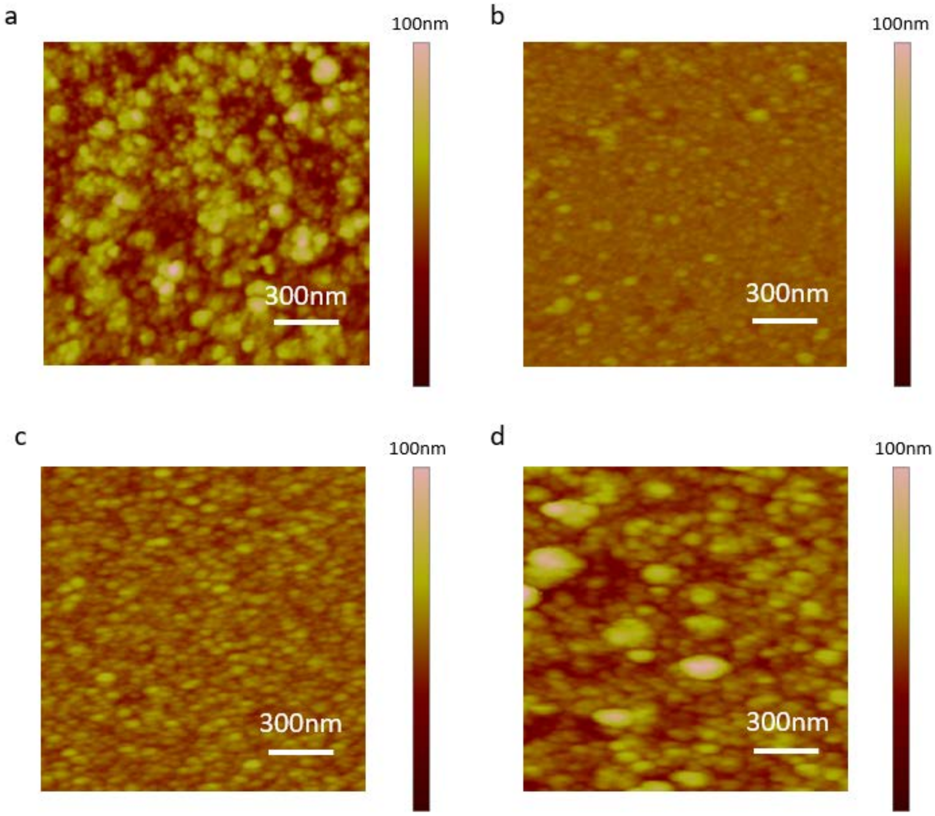

Figure 5.3. AFM images of 12-cycle $Cu_3(HHTT)_2$ thin films with different conditions. (a) 5 mM $(Cu(OAc)_2)$/0.5 mM (HHTT) ethanolic solutions. Thickness: 230 nm. (b) 0.2 mM $(Cu(OAc)_2)$/0.02 mM (HHTT) ethanolic solutions. Thickness: 20 nm. (c) 1mM $(Cu(OAc)_2)$/0.1mM (HHTT) IPA solutions. Thickness: 70 nm. (d) 1 mM $(Cu(OAc)_2)$/0.1 mM (HHTT) DMF solutions. Thickness: 30 nm.

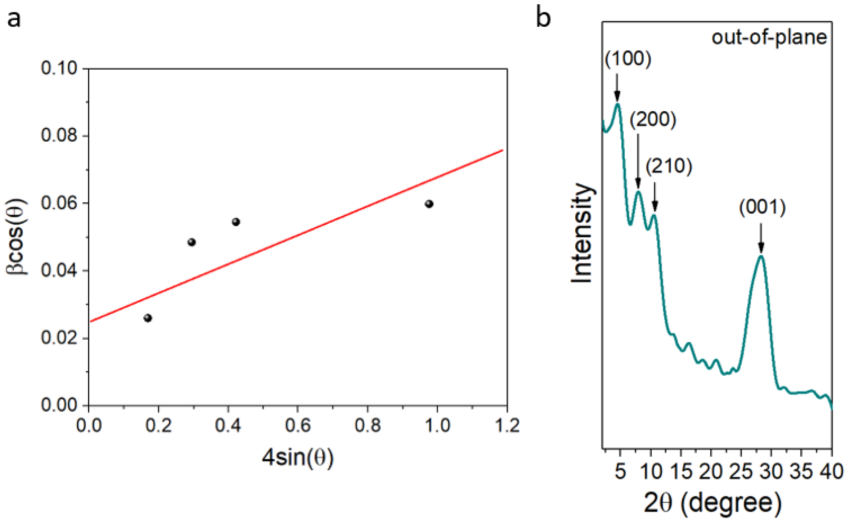

Figure 5.4. Supplementary XRD results of $Cu_3(HHTT)_2$ thin films. (a) W-H plot of $Cu_3(HHTT)_2$. (b) Out-of-plane GIXRD spectra of a film prepared from 5 mM ($Cu(OAc)_2$)/0.5 mM (HHTT) Ethanolic solutions. Thickness: 230 nm.

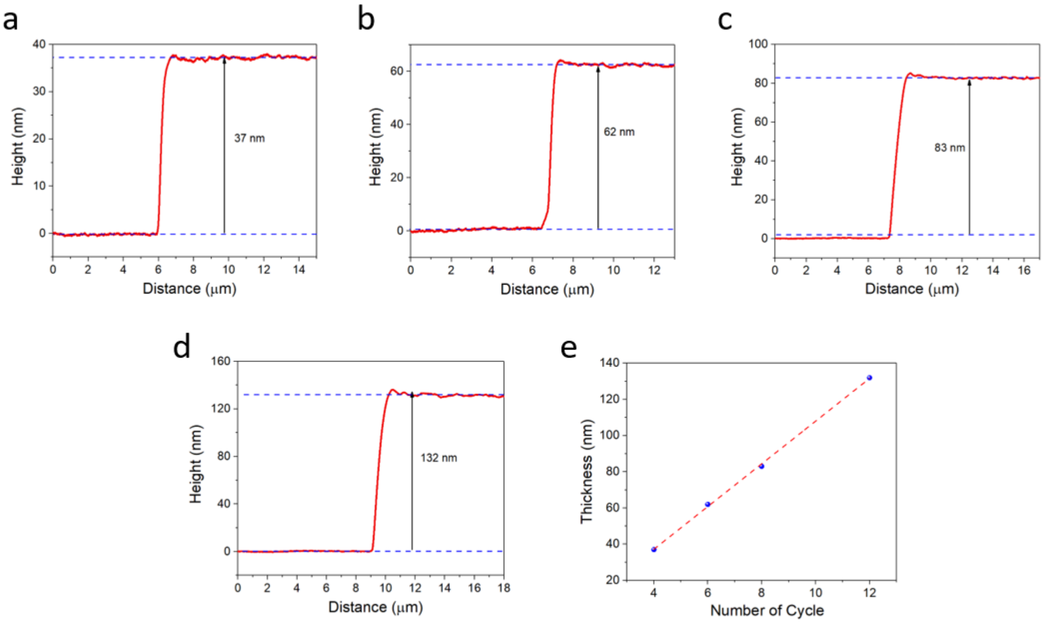

Figure 5.5. Thicknesses of $Cu_3(HHTT)_2$ thin films prepared from 1 mM ($Cu(OAc)_2$)/0.1 mM (HHTT) ethanolic solutions with different number of growth cycles. (a) 4 cycles;(b) 6 cycles; (c) 8 cycles; (d) 12 cycles. (e) Thickness as a function of number of growth cycle.

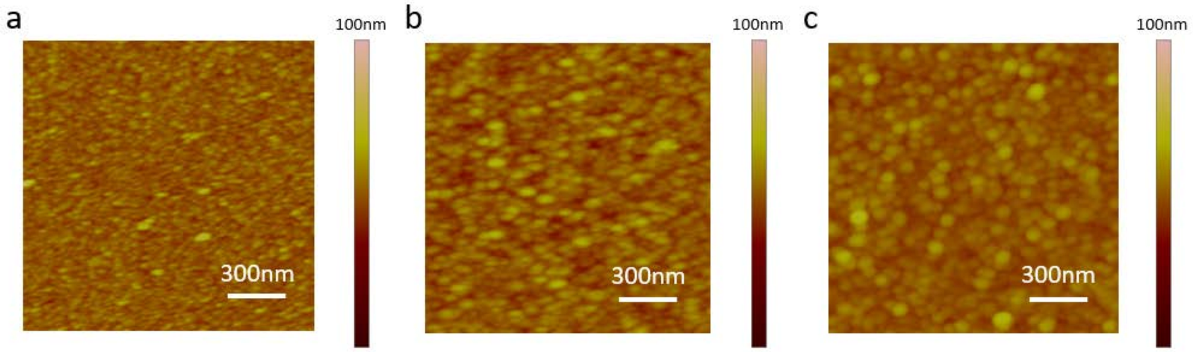

Figure 5.6. AFM images for $Cu_3(HHTT)_2$ films prepared from 1 mM ($Cu(OAc)_2$)/0.1 mM (HHTT) ethanolic solutions of different thicknesses. (a) 4 cycles; Thickness: 40 nm. (b) 6 cycles; Thickness: 60 nm. (c) 8 cycles. Thickness: 80 nm.

Table 5.2. Thickness, RMS surface roughness and roughness-to-thickness ratio of $Cu_3(HHTT)_2$ films with different cycle numbers using the same 1 mM ($Cu(OAc)_2$)/0.1 mM (HHTT) ethanolic solutions.

Condition	Thickness (nm)	RMS Surface Roughness (nm)	Roughness-to-Thickness Ratio (%)
4 cycles	37	1.26	3.4
6 cycles	62	2.43	3.92
8 cycles	83	2.98	3.59
12 cycles	132	4.86	3.68

The orientation of 2D c-MOF films can be revealed by grazing incidence X-ray diffraction (GIXRD) measurements. **Figure 5.1d** depicts the out-of-plane (left) and in-plane (right) XRD diffraction patterns for a film prepared from 1 mM ($Cu(OAc)_2$)/0.1 mM (HHTT) ethanolic solution on a SiO_2/Si wafer. The peak assignments are done by checking the peak positions from previously reported powder XRD patterns.[21, 44, 94] Only one peak at $2\theta = 27.9^{\circ}$ can be observed in the out-of-plane XRD pattern, which can be assigned to (001) diffraction. In contrast, three peaks at 2θ = 4.2°, 8.5°, 13.6° can be found in the in-plane XRD pattern, which can be indexed as (100), (200), (220) planes. The obtained XRD peaks are all consistent with those reported in the literature.[21, 44, 94] The significant difference between in-plane and out-of-plane XRD profiles indicates the highly oriented $Cu_3(HHTT)_2$ thin films prepared by this method. The relatively weak XRD signal can be attributed to small grain size and thin thickness of the film, which is similar to XRD spectra of other 2D c-MOF films.[108, 111] All the peaks can be fitted very well with Gaussian functions. Based on uniform deformation model (UDM) of Williamson-Hall (W-H) method (See Experimental Section and **Figure 5.4a**)[112], the average crystalline size and mircostrain are estimated to be 6.3 nm and 4.1% respectively, which indicates the polycrystalline nature of the $Cu_3(HHTT)_2$ films. The relatively large macrostrain could be attributed to the soft property of $Cu_3(HHTT)_2$ which has a large amount of organic ligands. In comparison, a film prepared from 5 mM ($Cu(OAc)_2$)/0.5 mM (HHTT) ethanolic solution shows random orientation because its out-of-plane XRD pattern shows several peaks, including (100), (200), (210) and (001) peaks at 2θ = 4.2°, 8.4°, 10.6°, 27.9°, respectively (**Figure 5.4b**). Hence, highly oriented films can be formed only with a slow enough crystallization process so that the orientation of a new c-MOF layer can be directed by the previous one through interlayer π-π interactions during the immersion steps. Films prepared from 1 mM ($Cu(OAc)_2$)/0.1 mM (HHTT) ethanolic solutions exhibit the best quality and reasonable growth speed, which is the optimum growth condition for the 2D c-MOF films. As shown in **Figure 5.5**, the growth speed of the film at this condition is estimated to be ~11nm/cycle. The roughness-to-thickness ratio is about 3.5% for all measured thicknesses, as shown in **Figure 5.6** and **Table 5.2**.

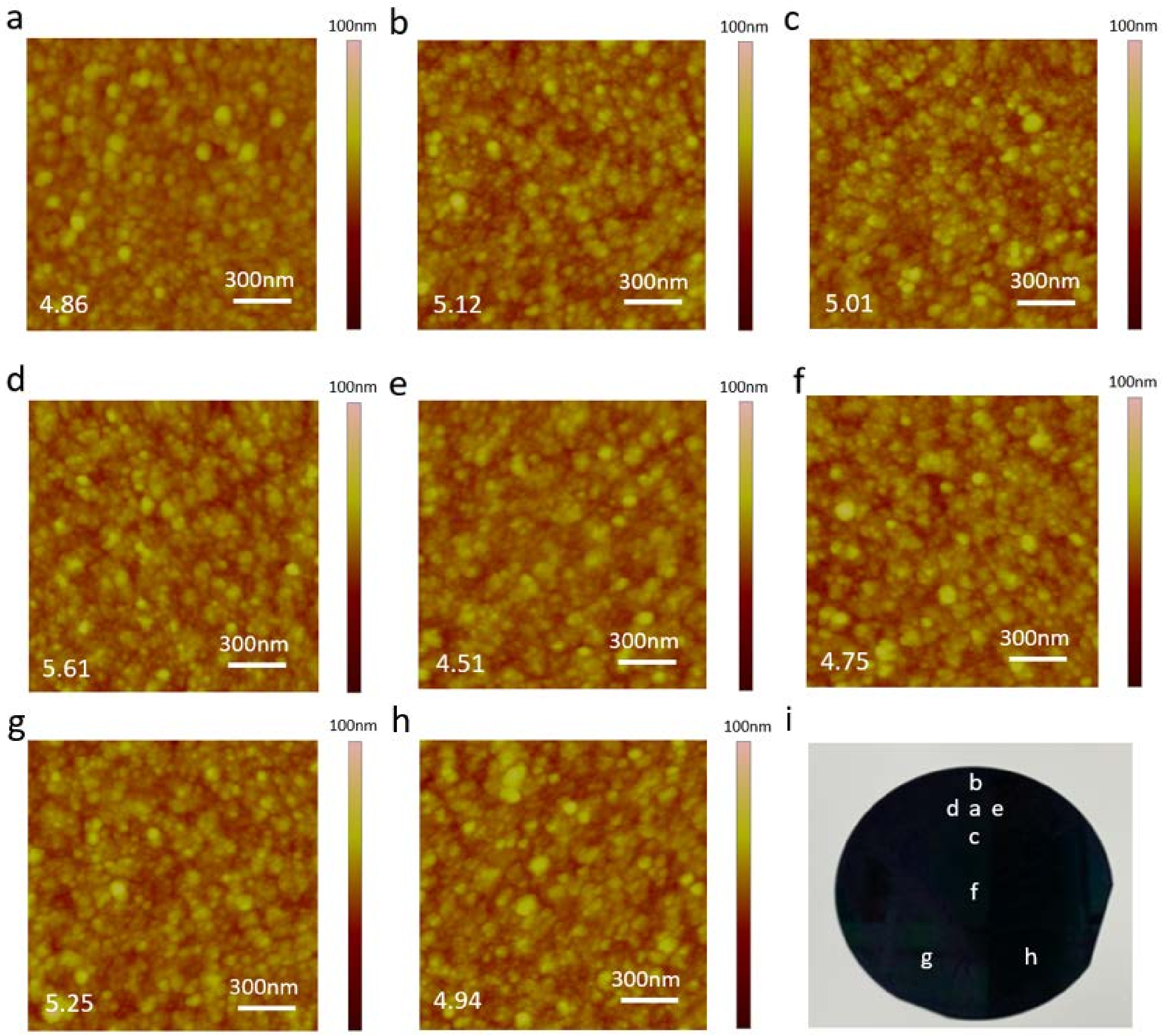

Figure 5.7. AFM images for a 12-cycle $Cu_3(HHTT)_2$ film prepared from 1 mM ($Cu(OAc)_2$)/0.1 mM (HHTT) ethanolic solutions taken at different positions on a 4-inch SiO_2/Si wafer. Thickness: 130 nm. The numbers at bottom-left corners of the AFM images are the RMS roughness values (in nm), respectively. (a-h) AFM images taken at different positions on the wafer. (i) A photograph of the wafer-scale film to show the positions where respective AFM images (a-h) are taken.

The uniformity of a large-area 2D c-MOF film on a 4-inch SiO_2/Si wafer was examined under AFM, which indicated identical surface roughness at different positions on the wafer

(**Figure 5.7**). In addition, smooth surfaces without any pinhole can be observed under SEM (SEM) on all samples with different thicknesses (Figure **5.8**). High resolution transmission electron microscopy (HRTEM) was further employed to observe the crystal structure of the films detached from substrates (**Figure 5.1e**). The corresponding FFT image clearly shows a hexagonal crystal structure of the film.

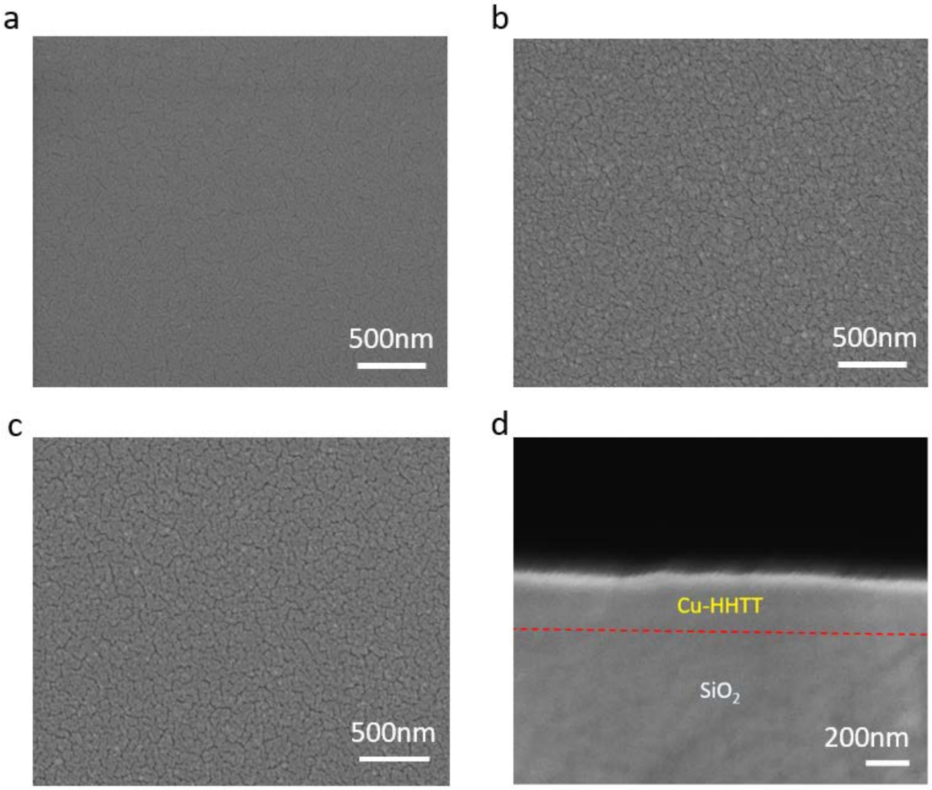

Figure 5.8. SEM images for (a) 4-cycle (thickness: 40 nm), (b) 8-cycle (thickness: 80 nm) and (c) 12-cycle (thickness: 130 nm) $Cu_3(HHTT)_2$ films prepared from 1 mM ($Cu(OAc)_2$)/0.1 mM (HHTT) ethanolic solutions. (d) cross-section SEM for a 12-cycle $Cu_3(HHTT)_2$ film prepared under similar conditions.

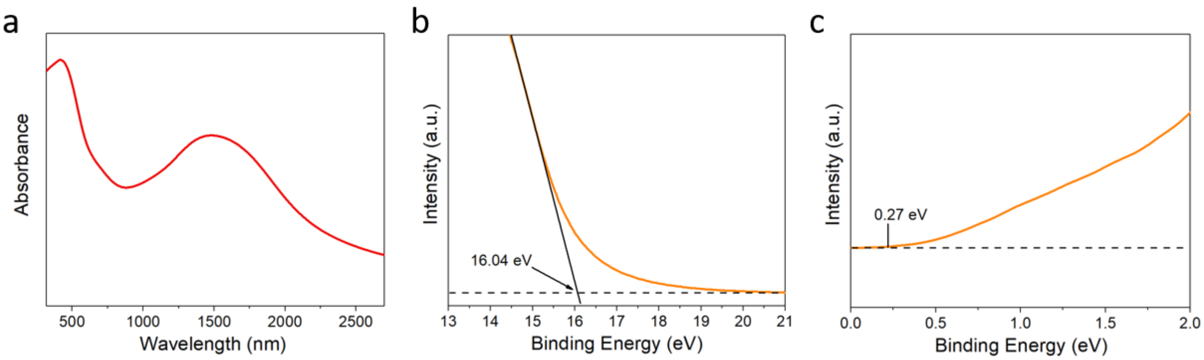

Figure 5.9. (a) Absorption spectrum of a $Cu_3(HHTT)_2$ film. Thickness: 130 nm. UPS spectrum in the (b) secondary cut-off region and (c) valence band region of a $Cu_3(HHTT)_2$ film on an ITO substrate.

Figure 5.**1f** and **5.9a** show the absorption spectra and the corresponding Tauc plot ($(\alpha h\nu)^2 \sim h\nu$) of a $Cu_3(HHTT)_2$ thin film, where α is the absorption coefficient, ν frequency and h Planck's constant. Being different from the results reported before,[21, 44, 94] the 2D c-MOF shows a narrow band gap of only ~0.55eV. The linear relationship between $(\alpha h\nu)^2$ and the photon energy $h\nu$ at the absorption edge clearly indicates the direct bandgap nature of $Cu_3(HHTT)_2$. The major reason for the different bandgap energies and absorption spectra between our work and the previously reported results could be attributed to the different crystallinity and quality of the samples.

Ultraviolet photoelectron spectroscopy (UPS) (**Figure 5.9b** and **c**) was employed to investigate the position of Fermi level and valence band edge. The secondary cut-off region of UPS spectra (**Figure 5.9b**) indicates that the binding energy of $Cu_3(HHTT)_2$ is 16.04 eV. With an UV light source of 21.2 eV, the Fermi level is calculated to be 5.16 eV, which is comparable with the work function of Au. Besides, the valence band edge is below Fermi level by ~0.27 eV, as indicated by the valence band region of UPS spectra (**Figure 5.9c**). Hence, the Fermi level is close to the mid-gap of the $Cu_3(HHTT)_2$ films.

5.2.2 Transport Mechanisms in $Cu_3(HHTT)_2$ thin films

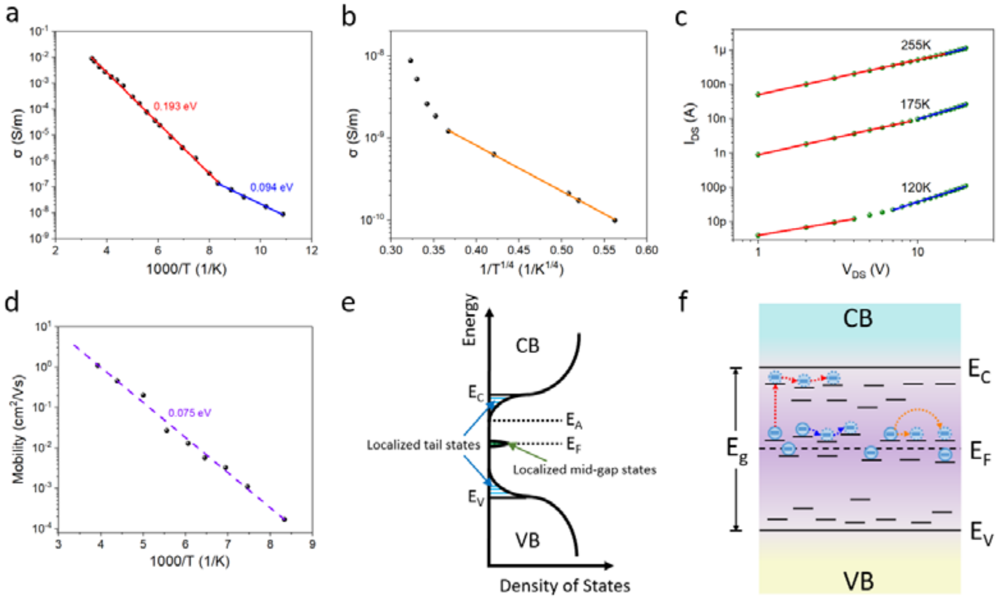

Figure 5.10. Temperature dependent transport property and derived schematic band diagrams. (a) σ vs. 1000/T relationship in two regions with different thermal activation energy (300K-90K). (b) ln(σ) vs. $1/T^{1/4}$ relationship at low T (90K-10K), showing the Mott variable range hopping behavior (55-10K). (c) Double-logarithm plot of I-V curves at various temperatures. The red and blue regions correspond to ohmic and space-charge-limited current (SCLC) conductions, respectively. (d) SCLC Mobility vs. 1000/T relationship (255K-120K). (e) Schematic band diagram used to explain the temperature-dependent conductivity. (f) Illustration of different transport mechanisms. Red, blue and orange dashed lines correspond to carrier transport between tail states by nearest-neighbor hopping, nearest neighbor hopping between mid-gap states and variable-range hopping between mid-gap states near Fermi level, respectively.

To further confirm the semiconducting property and verify its transport mechanisms of 2D c-MOF $Cu_3(HHTT)_2$, we characterized the DC conductivity (σ) of a film as a function of temperature (T). The $Cu_3(HHTT)_2$ film was grown on a SiO_2/Si substrate with pre-patterned two Au electrodes with the channel length and width of 5 and 800 μm, respectively. As shown in **Figure 5.10a**, the rapid drop of conductivity from 295K to 120K shows a thermal activation behavior, which is a characteristic of a semiconductor.[113] Another thermal activation process with a lower activation energy can be found between 120K and 90K. The temperature dependent conduction processes can be understood under the framework of polycrystalline semiconductors. From 295K to 120K, the activation process is due to thermal activation of carriers from localized mid-gap states close to the Fermi level (E_F) to localized tail states near conduction band edge (E_C) and carrier hopping between nearest tail states. The conductivity in this temperature region can be described by:[113]

$$\sigma = \sigma_0 \exp\left(-\frac{E_{a1}}{k_B T}\right),$$

$$E_{a1} = E_A - E_F + W_1,$$

where σ_0, k_B, E_A, are a prefactor, Boltzmann constant, minimum tail state energy, respectively, W_1 is the average nearest-neighbor hopping activation energy between tail states, respectively. E_{a1} is extracted to be 0.193 eV, which is much smaller than the band gap energy.

Another thermal activation process from 120K to 90K is due to nearest-neighbor hopping of carriers between localized states near Fermi level with the following relationship:[114]

$$\sigma = \sigma_1 \exp\left(-\frac{E_{a2}}{k_B T}\right),$$

$$E_{a2} = W_2,$$

where σ_1 is another prefactor and W_2 average nearest-neighbor hopping activation energy between the trap states, respectively. W_2 is extracted to be 0.094 eV, which is consistent with theoretical values.[115]

As shown in **Figure 5.10b**, another distinct conduction mechanism dominates at a lower temperature region (55 K-10 K), which shows a $\ln\sigma \propto 1/T^{1/4}$ dependence that can be assigned to Mott variable-range hopping.[116] At the low temperature range, the carriers in mid-gap states near Fermi level can only perform phonon-assisted hopping to another mid-gap states with similar energy levels, which are not necessarily the nearest neighbors.[113, 116]

The effective electron mobility in the temperature range corresponding to carrier hopping between nearest tail states is also investigated. When the bias voltage is high enough, a nonlinear current-voltage relationship can be observed, which can be attributed to space-charge-limited current (SCLC) of the device. The I-V curves are fitted by SCLC equation (**Figure 5.10c**):[117]

$$I = \frac{9\varepsilon_0\varepsilon_r\mu A V^2}{8L^3},$$

where ε_0 is vacuum permittivity, ε_r is dielectric constant, μ is mobility, A is channel cross-section, V is potential drop between two electrodes, L is channel length. The dielectric constant is assumed to be 1.5 since the typical values of dielectric constant for MOFs range from 1.2-2.[118] As shown in **Figure 5.10d**, the mobility shows a thermally activated behaviour with an activation energy of 0.075 eV, indicating that the carrier transport is a localized hopping process.[119]

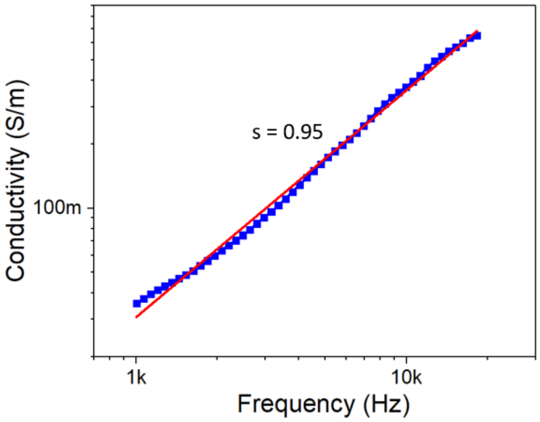

Figure 5.11. Double-logarithm plot of AC Conductivity vs. frequency and the linear fitting.

AC conductivity as a function of frequency was then conducted to further verify the conduction mechanism of the 2D c-MOF film at room temperature. We found that the frequency dependent AC conductivity follows the below expression from 1kHz to 20kHz:[120]

$$\sigma(\omega) \propto A\omega^{s}, \tag{6}$$

where A is a constant, ω is angular frequency and s is a characteristic parameter. Such relationship can be found in many hopping systems with s ranging from 0.5 to 1, depending on the interactions between charge carriers and their surrounding lattices.[120] It is found from the experimental data and linear fitting that s equals to 0.95 (**Figure 5.11**, Supporting Information) in our $Cu_3(HHTT)_2$ film, which is a clear indication of phonon-assisted hopping process among localized tail states in the 2D c-MOF film at room temperature. Notably, such fitting cannot be perfect because it is an empirical model for complicated hopping systems.

From the above analysis, a schematic band diagram is depicted in **Figure 5.10e**. The carrier transport mechanisms are graphically illustrated in **Figure 5.10f**. There are three different carrier transport processes from high to low temperatures, including (1) phonon-assisted hopping between tail states; (2) nearest-neighbor hopping between mid-gap trap states near the Fermi level, and (3) variable-range hopping between mid-gap trap states. Therefore, the conduction mechanism of $Cu_3(HHTT)_2$ is dominated by different conduction processes at three different temperature regions.

5.2.3 PD Performance

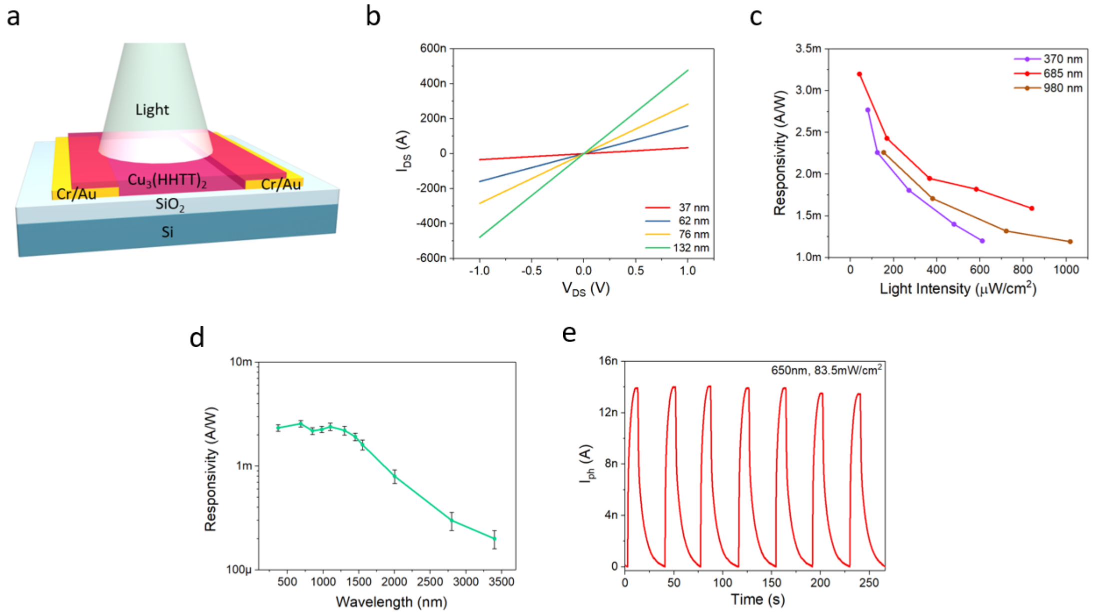

Figure 5.12. Device performance of PDs based on $Cu_3(HHTT)_2$ thin films. (a) schematic diagram of the device structure. (b) I-V curves of the devices with different cycle numbers. The films with 4, 6, 8, 12 cycles have the thicknesses of 37nm, 62nm, 76nm, and 132 nm, respectively. (c) Responsivity as a function of light intensity for three different wavelengths. (d) Spectral response for different light wavelengths from 370nm to 3400nm. Error bars were calculated from 4 devices. (e) Transient response for a PD under three 650 nm laser light on-off cycles.

Next, the performance of PDs based on $Cu_3(HHTT)_2$ films shown in **Figure 5.12a** was characterized. All the device measurements were conducted in a glove box filled with inert N_2. As shown in **Figure 5.12b**, the channel current of the device increases with the increase of the film thickness. In the first few cycles, the conductance is relatively low, which is presumably due to the substrate effect like the interfacial trap states and the carrier interaction with the substrate.[121] As the cycle number further increases, it is reasonable to find that the film conductance is approximately proportional to the film thickness. Notably, the devices with different thicknesses all exhibit linear I-V curve (**Figure 5.12b** and **5.13**), indicating Ohmic contacts between Au electrodes and $Cu_3(HHTT)_2$ layers. As expected, the film fabricated by 1 mM $(Cu(OAc)_2)$/0.1 mM (HHTT) ethanolic solution yields the highest current due to its ideal growth speed and the best quality. The relatively thinner films prepared from lower precursor concentration and unoriented films prepared from higher precursor concentrations (as indicated by XRD spectra, **Figure 5.4b**) both result in lower currents. Notably, the current of the device prepared from IPA solvent is similar to that prepared from ethanol solvent for similar film thickness, indicating their similar film quality. On the other hand, it is reasonable to find that the rough and thin (31 nm) films prepared from DMF have much lower conductivity than the films prepared with ethanol and IPA.

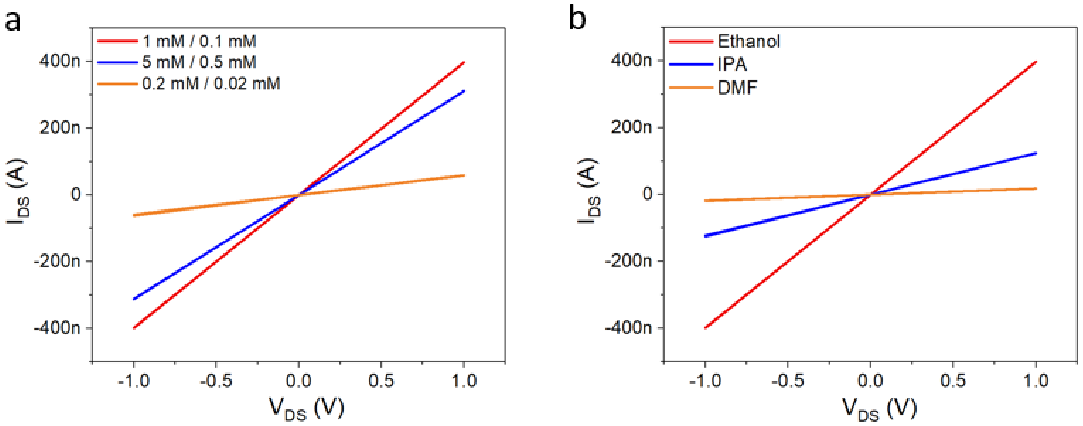

Figure 5.13. I-V curves of 12-cycle $Cu_3(HHTT)_2$ devices prepared under various conditions. (a) Different $Cu(OAc)_2$/HHTT concentrations;(b) different solvent.

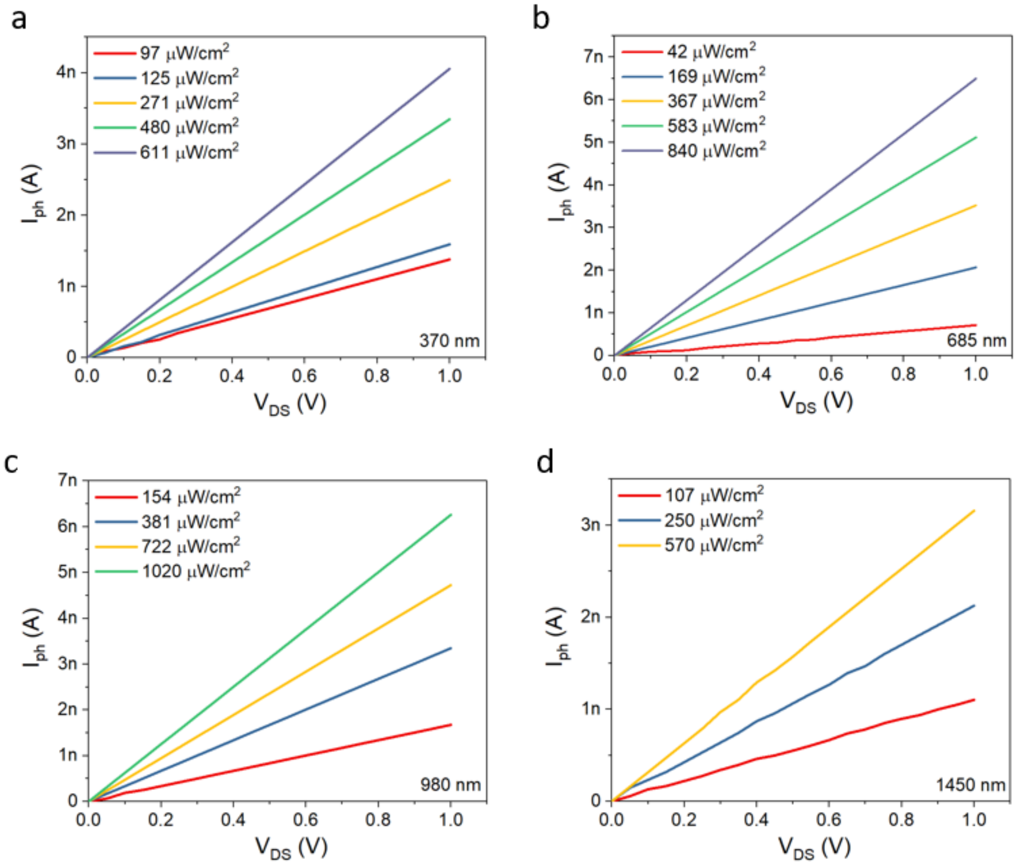

Figure 5.14. Photocurrent as a function of V_{DS} for various intensities under illumination of different wavelengths. (a) 370 nm. (b) 685 nm. (c) 980 nm. (d) 1450 nm.

The photo-response behavior of devices prepared under the optimum conditions with a film thickness of ~130 nm (12 cycles) was then characterized. The photocurrent increases with light intensity at different wavelengths (370 nm, 685 nm, 980 nm and 1450 nm) (**Figure 5.14**, Supporting Information). Responsivity is a parameter to quantify the sensitivity of a PD. **Figure 5.12c** shows the relationship between responsivity and light intensity for different wavelengths with the maximum responsivity of 3.2 mA/W under 685 nm illumination. The responsivity decreases with increase in light intensity at any wavelength, which can be attributed to faster carrier recombination under a higher light intensity due to the increased density of photo-carriers in the $Cu_3(HHTT)_2$ channel.

Table 5.3. Comparison of spectral response of solution-processed broadband PDs based on different materials.

Active Material	Spectral Range (nm)	Reference
Hybrid perovskite $FASnI_3$ (FA: formamidinium) film	370-980	[20]
2D c-MOF $Fe_3(THT)_2(NH_4)_3$	400-1575	[46]
Organic semiconductor poly(thiophene [1,2,5]thiadiazolo[3,4-g]quinoxaline(2-butyloctyl)) film	350-1400	[122]
quantum dots PbS film	800-1600	[123]
2D c-MOF $Cu_3(HHTT)_2$ film	370-3400	This work

Spectral response of a PD is critical to its applications. **Figure 5.12d** depicts the responsivity of a device as a function of wavelength under an identical light intensity of ~200 $\mu W/cm^2$. Remarkably, the device exhibits obvious photo-response across a broad wavelength range from UV (370nm) to MIR (3400nm), which significantly outperforms the reported solution-processed broadband PDs based on other 2D c-MOFs[46], quantum dots[123], hybrid perovskites[20] and organic semiconductors[124] (**Table 5.3**). Besides the wide range of applications in visible to near-infrared (NIR) range, PDs with MIR photo-response are useful in various applications, including thermal and medical imaging, air pollutant and dangerous chemical monitoring.[125]

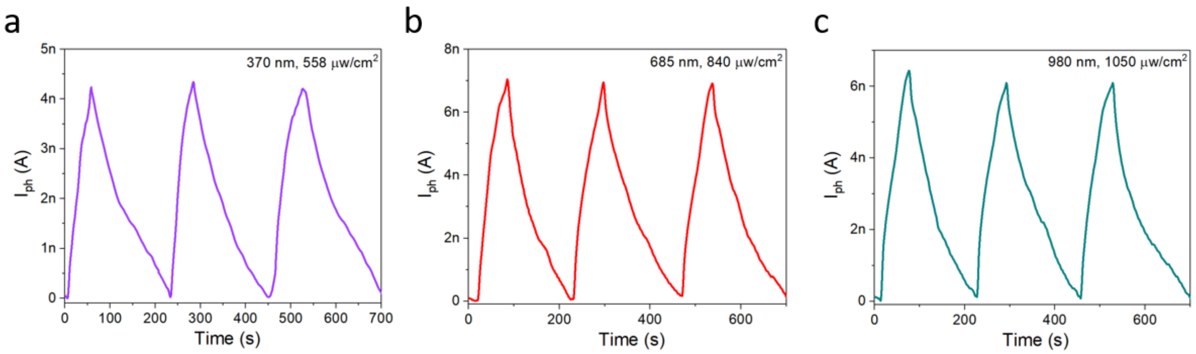

Figure 5.15. Transient response of the $Cu_3(HHTT)_2$ PD under three (a) 370 nm, (b) 685 nm and (c) 980 nm LED light on-off cycles.

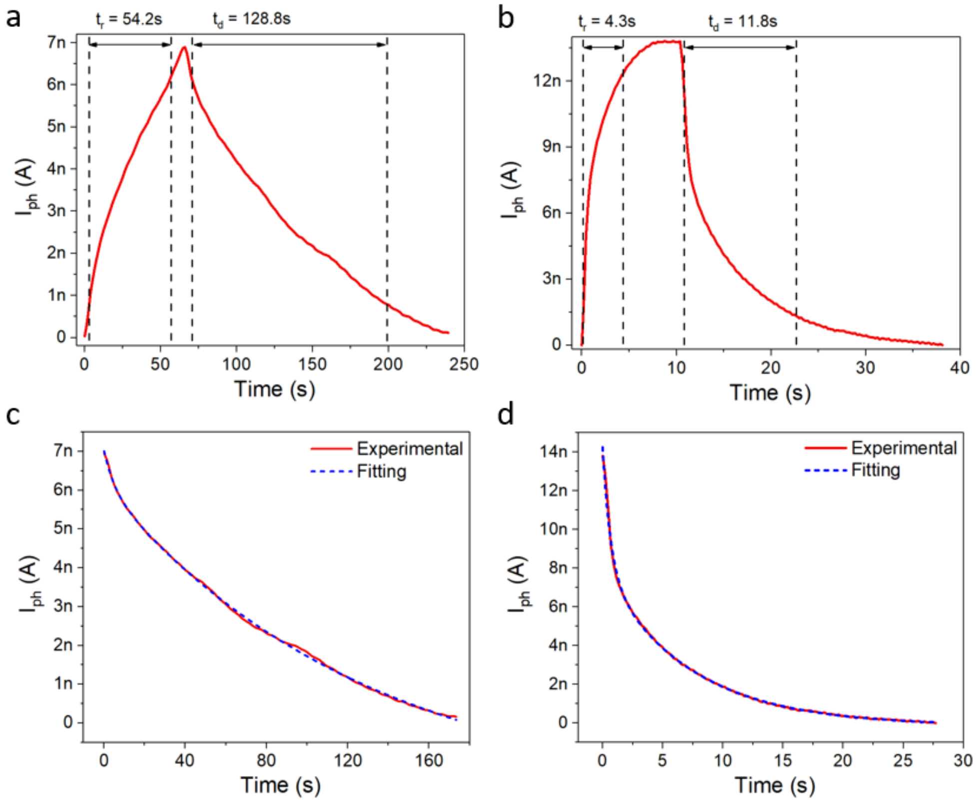

Figure 5.16. The transient responses of the $Cu_3(HHTT)_2$ PD under one light on-off cycle for (a) LED (685 nm, 840 μW/cm^2) and (b) laser (650 nm, 83.5mW/cm^2) illumination. (c) Decaying edge of the device under LED illumination and the exponential fitting curve. (d) Decaying edge of the device under laser illumination and the exponential fitting curve.

The responsivity remains almost unchanged in the short wavelength region while decreases with the increase of wavelength from 1450 nm to 3400nm. Considering the small band gap of $Cu_3(HHTT)_2$ with an absorption edge of ~2300 nm, the extended detection range can be attributed to the carriers excited from the mid-gap states to the conduction band or tail states. Notably, the spectral responses of four devices located at different positions of the SiO_2/Si substrate show little variation, further confirming the high uniformity of the 2D c-MOF film in a wafer scale.

Moreover, the 2D c-MOF PDs exhibit stable transient response for different wavelengths (**Figure 5.12e** and **5.15**). The transient responses of a device under light illuminations (685 nm: 840 μW/cm^2, 650 nm: 83.5mW/cm^2) have been characterized (**Figure 5.16a-b**). The rise and decay time, which are defined as the time duration of photocurrent changed from 10% to 90% and 90% to 10% of maximum, are indicated in the figures. It is obvious that the response is faster under higher light intensity. The decaying edges of the transient response under light illumination are fitted very well with a double exponential function:[49c]

$$I_{ph} = A_{d1} \exp\left(-\frac{t}{\tau_{d1}}\right) + A_{d2} \exp\left(-\frac{t}{\tau_{d2}}\right),$$

where A_{d1} and A_{d2} are magnitudes for the two decaying components, and τ_{d1} and τ_{d2} are the fast and slow relaxation times. As shown in **Figure 5.16d**, the extracted relaxation time τ_{d1} and τ_{d2} are 0.662s and 7.25s, respectively. The fast component could be due to the carrier recombination between conduction band and valance band, whereas the slow component could be attributed to the carrier recombination between localized states. Similar observation was previous found in PDs based on inorganic 2D materials with a similar band structure.[126]

5.2.4 Flexible PD Performance

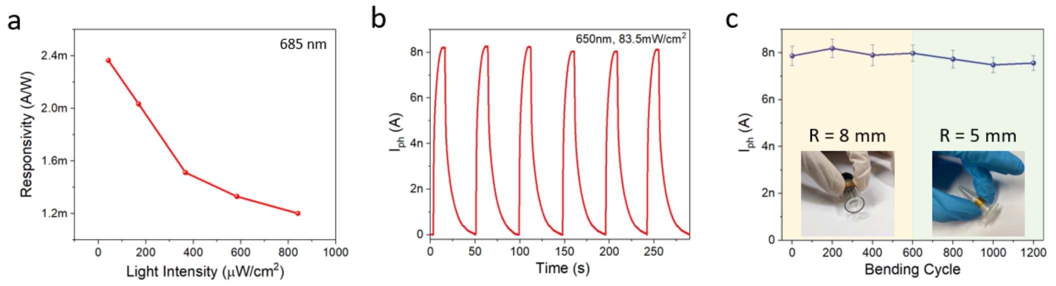

Figure 5.17. **Device performance of flexible PDs based on $Cu_3(HHTT)_2$ thin films.** (a) Responsivity as a function of light intensity for 685nm light wavelength. (b) Transient response for a flexible PD under three 650 nm laser light on-off cycles. (c) photocurrent of a device as a function of bending cycle under bending tests. Error bars are calculated from 4 devices. Inset: the photographs demonstrate the device subjected to bending tests.

Flexible PDs based on $Cu_3(HHTT)_2$ thin films can be fabricated by were replacing SiO_2/Si substrates with 50μm-thick polyimide (PI) substrates. The similar performance of the devices fabricated on PI and SiO_2/Si (**Figure 5.17a-b**) indicates the comparable quality of the 2D c-MOF films prepared on the two different substrates. Bending tests were performed on the devices to study the performance against mechanical deformation. The tests involve bending of the devices against a glass bottle with 8 mm radius for 600 times and then a tube with 5 mm radius for another 600 times. As depicted in **Figure 5.17c**, photo-response remains unchanged after 600 times of bending with 8 mm radius and show only slight decrease after additional 600 times of bending with 5mm radius, indicating the excellent mechanical stability of the devices.

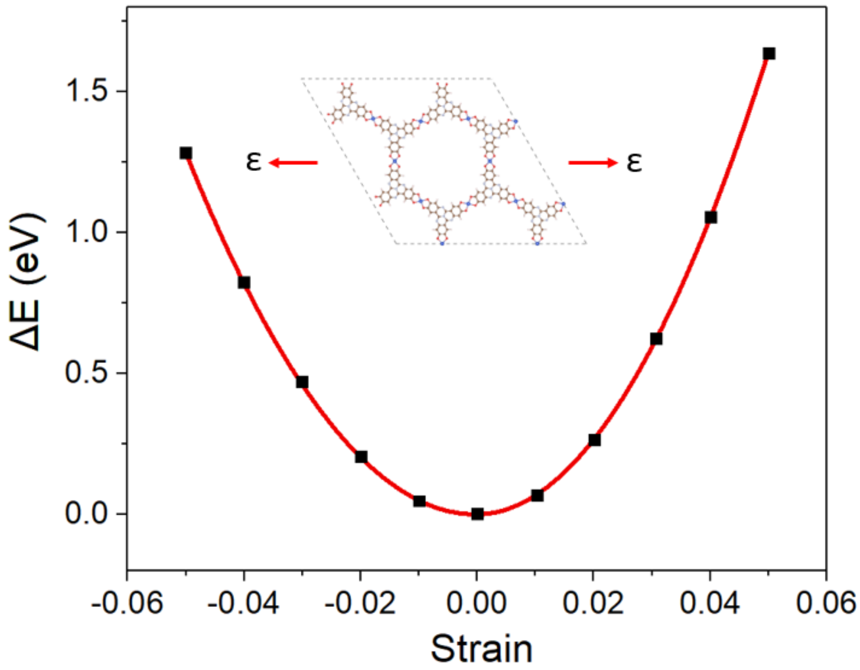

Figure 5.18. Calculated energy difference of a $Cu_3(HHTT)_2$ unit cell as a function of applied strain along **a** and **b** directions (they are symmetric). Solid line is the parabola fitting, which gives Young's modulus. A 2x2x1 cell of $Cu_3(HHTT)_2$ is shown in the figure.

Table 5.4. Comparison of Young's modulus of some typical and emerging optoelectronic materials

Material	Young's modulus (GPa)	Reference
Si	169	[127]
GaAs	116	[127]
$MAPbI_3$ (MA: Methylammonium)	22.8	[128]
monolayer MoS_2	238/270	[129]
graphene	1050	[130]
poly(3-hexylthiophene) (P3HT)	0.1-1	[131]
2D c-MOF $Cu_3(HHTT)_2$	34.6	This work

To gain more insight into the mechanical property of $Cu_3(HHTT)_2$, we calculated its Young's modulus (Y) by performing Density Functional Theory (DFT) simulation (see Computational Methods in Experimental Section and **Figure 5.18**). The calculated Y is 34.6 GPa, which is much lower than traditional optoelectronic materials[127] and is among the lowest in emerging optoelectronic materials[128-131] (**Table 5.4**). Such a low value of Y explains the high flexibility of the devices and further demonstrates their possible applications in flexible electronics.

5.2.5 Optical Synapse Performance

Inspired by the relatively long relaxation time under low light intensity in our devices, an optical synapse based on $Cu_3(HHTT)_2$ is demonstrated (**Figure 5.19a**). The photocurrent of the device can be defined as postsynaptic current change (ΔPSC). **Figure 5.19b** shows the gradual decrease of ΔPSC after light illumination (685nm, 840μW/cm^2), which is analogous to the short-term plasticity (STP) behavior in biological synapse. The persistent photocurrent is due to the trapping of photo-carriers by defects, as explained above. Paired pulse facilitation (PPF) is an important form of STP in recognizing and decoding temporary information.[132] Such behavior can be simulated by applying two consecutive optical pulses (**Figure 5.19c**). The ΔPSC after the second pulse is higher than that after the first pulse, which is due to the accumulated photo-carriers trapped in $Cu_3(HHTT)_2$ film.

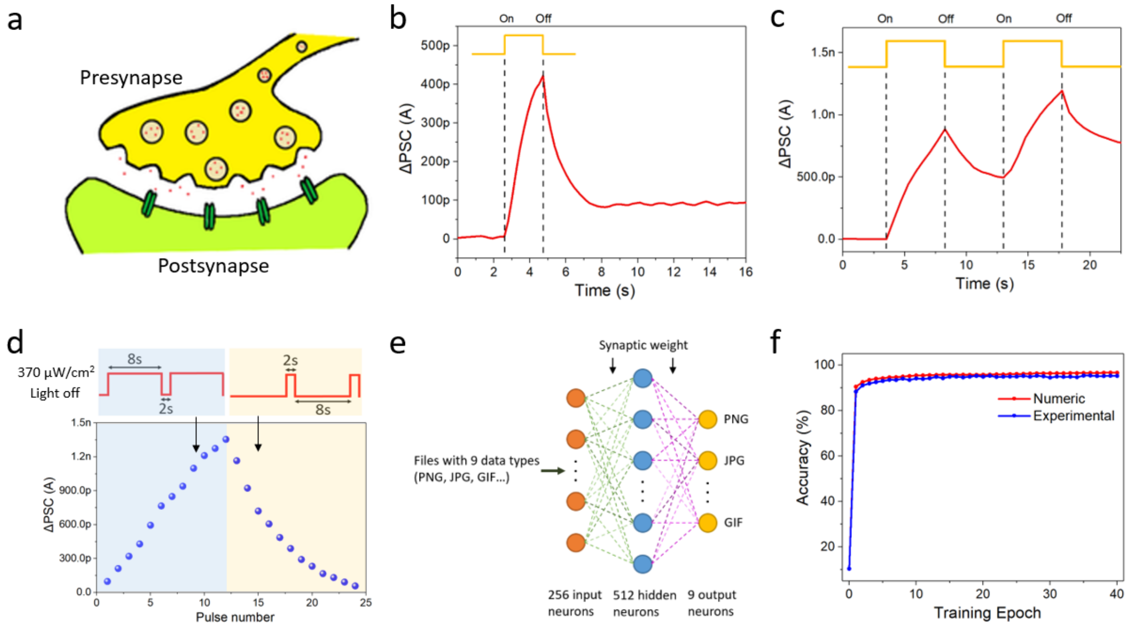

Figure 5.19. Device performance of an optical synapse device based on $Cu_3(HHTT)_2$ thin films. (a) Schematic illustration of a biological synapse. (b) Gradual decrease of ΔPSC after triggered by an optical signal (685 nm, 840μW/cm^2). (c) PPF behavior under stimulation of two consecutive optical signals. (d) LTP/LTD characteristics under continuous light on/off cycles (685nm, 370 μW/cm^2). On/off times of 8s/2s and 2s/8s are used to mimic LTP and LTD side of the curve, respectively. (e) Schematic illustration of the three-layer neural network for data type analysis. (f) Data type recognition accuracy as a function of training epoch.

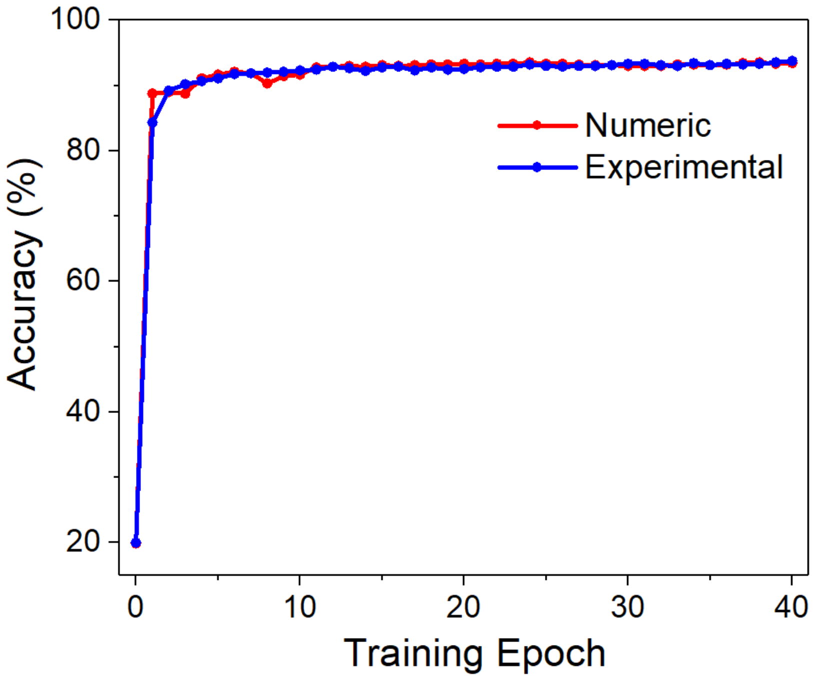

Figure 5.20. Recognition accuracy for handwritten digits with 8 × 8 pixels as a function of training epoch.

A LED (685nm, 370 µW/cm^2) with the same on/off frequency (0.1Hz) but different duty cycle was used to simulate LTP and LTD. Specifically, on/off times of 8s/2s and 2s/8s are implemented to mimic the long-term potentiation (LTP) and long-term depression (LTD), respectively. **Figure 5.19d** depicts LTP and LTD characteristics of the $Cu_3(HHTT)_2$ optical synapse at relatively high ΔPSC levels. The accuracy and efficiency for recognition are crucial for neuromorphic computing.[133] To further demonstrate the potential of the $Cu_3(HHTT)_2$-based optical synapse and provide an objective comparable data, the LTP/LTD characteristics of the device are employed to simulate the performance of a three-layer (256 × 512 × 9) ANN with one hidden layer. Synaptic weights are defined as different ΔPSC levels of the potentiation and the depression behaviors. Such network is adopted to perform data type recognition after training by a Sandia file classification dataset via backpropagation (**Figure 5.19e**). As shown in **Figure 5.19f**, the classification accuracy of $Cu_3(HHTT)_2$ synapse achieves over 90% with 7 training epochs. It finally reaches 92.1% after 40 training epochs, which is only 1.3% lower than the value obtained by ideal numerical training. Another ANN simulation with a smaller network size (64 × 36 × 10) was performed on the "Optical Recognition of Handwritten Digits" dataset consisting of 8×8 pixels handwritten digits (**Figure 5.20**). Again, the devices show recognition accuracy very close to ideal numerical calculations. The obtained data recognition efficiencies are among the best when compared to other synaptic devices used in ANN simulation.[134] These results indicate the great potential of our $Cu_3(HHTT)_2$ optical synapse for future applications.

5.2.6 Ultrathin $Cu_3(HHTT)_2$ Film as HTL in Perovskite Solar Cells

Furthermore, the $Cu_3(HHTT)_2$ film can be employed as hole transporting layer in perovskite solar cell. The 2D c-MOF films prepared by the self-assembly deposition method are used in ideal-bandgap Pb−Sn mixed PSCs. The ultrasmooth surface of the $Cu_3(HHTT)_2$ film can facilitate perovskite growth and enable defect passivation on the perovskite surface. The self-assembly approach is suitable for preparing large-area films conformally on a substrate, enabling the application of the film in large-area devices. Encouragingly, an efficiency over 22% is obtained from ideal-bandgap PSCs.

To avoid light absorption of $Cu_3(HHTT)_2$ in the devices, we prepared ultrathin films by a single cycle. The film prepared under the optimum condition, which will be addressed later, has a thickness of ~ 6 nm (**Figure 5.21a and 5.21b**). The optical transmission spectra of glass/ITO/$Cu_3(HHTT)_2$ and glass/ITO/NiO_x substrates are shown in **Figure 5.22**, which demonstrate similar transmittance in the visible region. The AFM image of a $Cu_3(HHTT)_2$ film grown on a SiO_2/Si substrate reveals that the film is continuous and has a surface roughness of 0.28 nm, which is even lower than the layer distance (0.32 nm) (**Figure 5.21c**).

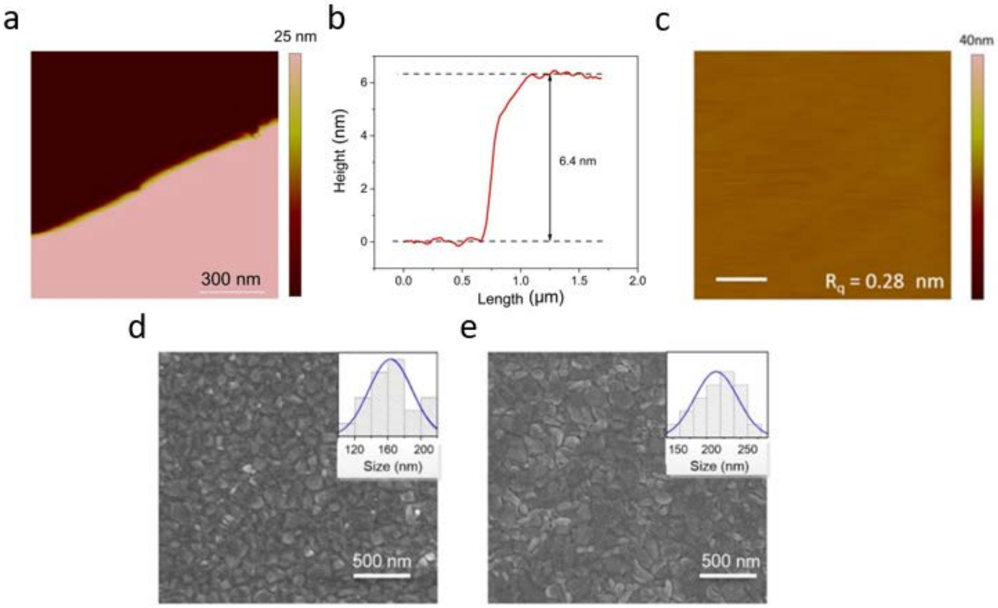

Figure 5.21. (a) AFM image of the edge of MOF on SiO_2. (b) AFM height profile of MOF. (c) AFM image of a $Cu_3(HHTT)_2$ thin film on an SiO_2/Si substrate with a roughness of 0.28 nm. Scale bar is 300 nm. SEM images of perovskite films on (d) NiO_x and (e) $Cu_3(HHTT)_2$.

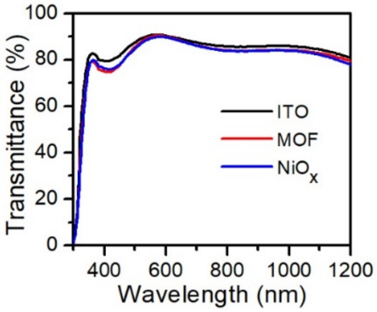

Figure 5.22. Transmittance spectra of ITO, MOF/ITO and NiO_x/ITO films.

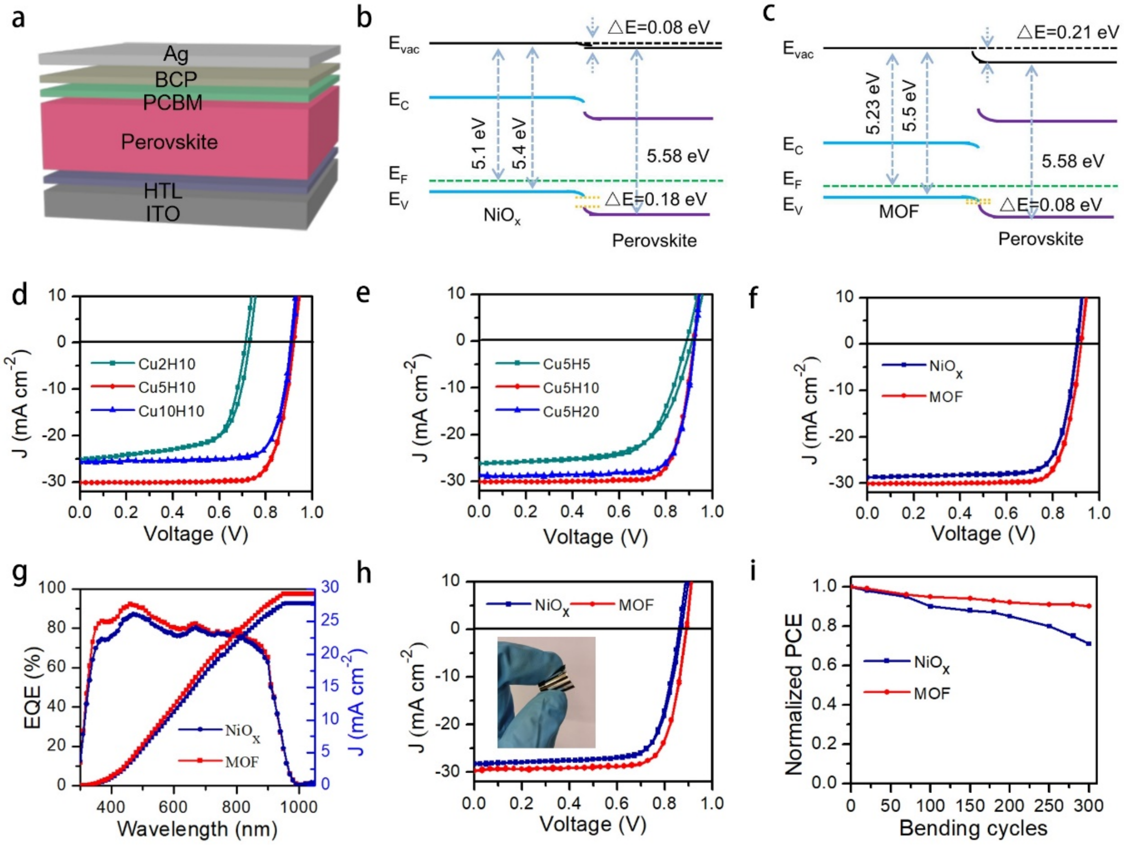

Figure 5.23. (a) Device structure of an inverted PSC. Band bending at (b) NiO_x/perovskite interface and (c) MOF/perovskite interface. *J-V* curves of PSCs based 2D c-MOF HTL with different (d) metal ions and (e) ligand molecules dipping periods. Labels: Cu*x*H*y*: *x* min for Cu and *y* min for HHTT dipping. (f) *J-V* curves of PSCs based on NiO_x and 2D c-MOF as HTLs. (g) EQE spectra of PSCs based on different HTLs. (h) *J-V* curves of flexible PSCs based on different HTLs. Inset: photo of a flexible PSCs. (i) Bending stability of flexible PSCs under a bending radius of 5 mm.

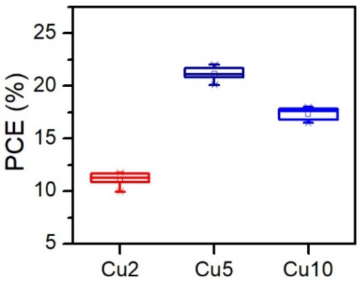

Figure 5.24. Statistics of PCE distribution of PSCs with different dipping period of metal ions.

After $Cu_3(HHTT)_2$ films were grown on ITO substrates, $FA_{0.83}Cs_{0.17}Sn_{0.35}Pb_{0.65}I_{2.9}Br_{0.1}$ perovskite films were prepared on the top by an antisolvent method[80b, 135]. The perovskite active layer has an optimized thickness. If the film is too thick, most photo-carriers are recombined before arriving to respective electrodes; if the film is too thin, light harvesting is not at optimum. In addition, perovskite films (control samples) were also prepared on glass/ITO/NiO_x substrates under the same processing conditions. The perovskite films were characterized under SEM, as shown in **Figure 5.21a and b**. It is interesting to find that the perovskite film grown on a $Cu_3(HHTT)_2$ film shows larger grains and fewer grain boundaries than the control sample, implying a better crystallinity of the perovskite films on the $Cu_3(HHTT)_2$ surface.

Table 5.5. The photovoltaic parameters of the *J-V* measurements from Figure 5.23d.

HHTT 10	Bias	V_{OC} (V)	J_{SC} (mA cm^{-2})	FF (%)	PCE (%)
Cu 2	Reverse	0.71	25.17	64.24	11.48
	Forward	0.73	25.17	66.18	12.16
Cu 5	Reverse	0.92	30.13	79.15	21.89
	Forward	0.92	30.13	79.42	22.01
Cu 10	Reverse	0.91	25.71	77.16	18.05
	Forward	0.90	25.71	77.05	17.83

Table 5.6. Summary of parameters of ideal-bandgap Pb-Sn mixed PSCs.

Perovskite	MA free	E_g (eV)	V_{OC} (V)	J_{SC} (mA cm^{-2})	FF (%)	PCE (%)
$MAPb_{0.7}Sn_{0.3}I_3$	No	1.38	0.85	25.3	71.7	15.42[135]
$Cs_{0.3}FA_{0.7}Sb_{0.3}Pb_{0.7}I_3$	Yes	1.34	0.804	29.4	81.8	19.3[136]
$MAPb_{0.5}Sn_{0.5}I_{2.4}Br_{0.6}$	No	1.35	0.89	25.67	75	17.13[137]
$Cs_{0.17}FA_{0.83}Pb_{0.7}Sn_{0.3}I_3$	Yes	1.33	0.8	28.7	73.5	17.6[138]
$FA_{0.8}MA_{0.2}Pb_{0.8}Sn_{0.2}I_3$	No	1.33	0.899	30.88	81.17	22.51[139]
This work	Yes	1.33	0.92	30.13	79.42	22.01

We optimized the MOF film thickness by adjusting the dipping periods in the solutions of metal ions and ligand molecules. Performance of 15 devices under each condition were measured and statistical data was extracted. First, we kept the dipping period for ligand molecules at 10 min and changed the dipping period for Cu ions to be 2, 5 and 10 min. **Figure 5.23** shows the *J-V* characteristics of the devices with different dipping periods of metal ions and the photovoltaic parameters are summarized in **Table 5.5**. The statistical data of the photovoltaic parameters with different dipping periods of metal ions are shown in **Figure 5.24**. Notably, the device performance is dramatically influenced by the dipping period for metal ions. For the device with 2 min dipping, a low PCE of 12.16% is obtained with V_{OC} of 0.73 V, J_{SC} of 25.17 mA cm^{-2} and FF of 66.18%, which can be ascribed to the poor coverage of $Cu_3(HHTT)_2$ on the ITO substrate. As the dipping period of metal ions is increased to 5 min, the device shows high efficiency of 22.01% together with V_{OC} of 0.92 V, J_{SC} of 30.13 mA cm^{-2} and FF of 79.42%, which is one of the highest values among ideal-bandgap PSCs (**Table 5.6**). However, when the dipping period is 10 min, the efficiency decreases to 18.05% with V_{OC} of 0.91 V, J_{SC} of 25.71 mA cm^{-2} and FF of 77.16%.

Table 5.7. The photovoltaic parameters of the *J-V* measurements from **Figure 5.23e**.

Cu 5		V_{OC} (V)	J_{SC} (mA cm^{-2})	FF (%)	PCE (%)
HHTT 5	Reverse	0.89	26.27	66.60	15.57
	Forward	0.90	26.27	67.72	16.01
HHTT 10	Reverse	0.92	30.13	79.15	21.89
	Forward	0.92	30.13	79.42	22.01
HHTT 20	Reverse	0.92	28.67	78.88	20.81
	Forward	0.92	28.67	78.15	20.60

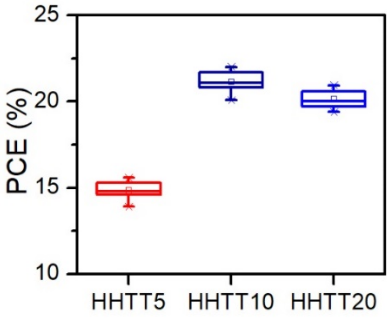

Figure 5.25. Statistics of PCE distribution of PSCs with different dipping period of ligand molecules.

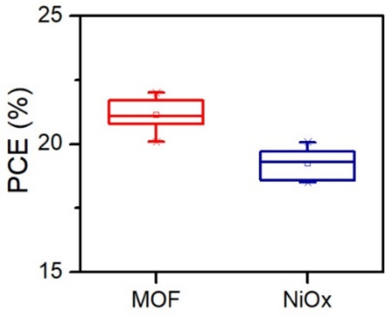

Figure 5.26. Statistics of PCE distribution of PSCs based on different HTLs.

Then, we optimized the device performance by keeping the dipping period for metal ions at 5 min and changing the dipping period for ligand molecules to be 5, 10 and 20 min. As shown in **Figure 5.23e**, the champion device is obtained when the dipping period is 10 min. The photovoltaic parameters with different dipping periods of ligand molecules are summarized in **Table 5.7** and the statistical data of the photovoltaic parameters are shown in **Figure 5.25**. Hence, the optimum conditions for preparing the $Cu_3(HHTT)_2$ film are 5min and 10 min for metal and organic ligand dipping, respectively, leading to an ultrathin film of ~6 nm thickness (**Figure 5.21a and 5.21b**). We also prepared PSCs based on NiO_x HTL as a control. As shown in **Figure 5.23f**, the control device exhibits a moderate PCE of 20.17% with V_{OC} of 0.90 V, J_{SC} of 28.73 mA cm^{-2} and FF of 78.03%. The corresponding statistical photovoltaic parameters are shown in **Figure 5.26**. The external quantum efficiency (EQE) of the champion devices based on different HTLs and integrated J_{SC} are shown in **Figure 5.23g**, which agree well with the values from the *J*-*V* curves.

To find the interface property between $Cu_3(HHTT)_2$ and perovskite layers, density-functional theory (DFT) calculations are conducted. To simplify the calculation while remaining the generality, a cell of $MAPb_{0.5}Sn_{0.5}I_3$ perovskite with PbI_2/SnI_2 surface is constructed. It is reported that defects involving Pb, Sn and I are critical to the band structure since band edges of such perovskites are dominated by their orbitals[140]. Specifically, antisite defects related to those ions are detrimental to carrier lifetime since they can lead to deep traps that may act as carrier recombination centers[141]. It is reported that C-N group in organic molecules can effectively passivate antisite defects in mixed perovskite by bonding with Sn^{2+}.[142] We therefore suspect that the C-N component in $\mathrm{Cu_3(HHTT)_2}$ possesses similar functions. **Figure 5.27a-d** shows the perovskite supercells with $\mathrm{Sn_I}$ and $\mathrm{Pb_I}$ antisite defects passivated with $\mathrm{Cu_3(HHTT)_2}$, respectively. To verify the nature of these defect states before and after passivation, density of states (DOS) of perfect supercells and defective supercells with and without the coverage of $\mathrm{Cu_3(HHTT)_2}$ are simulated (**Figure 5.28**). As depicted in **Figure 5.27e and f**, mid-gap trap states can be induced by antisite defects while the traps move to the valence band edge after $\mathrm{Cu_3(HHTT)_2}$ coating. Therefore, $\mathrm{Cu_3(HHTT)_2}$ can effectively passivate the deep antisite defects and lead to low defect density at the HTL/perovskite interface, which is consistent with our experimental results.

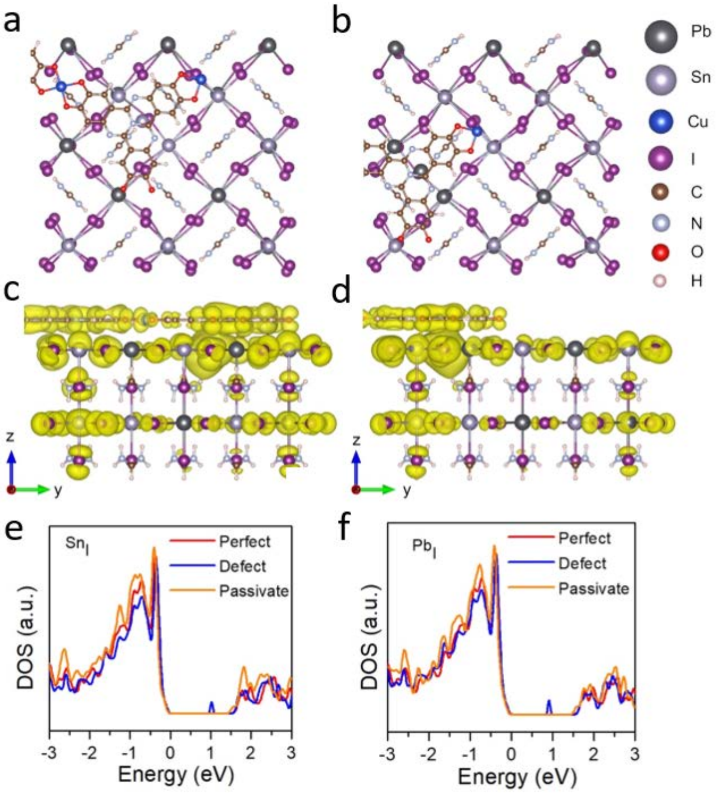

Figure 5.27. Perovskite supercells with (a,c) $\mathrm{Sn_I}$ and (b,d) $\mathrm{Pb_I}$ antisite defects passivated with MOF. DOS of (e) $\mathrm{Sn_I}$ and (f) $\mathrm{Pb_I}$ antisite defect surfaces.

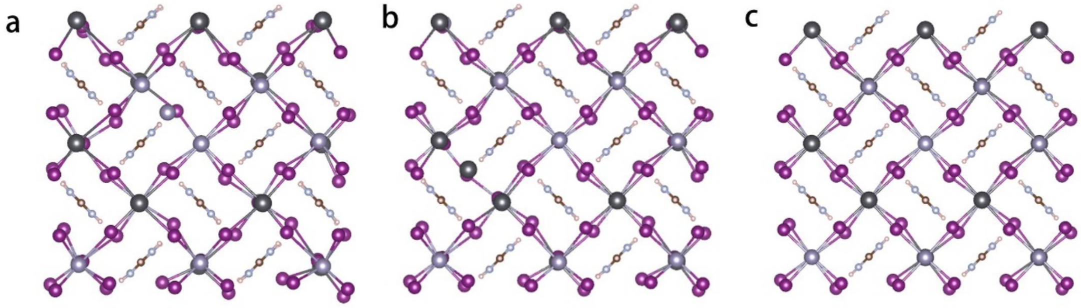

Figure 5.28. (a) Perovskite with Sn_I defect. (b) Perovskite with Pb_I defect. (c) Perovskite without defect.

5.3 Conclusion

In summary, large-area $Cu_3(HHTT)_2$ 2D c-MOF thin films with high orientation and uniformity are successfully prepared by using a facile layer-by-layer assembly method under ambient condition. The carrier transport in the $Cu_3(HHTT)_2$ thin films can be attributed to a phonon-assisted hopping process of carriers between localized states. PDs based on $Cu_3(HHTT)_2$ thin films show reliable photo response in a broad range from UV to MIR (370-3400 nm), which significantly outperform other solution-processed broadband PDs reported before. Such PDs with detectable regions to mid-infrared may find broad applications for thermal and medical imaging, air pollutant and dangerous chemical monitoring. Thanks to the intrinsic flexibility of the material, flexible PDs are fabricated on plastic substrates with excellent mechanical stability. Optical synapse based on the $Cu_3(HHTT)_2$ film is realized, which can achieve superior data recognition accuracy in ANN. Moreover, perovskite solar cell using the film as HTL has significantly improved performance when compared to traditional HTL, which is mainly due to the enhanced crystallinity of perovskite and the defect passivation effect of $Cu_3(HHTT)_2$ film on perovskite layer. This work demonstrates the potential of $Cu_3(HHTT)_2$ thin films for high-performance and multi-functional optoelectronic devices.

5.4 Experimental Section

5.4.1 Materials

All chemical reagents, solvents, and 4,5-dimethoxy-2-nitrobenzaldehyde for synthesizing HHTT were purchased from Dieckmann chemical company, China. Copper acetate was purchased from Sigma-Aldrich Co.

Formamidinium iodide (99.99%) (FAI) was purchased from Dyesol. Lead iodide (99.99%) (PbI2), cesium iodide (99.99%) (CsI) and lead bromide (99.99%) (PbBr2) were purchased from Alpha Aesar. DMF (99.8%), DMSO (99.9%) and diethyl ether (99.9%) were purchased from Sigma-Aldrich, Inc. Phenyl-C71-butyric acid methyl ester (99%) (PCBM) was purchased from Nano-C.

5.4.2 Synthesis procedure of HHTT ligand

The powder of HHTT ligand was obtained through a multi-step synthetic scheme, which is illustrated in **Figure 5.29**. The reactions were performed with the standard vacuum-line and Schleck techniques under nitrogen. Colum chromatography was performed using the silica gel. The procedure started by synthesizing 5,6-Dimethoxyanthranil **(2)**: Tin powder (13 g, 110 mmol) was added in portions to a stirred solution of 4,5-dimethoxy-2-nitrobenzaldehyde **(1)** (5 g, 23.7 mmol) in glacial acetic acid (300 mL). The resulting mixture was stirred at room temperature for 20 h before being worked up with ether and water. The organic layer was dried over anhydrous sodium sulfate and concentrated under vacuum. The residue was purified by silica gel column chromatography eluted with 8:2 hexanes/ethyl acetate followed by recrystallization using hexanes/ethyl acetate, affording 1.84 g (44%) of 5,6-dimethyoxyanthranil **(2)** as white rod-like crystals. ^{1}H NMR (400 MHz, $CDCl_3$): δ = 8.81 (1H), 6.78 (1H), 6.64 (1H), 3.96 (3H), 3.90 (3H) ppm. Next, 2,3,7,8,12,13-Hexamethoxytricycloquinazoline **(3)** was synthesized: A mixture of sulfolane (100 mL) and glacial acetic acid (25 mL) was added ammonium acetate (12 g, 156 mmol) and 5,6-dimethyoxyanthranil **2** (4 g, 22.33 mmol). The reaction mixture was refluxed for 96 hours and cooled down to room temperature, after which water was added. The resulting greenish-yellow solid was collected by suction filtration, washed with water and methanol, and dried under air to give 789 mg (20% yield) of 2,3,7,8,12,13- hexamethoxytricycloquinazoline **3**. ^{1}H NMR (400 MHz, $CDCl_3$): δ = 7.67 (3H), 6.88 (3H), 4.03 (9H), 4.00 (9H) ppm. Finally, 2,3,7,8,12,13-Hexahydroxytricycloquinazoline (HHTT) **(4)** was obtained through the following process: A mixture of 2,3,7,8,12,13-hexamethoxytricycloquinazoline **3** (800 mg, 1.6 mmol) and pyridine hydrochloride (27 g, 234 mmol) was heated to 240 °C for 3 hours and then cooled down to room temperature. Water was then added to the mixture, and the resultant black precipitate was collected by suction filtration, washed with water, and dried under vacuum to yield 328 mg (50%) of 2,3,7,8,12,13 hexamethoxytricycloquinazoline **4**. ^{1}H NMR (400 MHz, MeOD): δ = 7.48 (3H), 6.67 (3H) ppm. ^{13}C NMR (100 MHz, DMSO-*d6*): δ = 145.78, 143.92, 139.79, 111.05, 109.63 ppm. MALDI-TOF m/z, $[M]^+$, **4**: $C_{21}H_{12}N_4O_6$, calculated: 416.08, found: 416.96

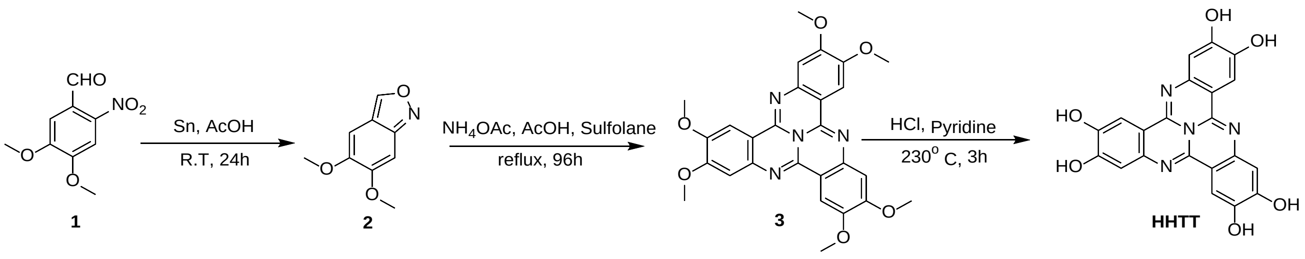

Figure 5.29. Synthetic route of HHTT **(4)**.

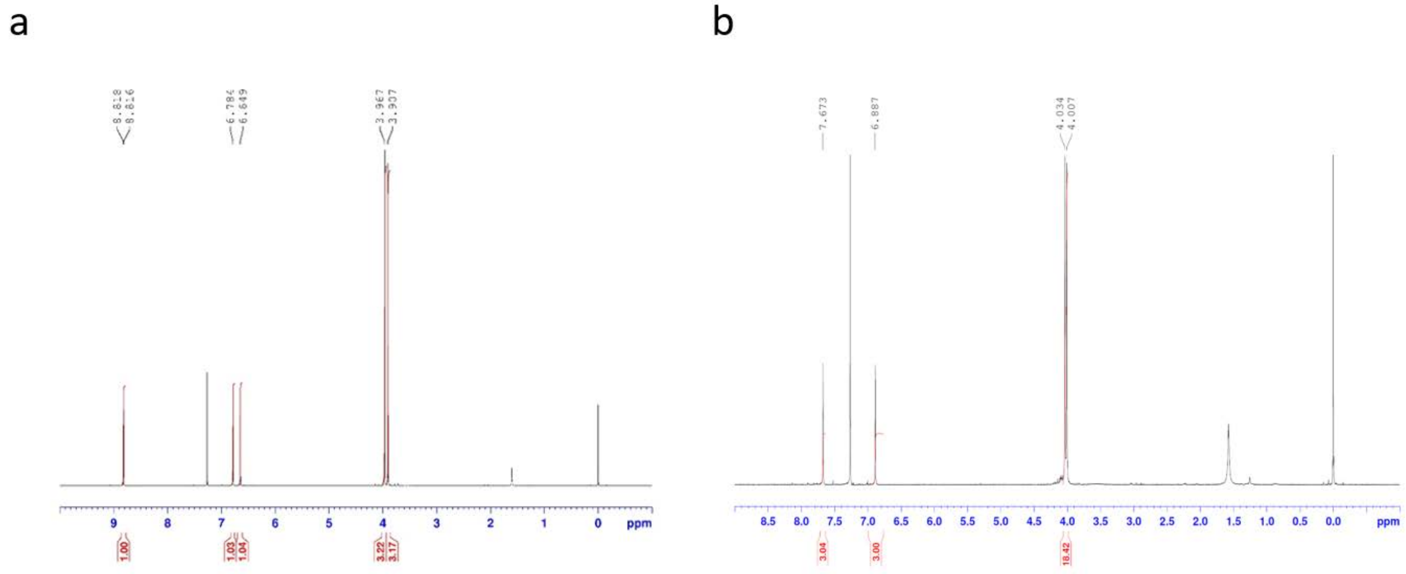

Figure 5.30. ^{1}H NMR of (a) compound **2** and (b) compound **3** in **Figure 5.29**.

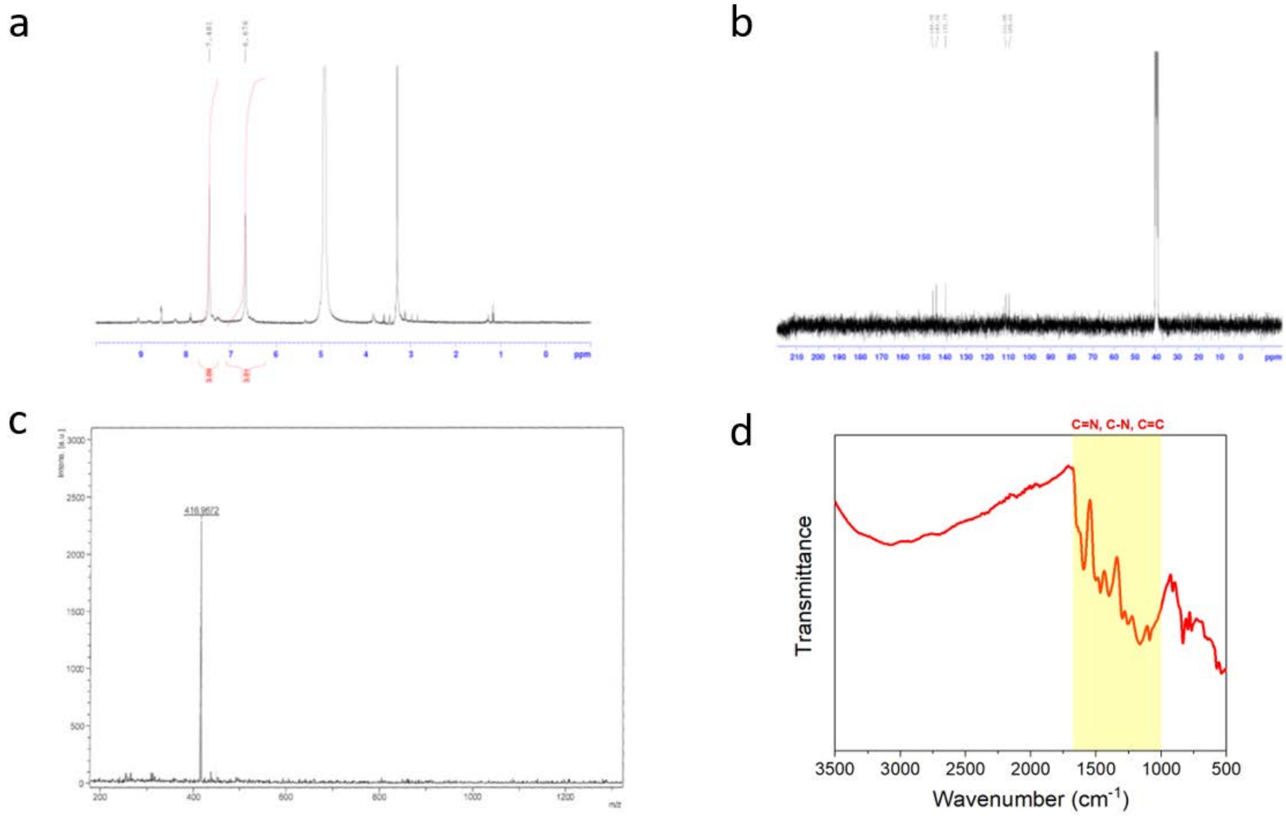

Figure 5.31. Characterizations of HHTT. (a) ^{1}H NMR and (b) ^{13}C NMR spectra of HHTT. (c) MALDI-TOF spectrum of HHTT. (d) FTIR spectrum of HHTT.

5.4.3 Materials Characterization

HHTT: ^{1}H NMR and ^{13}C NMR spectra were recorded on Bruker AC 300 P using the deuterated solvents ($CDCl_3$, and DMSO-d6) with the tetramethylsilane as the internal reference. High-resolution MALDI-TOF mass spectra were obtained with a Bruker Autoflex MALDI-TOF mass spectrometer. Fourier transform infrared spectroscopy (FTIR) was performed on a Spectrum 100 (Perkin Elmer, Inc., USA) spectrometer with a scan range of 4000-400 cm^{-1}.

$Cu_3(HHTT)_2$ thin film: The out-of-plane and in-plane XRD spectra was obtained by X-Ray diffraction (XRD), Rigaku SmartLab X-Ray diffractometer. SEM images were observed under a field emission scanning electron microscope (FESEM) (Tescan MAIA3). AFM images were recorded using scanning probe microscope (Bruker NanoScope 8). The thicknesses of the MOF films were characterized by a surface profiler (Bruker DektakXT). The HRTEM image was taken using a field emission electron microscope (JEM-2100F). The absorption spectra were recorded with a LAMBDA 1050+ UV/Vis/NIR spectrophotometer (PerkinElmer). UPS spectra was recorded using a X-Ray Photoelectron Spectrometer System (Thermo Fisher Nexsa).

5.4.4 Device Fabrication

Pre-patterned substrate preparation: 300nm-SiO_2/Si and PI substrates were cleaned by ultrasonication bath using deionized water, acetone, and IPA, followed by drying the substrate with stream of nitrogen gas. Next, 10nm-Cr/100nm-Au electrodes were deposited by sputtering after the desired area was patterned by standard photolithography process. The channel length and width of the devices used in this work are 5 and 800 μm, respectively. The substrates with electrodes were then replaced in glovebox for later use.

Fabrication of $Cu_3(HHTT)_2$ thin film for PDs and optical synapse: The above patterned substrates were first functionalized using oxygen plasma for 30 minutes. Next, the substrates were used for preparing $Cu_3(HHTT)_2$ according to previous report.[42] The functionalized substrates were immersed alternatively into copper acetate and HHTT with various concentration for 20 minutes and 40 minutes (**Figure 5.1b**). Ethanol, IPA and DMF were employed as solvents for both precursors. Devices fabricated by ethanolic solutions were used for most of the measurement. The substrates were washed with corresponding solvents to remove excessive precursor between each immersion step. The film thickness can be controlled by cycle numbers. The process is stopped after desired thickness is achieved, and the substrate is stored in a N_2-filled glove box.

Fabrication of Perovskite Solar Cells: ITO glass substrates were ultrasonically cleaned by deionized (DI) water, acetone and isopropanol for 15 min, respectively. $Cu_3(HHTT)_2$ thin films are then synthesis through the above method but with immersion times mentioned in Section 5.2.6. For controlled devices, the process of preparing NiO_x on ITO was similar to the previous report. NiO_x dissolved in DI water (7.5 mg mL^{-1}) was spin-coated on the ITO substrate at 4000 rpm for 30 s in ambient air and then the films were annealed at 150 ℃ for 30 min in air. Then the films were transferred to N_2 glovebox. The Pb-Sn mixed perovskite precursor was prepared by dissolving FAI (0.83 mmol), SnI_2 (0.35mmol), SnF_2 (0.035mmol), CsI (0.17 mmol), $PbBr_2$ (0.05 mmol), PbI_2 (0.6 mmol) in mixed solvent (DMF:DMSO=4:1). 4-hydrazinobenzoic acid (HBA) was introduced to suppress the oxidation of Sn^{2+}, and the molar ratio between HBA and SnI_2 was 3%. The perovskite precursor solution was spin-coated on the substrate at 1000 rpm for 10 s and 5000 rpm for 20 s, and diethyl ether was dropped on the film at 10th s. Then, the perovskite films were annealed at 70 ºC for 1 min and 100 ºC for 10 min. Afterward, PCBM (20 mg mL^{-1}) and BCP (0.5 mg mL^{-1}) were spin-coated on the films. Finally, 100 nm silver electrodes were thermally evaporated onto the films. The electrode size is 0.048 cm^2 unless stated otherwise.

5.4.5 Estimation of grain size and mircostrain based on XRD data

The grain size and macrostrain of the $Cu_3(HHTT)_2$ are estimated according to UDM of W-H method, which assumes uniform strain in all crystilline directions and is used extensively for polycrystaline materials.[143] In this model, the peak broadening or full width at half maximum (FWHM) for each XRD peak can be expressed as:[143]

$$\beta_{hkl} = \left(\frac{k\lambda}{D cos\theta}\right) + 4\varepsilon tan\theta,$$

where k, D and ε are shape factor, crystal size and microstrain. Rearranging the equation yields the following:

$$\beta_{hkl}cos\theta = \frac{k\lambda}{D} + 4\varepsilon sin\theta.$$

A W-H plot is obtained by ploting $\beta_{hkl}cos\theta$ against $4sin\theta$ (Figure S6b). The value of k is assigned to be 0.94, which is a general value originally derived by Scherrer and used widely for thin films.[144] From linear fitting of the data, crystal size and microstrain can be estimated from the y-intercept and the slope.

5.4.6 Device Measurements

Temperature and frequency dependent conductivity measurements: The temperature dependent measurements were conducted using a cryogenic probe station (Lake Shore Cryotronics). The AC measurement was performed by connecting a probe station in glove box to an electrochemical workstation (VersaSTAT 3, Ametek).

Electrical and optoelectronic measurements for the devices: A Keithley 4200 semiconductor parameter analyzer was employed for electrical and optoelectrical measurements for the devices. The devices were placed in a glovebox filled with N_2 gas equipped with various LED light sources. LED with wavelengths of 370, 685, 850, 980, 1100, 1300, 1450, 1550, 2000, 2800 and 3400 nm were used in this work. The intensity was tuned to about 200 $\mu W/cm^2$ when measuring spectral response. *J-V* curves were measured by a Keithley 2400 source meter with a solar simulator under AM 1.5 G one sun illumination (Newport 66902). The EQE of the PSCs was obtained from an EQE system under DC mode. UV-vis spectra were collected on a UV-vis spectrometer (Perkin elmer).

Bending stability assessment for flexible device: Device performance of the flexible devices was measured with the above equipment first. Then, the whole PI sheet with devices were curved against a little glass bottle with radius of 8 mm for different times. After specific times of bending, device measurement was performed.

5.4.7 Computational Methods

DFT simulation for Young's modulus of $Cu_3(HHTT)_2$: All DFT calculations were performed using Quantum Expresso (ver. 6.5).[145] The initial lattice parameters of $Cu_3(HHTT)_2$ unit cell were obtained from previous literature.[94] Perdew, Burke and Ernzerhof (PBE) exchange-correlation functionals[146] under an electronic convergence criterion of 1×10^{-6} eV were used to fully relax the structure. Projector augmented wave (PAW) method with a plane wave basis set of 500 eV cut-off energy were applied. A k-grid of 4 x 4 x 4 was used. During Young's modulus calculation, different amount of uniaxial strain along a-axis was applied to the unit cell of $Cu_3(HHTT)_2$. The cells are fully relaxed at each calculated strain points.

DFT Simulation for interface property of perovksite/$Cu_3(HHTT)_2$: Quantum ESPRESSO software was used to perform all the DFT simulations. Before the simulation, we will construct and visualize the initial crystal structure using VESTA software. The initial atomic positions will be obtained by either referencing to existing literatures or estimated from independent bond lengths. Prior to the density of states (DOS) simulations, all the structures were relaxed under PBE exchange-correlation functions with an electronic convergence criterion of 1×10^{-6} eV. In the simulation, PAW method with a plane wave basis set of 450 eV cut-off energy was used.

Calculation of Young's modulus: Figure 5.18 shows the energy difference of a unit cell as a function of applied strain along **a** and **b**-axis (they are symmetric). Then, Y can be extracted using the following equation:

$$Y = \frac{1}{A_0}\frac{\partial^2 E_s}{\partial \varepsilon^2},$$

where A_0 is equilibrium surface area of the unit cell and $\frac{\partial^2 E_s}{\partial \varepsilon^2}$ is the second partial derivative of strain energy with respective to applied strain.

Neural network simulation: CrossSim[147] was used to simulate the device performance when implemented in a crossbar array.[148] During the simulation, the artificial synapse-based crossbar array is responsible for two crucial operations: a vector matrix multiply and parallel rank 1 outer product update. For the simulation with a Sandia file classification dataset and the "Optical Recognition of Handwritten Digits" dataset, a 256 × 512 × 9 and a 64 × 36 × 10 sized network were adopted respectively. The measured LTP and LTD characteristics of $Cu_3(HHTT)_2$ synapse were mapped to the numerical synaptic weights, and the non-linearity and write noise of the device were incorporated into the simulation through weight updating.[134b] Specifically, only weights corresponding to high ΔPSC levels are considered so that the influence of device nonlinearity and asymmetry on recognition accuracy can be minimized.

5.4.8 Statistical Analysis

The statistical data has not gone thought any pre-processing. The error bars in the graphs represent mean values and standard deviations of the data. As mentioned in the main manuscript, the sample sizes are 4 for PDs and 15 for solar cells in all statistical analysis. Statistical method: standard deviation was calculated to assess significant differences, which was processed in Excel.

Chapter 6: 2D Metal–Organic Framework $Cu_3(HHHAT)_2$ Films for Broadband Photodetector and Ferroelectric Memory

$Cu_3(HHHAT)_2$ is a novel 2D MOF material which shows excellent physical and chemical properties. With the high conductivity and probability for thin film fabrication, it also has tremendous potential in optoelectronic applications. Herein, we demonstrated for the first time the high quality $Cu_3(HHHAT)_2$ thin films. With detailed materials characterizations, including GIXRD, SEM and AFM, indicate that the thin film is in high-quality with preferred orientation. Moreover, PDs with reliable broadband photo-response have been fabricated. More importantly, a top-gated transistor with resistive memory effect has been demonstrated for the first time in 2D c-MOF devices. The results clearly demonstrate the potential of using 2D c-MOFs for high-performance optoelectronic applications.

6.1. Introduction

MOF is a type of porous materials which have a series of unique physical and chemical properties.[95c] They are organic networks interconnected by metal nodes. Due to the large specific surface area, tunable porosity, dense active sites and unlimited chemical tailorability, they have long been employed as functional materials for a series of applications, such as catalysis[23, 44, 95], gas sensor[24, 95b, 96], energy storage[23, 25, 97] and molecular filter[149]. Over the past decade, impressive progress has been indeed obtained in those traditional areas. However, optoelectronic applications using MOFs remains blank until recently due to their low electrical conductivity.[4] Lately, researchers have developed 2D c-MOFs, which exhibit 2D network structure and has exceptional conductivity with moderate band gap due to their strong in-plane conjugation and tight inter-layer stacking.[5, 45]

On the other hand, conventional PD functional materials such as Si and III-V semiconductors fail to provide desired functionalities like lost cost, stretchable and wearable optoelectronics.[71b, 150] Therefore, much research effort has been put in developing next-generation materials for advanced optoelectronic applications. For instance, OIHPs show excellent optical absorption coefficient, outstanding mobility and exceptional defect tolerance.[29] However, they are extremely unstable in ambient conditions.[151] 2D materials have superior transport and optoelectronic properties, but the effective large-area fabrication is still lacking.[152] Therefore, the search of novel optoelectronic materials still needs to continue. Considering the moderate band gap, high electrical conductivity, solution-processibility, air stability and intrinsic flexibility of 2D c-MOFs, it can be a potential candidate for next-generation PD functional materials. Despite their potential, only very few research have been done in this area. Arora et al. first reported a PD based on 2D $Fe_3(THT)_2(NH_4)_3$ at show a detectivity of 7×10^8 Jones at 77K.[46] Our group recently developed a flexible ultra-broadband PD based on $Cu_3(HHTT)_2$ with response from UV to MIR. We fabricated wafer-scale $Cu_3(HHTT)_2$ thin film for the first time and studied its carrier transport behaviour carefully.[45] The device also shows typical synaptic behaviours and excellent data recognition efficiency in ANN. Lately, another novel 2D c-MOF, $Cu_3(HHHAT)_2$ is developed in powder form for electrocatalytic reduction of CO_2 to methane.[153] $Cu_3(HHHAT)_2$ shows excellent thermal and chemical stability as well as desirable π-π interactions, which shows potential for optoelectronic applications if thin film form of this material can be developed.

Herein, we firstly report the fabrication of $Cu_3(HHHAT)_2$ thin film. By various materials characterizations, it is confirmed that the film is in high quality. Broadband PDs with response from UV to NIR are developed based on the $Cu_3(HHHAT)_2$ thin film, showing reliable photo-response. More importantly, ferroelectric resistive memory effect is for the first time demonstrated for 2D c-MOF devices based on a top-gated device structure with a ferroelectric organic dielectric layer. This work demonstrates the potential of using novel 2D c-MOF thin film for (opto)electronic devices.

6.2 Results and Discussion

6.2.1 Materials and Thin film Characterizations

Figure 6.1 shows the synthetic scheme for the HHHAT powder. **Figures 6.2 and 6.3** display the NMR spectra for intermediates and the final HHHAT product. The spectra indicate that reaction intermediates and products are pure without any contamination. **Figure 6.4** shows the procedure of the layer-by-layer self-assembling growth of $Cu_3(HHHAT)_2$. The detailed experimental procedure is included in Experimental Section. Briefly, the substrate is first functionalized with hydroxyl groups. Next, the substrate is immersed into ethanolic solution of $Cu(OAc)_2$. The Cu^{2+} ions can be anchored onto the hydroxyl groups. the substrate is then carefully washed with ethanol to avoid excess Cu^{2+} ions. After that, the substrate is immersed into ethanolic solution of HHHAT. The hydroxyl groups in HHHAT will bond with Cu^{2+} ions and form a continuous 2D c-MOF thin layer. After another washing step with ethanol, the process can be repeated until the desired thickness is obtained.

Figure 6.5a displays the FTIR spectra for both HHHAT and $Cu_3(HHHAT)_2$. The broad peak at ~3400 cm^{-1} of HHHAT disappears after the formation of $Cu_3(HHHAT)_2$, indicating the complete reaction is achieved. **Figure 6.5b** reveals the absorption spectrum of $Cu_3(HHHAT)_2$. It is noted that the absorption tail extends to NIR range. **Figure 6.5c** displays the tauc plot obtained from the absorption spectrum, where the band gap is shown to be 1.46 eV, which lies within visible range. The extended absorption range can be attributed to the electronic transition from VBM to mid-gap states or from mid-gap states to CBM. UPS is also employed to study the band structure of $Cu_3(HHHAT)_2$. As indicated in the secondary cut-off region of UPS spectrum (**Figure 6.5d**), the binding energy of $Cu_3(HHHAT)_2$ is 16.13 eV. Under a UV light source of 21.2 eV, the fermi energy can be calculated to be 5.07 eV. On the other hand, the energy difference from fermi level to VBM is 0.68 eV, as revealed in valance band region of UPS spectrum (**Figure 6.5e**). Combing the results from UPS and absorption spectrum, the band structure can be depicted and shown in **Figure 6.5f**.

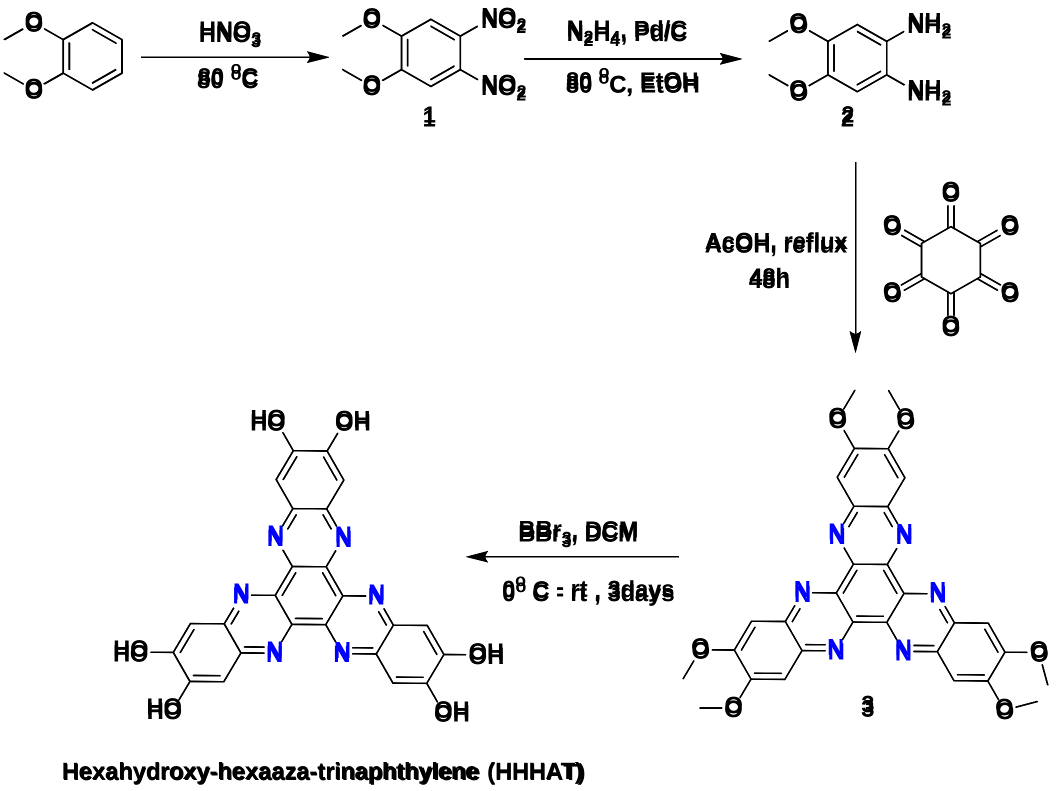

Figure 6.1. Synthetic scheme of HHHAT.

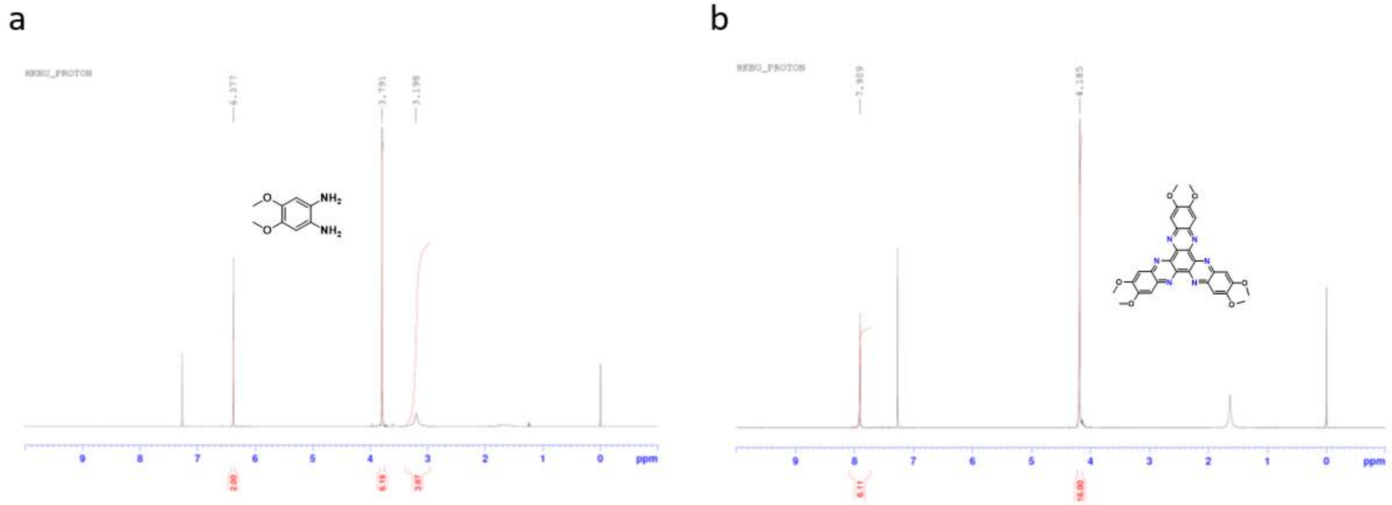

Figure 6.2. (a) ^{1}H NMR of compound 2 recorded in CDCl$_3$. (b) ^{1}H NMR of compound 3 recorded in CDCl$_3$.

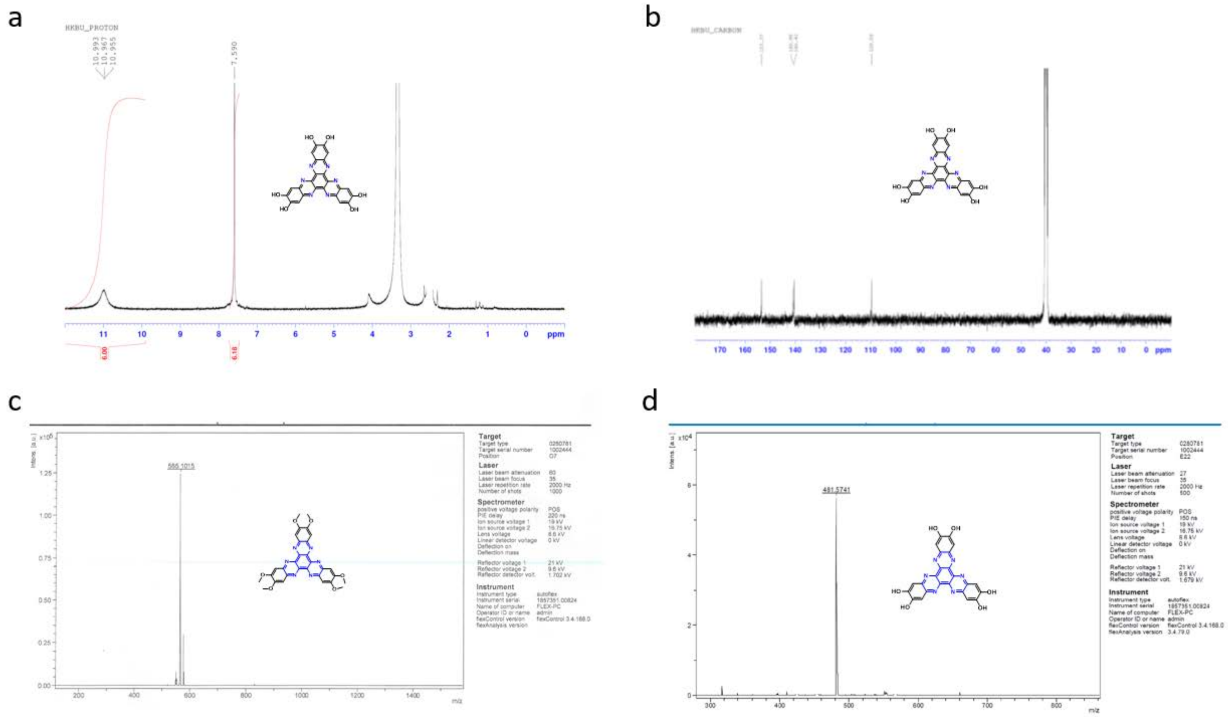

Figure 6.3. (a) ^{1}H NMR of compound HHHAT recorded in DMSO-d$_6$. (b) ^{13}C NMR of compound HHHAT recorded in DMSO-d$_6$. High-resolution MALDI-TOF mass spectra of (c) compound 3 and (d) HHHAT.

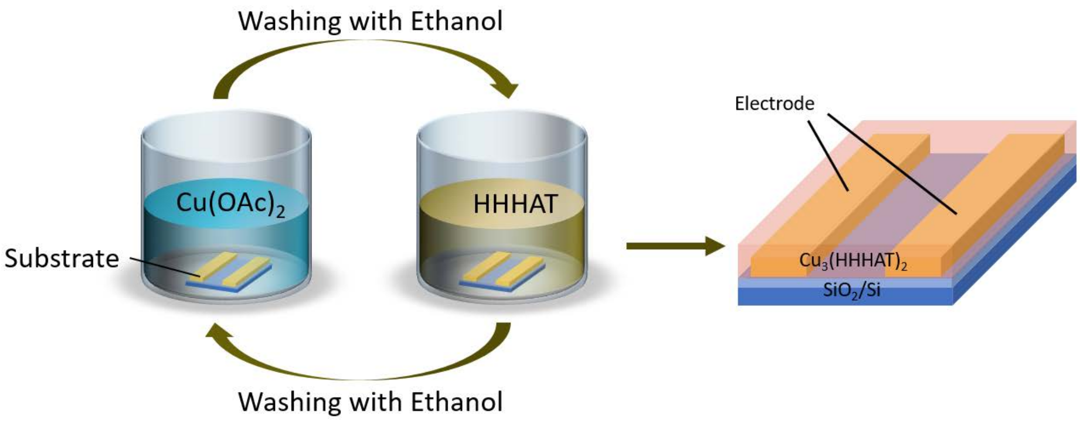

Figure 6.4. Schematic diagram illustrating the fabrication process of Cu$_3$(HHHAT)$_2$ thin film.

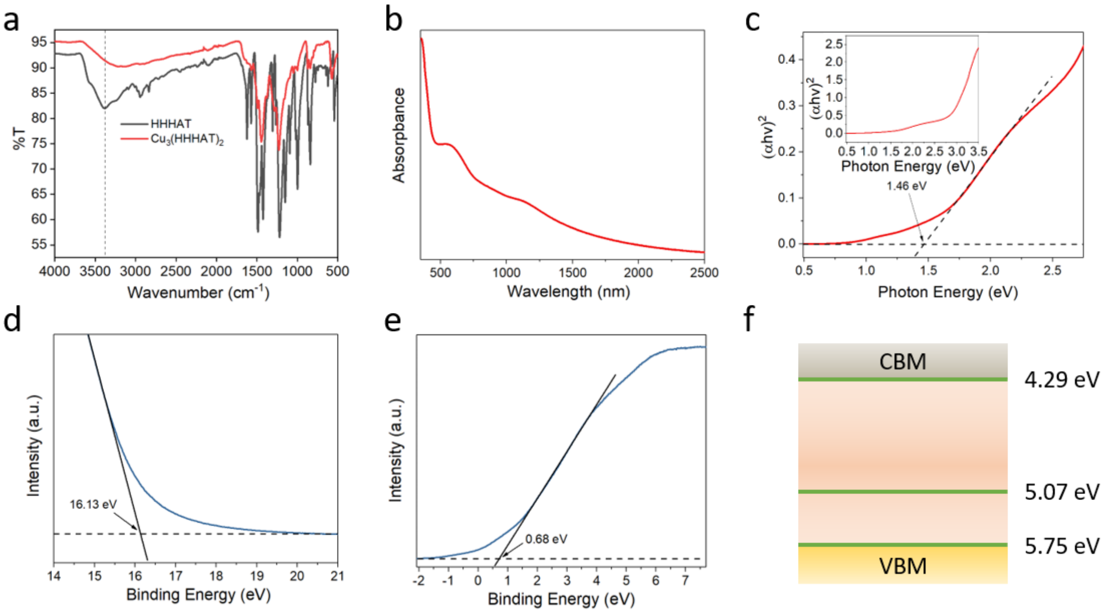

Figure 6.5. (a) FTIR spectra of HHHAT and Cu$_3$(HHHAT)$_2$. (b) Absorption spectrum of Cu$_3$(HHHAT)$_2$. (c) Tauc plot obtained from absorption spectrum of Cu$_3$(HHHAT)$_2$. UPS spectrum in the (b) secondary cut-off region and (c) valence band region of a Cu$_3$(HHHAT)$_2$ film on an ITO substrate.

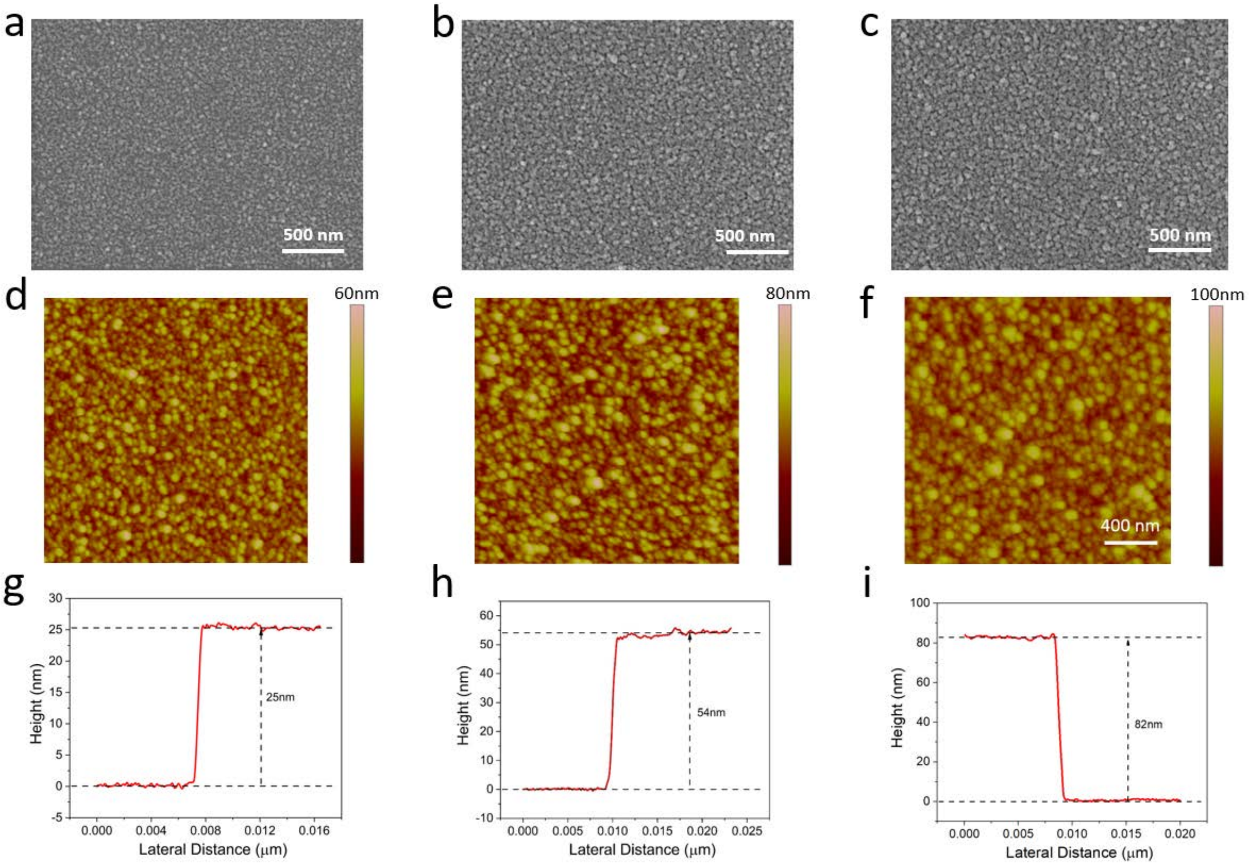

Figure 6.6. SEM images (a-c), AFM images (d-f) and measured thickness (g-i) of $Cu_3(HHHAT)_2$ thin film after 4, 8 and 12 growth cycles.

The thin film morphology is carefully studied by SEM, AFM and GIXRD. As indicated by the SEM image (**Figure 6.6a-c**), the smooth $Cu_3(HHHAT)_2$ film fully covers the substrate without any pinhole, which important for carrier transport. AFM is employed to further confirm the high quality of the thin film. **Figure 6.6d-f** reveals the AFM images of 25, 54 and 82 nm thick (**Figure 6.6g-i**) $Cu_3(HHHAT)_2$ films. The RMS surface roughness are 1.2 nm, 2.6 and 3.9 nm, which are only less than 5% of the total film thickness. Such small surface roughness value further indicates its high quality and its potential for optoelectronic applications.

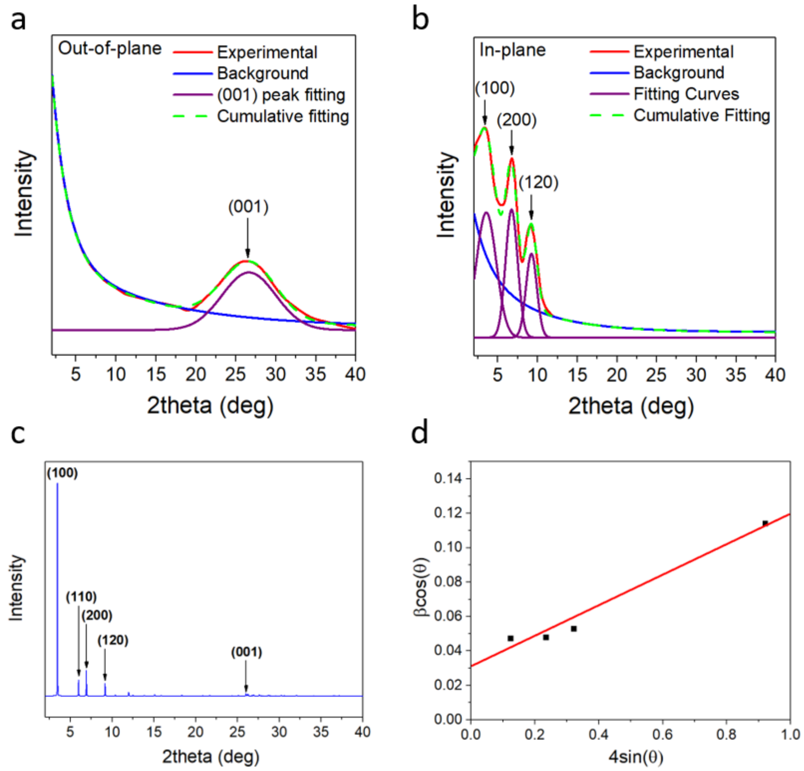

Figure 6.7. (a) Out-of-plane and (b) in-plane GIXRD spectrum of $Cu_3(HHHAT)_2$ film. (c) Simulated PXRD spectrum of $Cu_3(HHHAT)_2$ film. (d) W-H plot corresponding to the GIXRD spectra.

Figure 6.7a and b the out-of-plane and in-plane GIXRD spectra of the $Cu_3(HHHAT)_2$ film. All the measured peaks are in close agreement of the simulated PXRD spectrum. The out-of-plane GIXRD only reveals a peak corresponding to (001) plane, while in-plane GIXRD only reveals peaks corresponding to a-b plane. This clearly indicates that the crystals in the film are well-oriented, further confirms the high quality of the thin film. The relatively broad XRD peaks are due to the small crystal size and such observation has been reported previously for 2D c-MOF thin films.[45, 108, 111] All the XRD peaks can be fitted reasonably well with Gaussian functions.

UDM of W-H method (See Experimental Section and **Figure 6.7d**)[112] can be used to estimate the crystal size and microstrain in the thin film. The calculated crystal size and microstrain for the $Cu_3(HHHAT)_2$ film are 5.7 nm and 6.7%, respectively. The relatively large mircostrain compared to inorganic thin films can be attributed to the large amount of soft organic ligand in the $Cu_3(HHHAT)_2$ film. The values are similar to $Cu_3(HHTT)_2$ we previously reported and is reasonable for 2D c-MOF thin films.

6.2.2 PD performance

PDs based on the $Cu_3(HHHAT)_2$ film is fabricated based on a typical photoconductor. The fabrication details and device geometry can be found in Experimental Section. The dark I-V curves of the devices show that ohmic contact (**Figure 6.8a**), which is desirable for photo-carrier transport. Under light illumination, the photons with sufficient energy incident on $Cu_3(HHHAT)_2$ film excite electrons near VBM and generate electron-hole pairs. When a bias voltage is applied between the electrodes, those photo-carriers will be collected in respective electrodes, contributing to photocurrent. **Figure 6.8b** shows the spectral response of the device. The response spans from UV (370 nmn) to NIR (980 nm), indicating a broadband photo-response. It is worth noting that the spectral response is in highly correspondence with the absorption spectrum (**Figure 6.5b**). The band gap of $Cu_3(HHHAT)_2$ is measured to be 1.46 eV which corresponds to a wavelength of 850 nm. The extended photo-response from 850 nm to 1450 nm can be attributed to carriers excited from the mid-gap states to the conduction band or tail states. The similar effect is found for $Cu_3(HHTT)_2$ film and other polycrystalline materials.

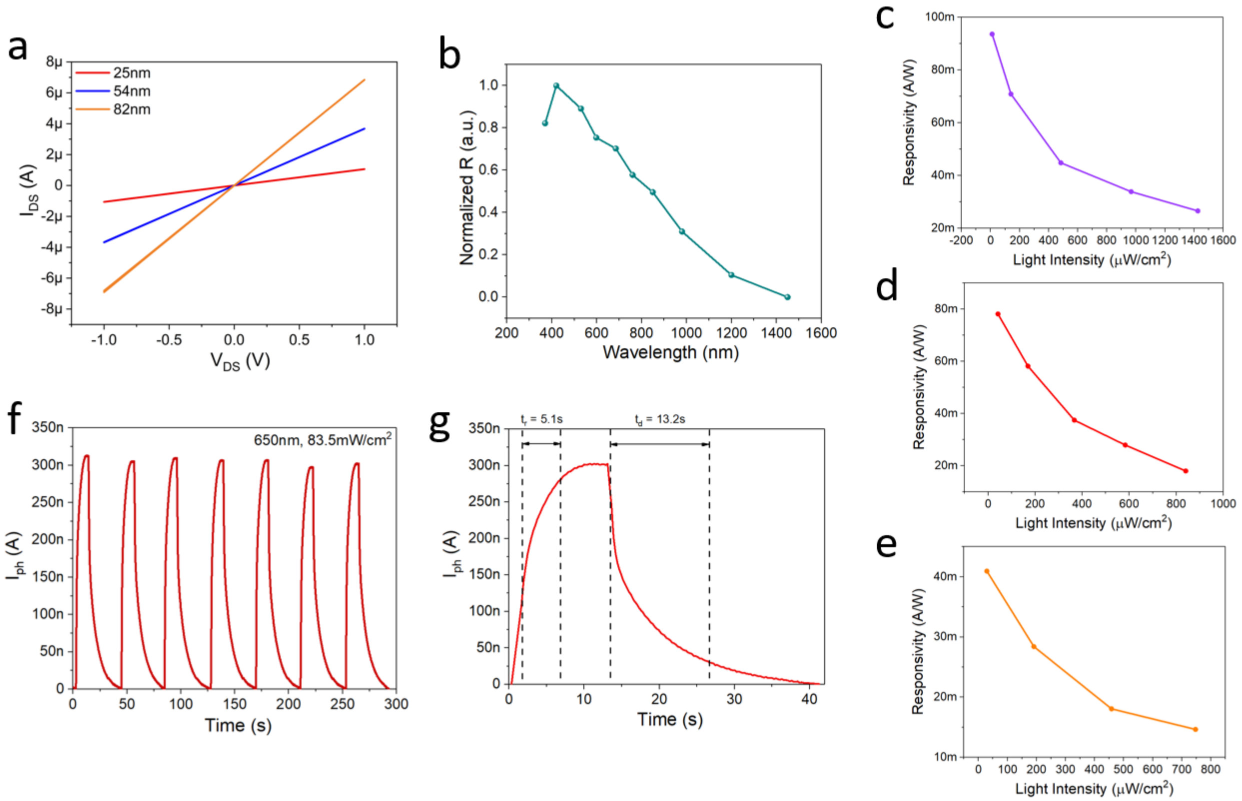

Figure 6.8. (a) I-V curves of devices with different $Cu_3(HHHAT)_2$ thicknesses under dark environment. (b) Spectral response of the Cu3(HHHAT) PD. Responsivity as a function of light intensity of the device under light wavelength of (c) 420 nm, (d) 685 nm and (e) 850 nm. Time-dependent photocurrent of the device. (g) enlarged view of one light on-off cycle, showing the rising and decaying time.

The photoresponsivity measures the sensitivity of a PD. The maximum photoresponsivity of the device is calculated to be 0.94 A/W (**Figure 6.8c**). As revealed in **Figure 6.8c-e**, responsivity decreases with increased intensity for all measured wavelengths. This is expected and is due to the saturation of photocurrent under high light intensity. With a high light intensity, a large number of photo-carriers are accumulated in the $Cu_3(HHHAT)_2$ film. This significantly increases the recombination possibility and reduces the carrier lifetime, resulting in a lower responsivity.

Time-dependent photo-response is also important feature to understand the device working mechanism. The response is stable under multiple light on-off cycles (**Figure 6.8f**), indicating the high working stability of the device. As shown in the enlarged view of time-dependent photo-response curve, the rising time and decay time are measured to be 13.2 s (**Figure 6.8g**).

6.2.3 Top-Gated FET Performance

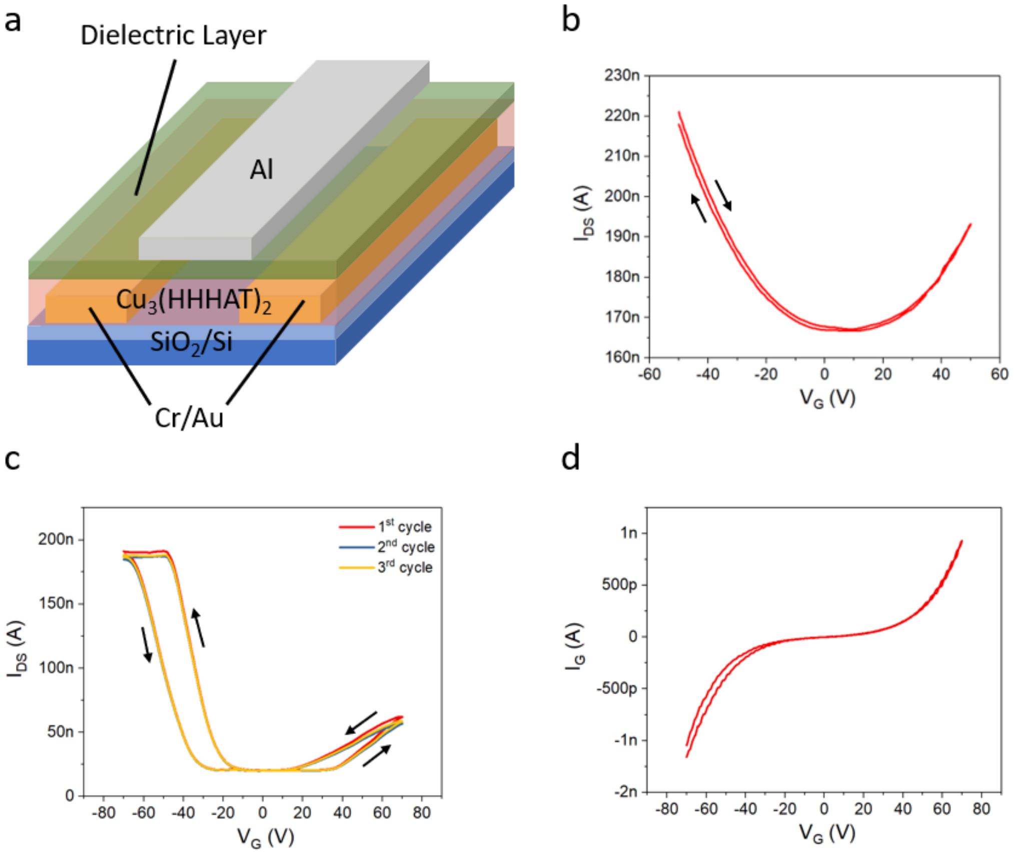

Figure 6.9. (a) Schematic Diagram of the top-gated FET. (b) Transfer curve of the FET when P(VDF-TrFE-CFE) tripolymer is used as dielectric layer. (c) Transfer curve of the FET when P(VDF-TrFE) (65/35 mol%) copolymer is used as dielectric layer. (d) Leakage current as a function of gate voltage when P(VDF-TrFE) (65/35 mol%) copolymer is used as dielectric layer.

To further demonstrate the potential of $Cu_3(HHHAT)_2$ film in electronic applications, we developed a top-gated FET based on $Cu_3(HHHAT)_2$ thin film. By depositing a high-k dielectric P(VDF-TrFE-CFE) (56/36.5/7.5 mol%) (~600 nm) tripolymer on top of the 2D c-MOF film with Al gate electrode (**Figure 6.9a**), we successfully demonstrate the gate modulation of channel conductivity, which has never been done in 2D c-MOF devices. The transistor shows a typical ambipolar behaviour (**Figure 6.9b**) and the channel conductivity can be modulated effectively. The hole and electron mobilities are measured to be and ~0.039 $cm^2/V \cdot s$ and ~0.022 $cm^2/V \cdot s$, respectively.

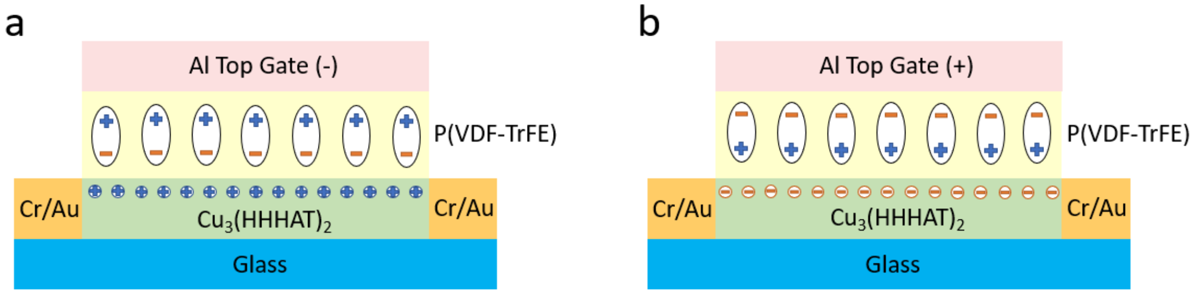

Figure 6.10. Schematic diagrams illustrating the working mechanisms of the ferroelectric transistor working in (a) hole-conductive mode and (b) electron-conductive mode.

Moreover, ferroelectric memory effect can be realized by replacing the P(VDF-TrFE-CFE) tripolymer with ferroelectric P(VDF-TrFE) (65:35) (~350 nm) copolymer. As shown in **Figure 6.9c**, the device shows consistent transfer characteristics under multiple working cycles. It demonstrates counterclockwise hysteresis, which is due to the ferroelectric polarization switching in P(VDF-TrFE) film. The leakage current (**Figure 6.9d**) is negligible when compared to channel current, indicating the high quality of P(VDF-TrFE) film. The electron and hole mobilities are calculated to be ~0.15 $cm^2/V \cdot s$ and ~0.016 $cm^2/V \cdot s$, respectively. It is noted that the carrier mobilities are higher when P(VDF-TrFE) is used instead of P(VDF-TrFE-CFE). This can be attributed to the higher dielectric constant of P(VDF-TrFE-CFE) (~65)[154] than P(VDF-TrFE) (~12)[155], which can induce stronger remote phonon scattering.[156] Notably, hole mobility is higher in both configurations, which may be due to the higher intrinsic hole mobility in $Cu_3(HHHAT)_2$ film. The channel conductivity at off-state is lower in device with P(VDF-TrFE) than that with P(VDF-TrFE-CFE). This could be attributed to the combined effect of different interfacial properties at P(VDF-TrFE)/$Cu_3(HHHAT)_2$ and P(VDF-TrFE-CFE)/$Cu_3(HHHAT)_2$, like surface properties, dipole disorder and surface charge-trapping sites.[157] The interfacial effects can significantly affect bulk properties of bulk conductivity of $Cu_3(HHHAT)_2$ due to its highly porous nature. The device has two operation modes thanks to its ambipolar nature. The device works in hole-conductive mode with a negative gate voltage while it works in electron-conductive mode with a positive gate voltage. The threshold voltages for erased and programmed states in hole-conductive mode are extracted to be -33V and -19V, respectively. On the other hand, the threshold voltages for erased and programmed states in electron-conductive mode are extracted to be 36V and 18V, respectively. The channel current can be modulated by nearly 10 times in hole-conductive mode and more than one time in electron-conductive mode. To operate the device in hole-conductive mode (**Figure 6.10a**), the gate voltage is swept from 0V to -49V, which first poles the P(VDF-TrFE) copolymer and make it in programmed state. The ferroelectric dipole in this case points from Al top gate towards $Cu_3(HHHAT)_2$, such that the holes in $Cu_3(HHHAT)_2$ will be accumulated at the $Cu_3(HHHAT)_2$/ P(VDF-TrFE) interface. The accumulated holes induce a highly conductive channel near the interface, largely increasing the channel conductivity. When the gate voltage sweeps from -60V to -33V, the P(VDF-TrFE) is depolarized and the device is in erased state. When gate voltage sweeps through another direction (**Figure 6.10b**), the electron-conductive mode is achieved and the whole process above is reversed for electrons.

6.3 Conclusion

In summary, the thin film form of $Cu_3(HHHAT)_2$ is developed for the first time. It is confirmed that by various characterizations that the thin film is in high quality and suitable for optoelectronic applications. Considering this, PDs based on $Cu_3(HHHAT)_2$ is fabricated. The device shows broadband photo-response from UV to NIR. Furthermore, gate-modulation of conductivity is first demonstrated for 2D c-MOF devices by a top-gate device configuration. This work clearly demonstrates the potential of high-performance optoelectronic devices based on 2D c-MOFs.

6.4 Experimental Section

6.4.1 Materials characterization

HHHAT: ^1H NMR and ^{13}C NMR spectra were recorded on Bruker AC 300 P using the deuterated solvents ($CDCl_3$, and DMSO-d6) with the tetramethylsilane as the internal reference. High-resolution MALDI-TOF mass spectra were obtained with a Bruker Autoflex MALDI-TOF mass spectrometer. Fourier transform infrared spectroscopy (FTIR) was performed on a Spectrum 100 (Perkin Elmer, Inc., USA) spectrometer with a scan range of 4000-400 cm^{-1}.

$Cu_3(HHHAT)_2$ thin film: The out-of-plane and in-plane XRD spectra was obtained by X-Ray diffraction (XRD), Rigaku SmartLab X-Ray diffractometer. SEM images were observed under a field emission scanning electron microscope (FESEM) (Tescan MAIA3). AFM images were recorded using scanning probe microscope (Bruker NanoScope 8). The thicknesses of the MOF films were characterized by a surface profiler (Bruker DektakXT). The HRTEM image was taken using a field emission electron microscope (JEM-2100F). The absorption spectra were recorded with a LAMBDA 1050+ UV/Vis/NIR spectrophotometer (PerkinElmer). UPS spectra was recorded using an X-Ray Photoelectron Spectrometer System (Thermo Fisher Nexsa).

6.4.2 Device Fabrication

Pre-patterned Substrate preparation: 300nm-SiO_2/Si and PI substrates were cleaned by ultrasonication bath using deionized water, acetone, and IPA, followed by drying the substrate with stream of nitrogen gas. Next, 10nm-Cr/100nm-Au electrodes were deposited by sputtering after the desired area was patterned by standard photolithography process. The channel length and width of the devices used in this work are 5 and 800 μm, respectively. The substrates with electrodes were then replaced in glovebox for later use.

For the top-gated devices, glass substrates were used instead. The bottom and top electrodes are prepared by thermal evaporation through shadow masks. The bottom electrodes are 10nm-Cr/100nm-Au and the top-electrode is 80-nm. The channel length and width of the devices are 100 and 2000 μm, respectively.

Fabrication of $Cu_3(HHHAT)_2$ thin film: The above patterned substrates were first functionalized using oxygen plasma for 30 minutes. Next, the substrates were used for preparing $Cu_3(HHHATT)_2$ according to previous report.[42, 45] The functionalized substrates were immersed alternatively into copper acetate and HHHAT with various concentration for 20 minutes and 40 minutes (**Figure 6.4**). Ethanol, IPA and DMF were employed as solvents for both precursors. Devices fabricated by ethanolic solutions were used for most of the measurement. The substrates were washed with corresponding solvents to remove excessive precursor between each immersion step. The film thickness can be controlled by cycle numbers. The process is stopped after desired thickness is achieved, and the substrate is stored in a N_2-filled glove box.

Fabrication of dielectric layers on $Cu_3(HHHAT)_2$ thin film: To fabricate P(VDF-TrFE-CFE) thin films, P(VDF-TrFE-CFE) (56/36.5/7.5 mol%) powder was dissolved into methyl ethyl ketone (MEK) at a concentration of 70 mg/ml and spin-coated onto the $Cu_3(HHHAT)_2$ thin film with a speed of 3000 rpm, followed by annealing at 60 degree for 2 hours. To fabricate P(VDF-TrFE) thin films, P(VDF-TrFE) (65/35 mol%) powder was dissolved into methyl ethyl ketone (MEK) at a concentration of 40 mg/ml and spin-coated onto the $Cu_3(HHHAT)_2$ thin film with a speed of 3000 rpm, followed by annealing at 110 degree for 2 hours.

6.4.3 Estimation of Grain Size and Mircostrain Based on XRD Data

The grain size and macrostrain of the $Cu_3(HHHAT)_2$ are estimated according to UDM of W-H method, which assumes uniform strain in all crystilline directions and is used extensively for polycrystaline materials.[2] In this model, the peak broadening or full width at half maximum (FWHM) for each XRD peak can be expressed as:[2]

$$\beta_{hkl} = \left(\frac{k\lambda}{D cos\theta}\right) + 4\varepsilon tan\theta, \qquad (1)$$

where k, D and ε are shape factor, crystal size and microstrain. Rearranging the equation yields the following:

$$\beta_{hkl} cos\theta = \frac{k\lambda}{D} + 4\varepsilon sin\theta \qquad (2)$$

A W-H plot is obtained by ploting $\beta_{hkl} cos\theta$ against $4sin\theta$ (Figure S6b). The value of k is assigned to be 0.94, which is a general value originally derived by Scherrer and used widely for thin films.[3] From linear fitting of the data, crystal size and microstrain can be estimated from the y-intercept and the slope.

Chapter 7: Conclusions and Perspectives

7.1 Conclusions

In this thesis, high-performance PDs based on novel hybrid perovskites and 2D c-MOFs have been fabricated. The material and device physics are studied carefully. The results clearly indicated the huge potential for these materials being used in practical applications.

First, a high-performance PD based on $FASnI_3$/PEDOT:PSS have been developed. The device performance is largely improved when compared to bare $FASnI_3$ and PEDOT:PSS devices thanks to the photogating effect. The resultant responsivity and gain is 2.6×10^6 A/W and 4.7×10^6, respectively. Higher response time and detectivity can be further achieved by reducing the PDDOT:PSS thickness. Flexible devices can also be demonstrated with excellent mechanical stability. This work opens up the window for using vertical heterojunction to enhance PD performance.

Then, a sensitive phototransistor based on quasi-2D perovskite/SWCNT vertical heterojunction is reported. Thanks to the excellent optical properties and self-constructed vertical gradient type-II heterostructure of quasi-2D perovskite and the outstanding transport properties of SWCNT, superior responsivity and detectivity of 2×10^6 A/W and 7×10^{14} Jones is obtained. High on/off ratio of 10^3 is also achieved. This work demonstrates the huge potential of quasi-2D perovskite/SWCNT phototransistor for next-generation PDs.

After that, we first report the successful growth of high-quality $Cu_3(HHTT)_2$ thin film. The transport behavior is carefully studied through AC and temperature dependent conductivity measurements. Ultrabroadband photoconductor with reliable response from UV to Mid-IR under room temperature has been demonstrated. Moreover, the PD shows a typical synaptic behavior under light and exhibit outstanding data recognition accuracy in artificial neural networks. This work clearly demonstrates the promising potential of 2D c-MOFs in high-performance and multi-functional optoelectronic devices.

Finally, the first report of the thin film form of another 2D c-MOF, $Cu_3(HHHAT)_2$ has been demonstrated. Materials characterization indicate the thin film is in desired quality for optoelectronic devices. PD with response from UV to NIR. Field-effect modulation of conductivity and more importantly, ferroelectric memory effect, are also demonstrated for the first time for 2D c-MOF thin films. The work opens up a window for further development of high-performance optoelectronic devices based on 2D c-MOFs.

7.2 Perspectives

Developing new material is a promising direction. As discussed in the thesis, semiconductor is one of the key elements in obtaining high-performance PDs. Although a great deal of research effort has been put in developing semiconductor materials with high mobility, excellent optical absorption coefficient, direct band gap, environmentally friendly, superior mechanical flexibility and outstanding air stability, all of those novel materials cannot simultaneously fulfil the requirements for ideal next-generation functional materials. For instance, the Sn-perovskites still suffer from the severe oxidation issue in ambient air; 2D c-MOFs nowadays have relatively low optical absorption coefficient. Therefore, it will be important for materials scientists and chemists play an important role for inventing even more suitable semiconducting materials for future optoelectronic devices.

Constructing novel device structure is another possible way to enhance the device performance. As mentioned in the thesis, device design is also critical for device performance. Vertical heterojunction with a light absorbing layer and carrier transporting layer is a typical example for enhancing performance by decoupling the requirements of the channel material, as demonstrated earlier in this thesis. However, the two materials still need to have suitable band alignment. The top-layer must also be fabricated on top of bottom-layer, which can sometimes cause technical difficulties. Therefore, more innovative design is urgently needed for better utilizing the materials properties of the channel materials.

The better understanding of thin film physics based on the novel materials and/or the interfaces formed by these materials may lead to more rational device designs and higher material quality. For instance, the lack of knowledge in thin film growth severely limiting the thin film quality for 2D c-MOF thin films. The potential for practical applications of 2D c-MOFs in optoelectronics will be fully revealed only when thin films with large crystal size can be fabricated with feasible method. On the other hand, the transport and optoelectronic processes for the novel OIHP thin films are under active research, which may lead to further improved optoelectronic performance.

Developing large area array of PDs is an essential step for commercialization. By optimizing fabrication processes and fine-tuning of materials properties, wearable sensitive PDs can be assembled into large area array for image capture and other advanced applications. Taking the advantages of excellent optoelectronic properties of novel functional materials like emerging hybrid perovskites and 2D c-MOFs, lightweight wearable optoelectronic system with multi-functionalities such as healthcare and imaging recording can be developed.

With the latest rapid development of semiconductors and novel device structure like artificial eye based on hybrid perovskites, PDs have been explored for tremendous emerging applications beyond the traditional ones. The continuous research in both device physics and exploration of innovative applications will no doubt lead to a world with convenience and safety.

References

[1] Y. Wang, D. Li, L. Chao, T. Niu, Y. Chen, W. Huang, *Applied Materials Today* **2022**, 28, 101509.
[2] G. Grancini, M. K. Nazeeruddin, *Nature Reviews Materials* **2019**, 4, 4.
[3] F. Wang, X. Zou, M. Xu, H. Wang, H. Wang, H. Guo, J. Guo, P. Wang, M. Peng, Z. Wang, Y. Wang, J. Miao, F. Chen, J. Wang, X. Chen, A. Pan, C. Shan, L. Liao, W. Hu, *Advanced Science* **2021**, 8, 2100569.
[4] J. Liu, Y. Chen, X. Feng, R. Dong, *Small Structures* **2022**, 3, 2100210.
[5] M. Wang, R. Dong, X. Feng, *Chemical Society Reviews* **2021**, 50, 2764.
[6] S. M. Sze, K. K. Ng, in *Physics of Semiconductor Devices: Third Edition*, DOI: 10.1002/9780470068328, 2006.
[7] P. C. Y. Chow, T. Someya, Vol. 1902045, 2020, 1.
[8] F. Yu, S. Wu, X. Wang, G. Zhang, H. Lu, L. Qiu, in *RSC Adv.*, Vol. 7, Royal Society of Chemistry, 2017, 11572.
[9] C. Xie, C.-K. Liu, H.-L. Loi, F. Yan, *Advanced Functional Materials* **2020**, 30, 1903907.
[10] Y. Park, S. Lee, H. J. Park, H. W. Baac, G. Yoo, J. Heo, in *Journal of Nanoscience and Nanotechnology*, Vol. 16, 2016, 11722.
[11] a) S.-l. M. Phototransistors, **2012**, DOI: 10.1021/nn202455774; b) C. Soci, A. Zhang, B. Xiang, S. A. Dayeh, D. P. R. Aplin, J. Park, X. Y. Bao, Y. H. Lo, D. Wang, *Nano Letters* **2007**, 7, 1003; c) M. Chen, X. Lan, X. Tang, Y. Wang, M. H. Hudson, D. V. Talapin, P. Guyot-Sionnest, *ACS Photonics* **2019**, 6, 2358.
[12] M. Ahmadi, T. Wu, B. Hu, in *Advanced Materials*, Vol. 29, 2017, 1605242.
[13] A. M. Al-Amri, B. Cheng, J.-H. He, in *IEEE Transactions on Nanotechnology*, Vol. 18, IEEE, 2019, 1.
[14] A. Kojima, K. Teshima, Y. Shirai, T. Miyasaka, *Journal of the American Chemical Society* **2009**, 131, 6050.
[15] J. Sun, J. Wu, X. Tong, F. Lin, Y. Wang, Z. M. Wang, *Advanced Science* **2018**, 5, 1700780.
[16] Y. Wu, Q. Wang, Y. Chen, W. Qiu, Q. Peng, *Energy & Environmental Science* **2022**, 15, 4700.
[17] S. Wei, F. Wang, X. Zou, L. Wang, C. Liu, X. Liu, W. Hu, Z. Fan, J. C. Ho, L. Liao, *Advanced Materials* **2020**, 32, 1907527.
[18] Q. Tai, K.-C. Tang, F. Yan, *Energy & Environmental Science* **2019**, 12, 2375.
[19] H.-Y. Hou, S. Tian, H.-R. Ge, J.-D. Chen, Y.-Q. Li, J.-X. Tang, *Advanced Functional Materials* n/a, 2209324.
[20] C.-K. Liu, Q. Tai, N. Wang, G. Tang, H.-L. Loi, F. Yan, *Advanced Science* **2019**, 6, 1900751.
[21] J. Yan, Y. Cui, M. Xie, G. Z. Yang, D. S. Bin, D. Li, *Angew Chem Int Ed Engl* **2021**, 60, 24467.
[22] T. Wang, L. Gao, J. Hou, S. J. A. Herou, J. T. Griffiths, W. Li, J. Dong, S. Gao, M. M. Titirici, R. V. Kumar, A. K. Cheetham, X. Bao, Q. Fu, S. K. Smoukov, *Nature Communications* **2019**, 10, 1340.
[23] J. Lee, O. K. Farha, J. Roberts, K. A. Scheidt, S. T. Nguyen, J. T. Hupp, *Chemical Society Reviews* **2009**, 38, 1450.
[24] C. Zhu, R. E. Gerald, Y. Chen, J. Huang, *Sensors and Actuators B: Chemical* **2020**, 321, 128608.
[25] D. DeSantis, J. A. Mason, B. D. James, C. Houchins, J. R. Long, M. Veenstra, *Energy and Fuels* **2017**, 31, 2024.
[26] G. Chakraborty, I. H. Park, R. Medishetty, J. J. Vittal, in *Chemical Reviews*, Vol. 121, 2021, 3751.
[27] R. Dong, P. Han, H. Arora, M. Ballabio, M. Karakus, Z. Zhang, C. Shekhar, P. Adler, P. S. Petkov, A. Erbe, S. C. B. Mannsfeld, C. Felser, T. Heine, M. Bonn, X. Feng, E. Cánovas, *Nature Materials* **2018**, 17, 1027.
[28] J. Huang, J. Du, Z. Cevher, Y. Ren, X. Wu, Y. Chu, *Advanced Functional Materials* **2017**, 27, 1604163.
[29] H. Wang, H. Wang, **2017**, 46.
[30] M. Ahmadi, T. Wu, B. Hu, *Advanced Materials* **2017**, 29, 1605242.
[31] L. Wang, X. Zou, J. Lin, J. Jiang, Y. Liu, X. Liu, X. Zhao, Y. F. Liu, J. C. Ho, L. Liao, *ACS Nano* **2019**, 13, 4804.
[32] C. Xie, F. Yan, *ACS Applied Materials & Interfaces* **2017**, 9, 1569.
[33] C. Liang, D. Zhao, Y. Li, X. Li, S. Peng, G. Shao, G. Xing, *Energy & Environmental Materials* **2018**, 1, 221.
[34] C. H. Ji, K. T. Kim, S. Y. Oh, *RSC Advances* **2018**, 8, 8302.
[35] X. Hu, X. Zhang, L. Liang, J. Bao, S. Li, W. Yang, Y. Xie, *Advanced Functional Materials* **2014**, 24, 7373.
[36] Y. Chen, Y. Sun, J. Peng, J. Tang, K. Zheng, Z. Liang, *Advanced Materials* **2018**, 30, 1703487.
[37] A. Waleed, M. M. Tavakoli, L. Gu, Z. Wang, D. Zhang, A. Manikandan, Q. Zhang, R. Zhang, Y.-L. Chueh, Z. Fan, *Nano Letters* **2017**, 17, 523.
[38] X. W. Tong, W. Y. Kong, Y. Y. Wang, J. M. Zhu, L. B. Luo, Z. H. Wang, *ACS Applied Materials and Interfaces* **2017**, 9, 18977.

References

[39] C. Huo, B. Cai, Z. Yuan, B. Ma, H. Zeng, *Small Methods* **2017**, 1, 1600018.

[40] K. Wang, C. Wu, D. Yang, Y. Jiang, S. Priya, *ACS Nano* **2018**, 12, 4919.

[41] Y. Shao, Y. Liu, X. Chen, C. Chen, I. Sarpkaya, Z. Chen, Y. Fang, J. Kong, K. Watanabe, T. Taniguchi, A. Taylor, J. Huang, F. Xia, *Nano Letters* **2017**, 17, 7330.

[42] J. Song, J. Zheng, A. Yang, H. Liu, Z. Zhao, N. Wang, F. Yan, *Materials Chemistry Frontiers* **2021**, 5, 3422.

[43] K. W. Nam, S. S. Park, R. dos Reis, V. P. Dravid, H. Kim, C. A. Mirkin, J. F. Stoddart, *Nature Communications* **2019**, 10, 4948.

[44] J. Liu, D. Yang, Y. Zhou, G. Zhang, G. Xing, Y. Liu, Y. Ma, O. Terasaki, S. Yang, L. Chen, *Angewandte Chemie - International Edition* **2021**, 60, 14473.

[45] C.-K. Liu, V. Piradi, J. Song, Z. Wang, L.-W. Wong, E.-H.-L. Tan, J. Zhao, X. Zhu, F. Yan, *Advanced Materials* **2022**, 34, 2204140.

[46] H. Arora, R. Dong, T. Venanzi, J. Zscharschuch, H. Schneider, M. Helm, X. Feng, E. Cánovas, A. Erbe, *Advanced Materials* **2020**, 32, 1907063.

[47] a) Y. Zhao, K. Zhu, *Chemical Society Reviews* **2016**, 45, 655; b) J. S. Manser, J. A. Christians, P. V. Kamat, *Chemical Reviews* **2016**, 116, 12956; c) Q. Chen, N. De Marco, Y. Yang, T.-B. Song, C.-C. Chen, H. Zhao, Z. Hong, H. Zhou, Y. Yang, *Nano Today* **2015**, 10, 355.

[48] F. P. García de Arquer, A. Armin, P. Meredith, E. H. Sargent, *Nature Reviews Materials* **2017**, 2, 16100.

[49] a) L. Qian, Y. Sun, M. Wu, C. Li, D. Xie, L. Ding, G. Shi, *Nanoscale* **2018**, 10, 6837; b) J. Song, L. Xu, J. Li, J. Xue, Y. Dong, X. Li, H. Zeng, *Advanced Materials* **2016**, 28, 4861; c) C. Xie, P. You, Z. Liu, L. Li, F. Yan, *Light: Science &Amp; Applications* **2017**, 6, e17023.

[50] G. Tang, P. You, Q. Tai, R. Wu, F. Yan, *Solar RRL* **2018**, 0, 1800066.

[51] F. Li, C. Ma, H. Wang, W. Hu, W. Yu, A. D. Sheikh, T. Wu, *Nature communications* **2015**, 6, 8238.

[52] M. Spina, M. Lehmann, B. Náfrádi, L. Bernard, E. Bonvin, R. Gaál, A. Magrez, L. Forró, E. Horváth, *Small* **2015**, 11, 4824.

[53] Z.-Y. Peng, J.-L. Xu, J.-Y. Zhang, X. Gao, S.-D. Wang, *Advanced Materials Interfaces* **2018**, 5, 1800505.

[54] X. Zou, Y. Li, G. Tang, P. You, F. Yan, *Small* **2019**, 15, 1901004.

[55] A. Demayo, M. C. Taylor, K. W. Taylor, P. V. Hodson, *C R C Critical Reviews in Environmental Control* **1982**, 12, 257.

[56] a) Q. Tai, X. Guo, G. Tang, P. You, T. W. Ng, D. Shen, J. Cao, C. K. Liu, N. Wang, Y. Zhu, C. S. Lee, F. Yan, *Angewandte Chemie - International Edition* **2019**, 58, 806; b) N. K. Noel, S. D. Stranks, A. Abate, C. Wehrenfennig, S. Guarnera, A. A. Haghighirad, A. Sadhanala, G. E. Eperon, S. K. Pathak, M. B. Johnston, A. Petrozza, L. M. Herz, H. J. Snaith, *Energy and Environmental Science* **2014**, 7, 3061; c) T. Leijtens, R. Prasanna, A. Gold-Parker, M. F. Toney, M. D. McGehee, *ACS Energy Letters* **2017**, 2, 2159.

[57] C. Ji, P. Wang, Z. Wu, Z. Sun, L. Li, J. Zhang, W. Hu, M. Hong, J. Luo, *Advanced Functional Materials* **2018**, 28, 1705467.

[58] B. Yang, Y. J. Li, Y. X. Tang, X. Mao, C. Luo, M. S. Wang, W. Q. Deng, K. L. Han, *Journal of Physical Chemistry Letters* **2018**, 9, 3087.

[59] S. D. Stranks, V. M. Burlakov, T. Leijtens, J. M. Ball, A. Goriely, H. J. Snaith, *Physical Review Applied* **2014**, 2, 034007.

[60] a) W. Liao, D. Zhao, Y. Yu, C. R. Grice, C. Wang, A. J. Cimaroli, P. Schulz, W. Meng, K. Zhu, R. G. Xiong, Y. Yan, *Advanced Materials* **2016**, 28, 9333; b) P. Docampo, J. M. Ball, M. Darwich, G. E. Eperon, H. J. Snaith, *Nature Communications* **2013**, 4, 1.

[61] F. Yu, S. Wu, X. Wang, G. Zhang, H. Lu, L. Qiu, *RSC Adv.* **2017**, 7, 11572.

[62] a) Y. Yuan, J. Huang, *Accounts of Chemical Research* **2016**, 49, 286; b) Q. Wei, M. Mukaida, Y. Naitoh, T. Ishida, *Advanced Materials* **2013**, 25, 2831; c) E. Stavrinidou, P. Leleux, H. Rajaona, D. Khodagholy, J. Rivnay, M. Lindau, S. Sanaur, G. G. Malliaras, *Advanced Materials* **2013**, 25, 4488.

[63] a) T. M. Koh, T. Krishnamoorthy, N. Yantara, C. Shi, W. L. Leong, P. P. Boix, A. C. Grimsdale, S. G. Mhaisalkar, N. Mathews, *Journal of Materials Chemistry A* **2015**, 3, 14996; b) W. Ke, C. C. Stoumpos, M. Zhu, L. Mao, I. Spanopoulos, J. Liu, O. Y. Kontsevoi, M. Chen, D. Sarma, Y. Zhang, M. R. Wasielewski, M. G. Kanatzidis, *Science Advances* 3, e1701293.

[64] C. Bi, Q. Wang, Y. Shao, Y. Yuan, Z. Xiao, J. Huang, *Nature Communications* **2015**, 6, 7747.

[65] a) L. Qin, L. Wu, B. Kattel, C. Li, Y. Zhang, Y. Hou, J. Wu, W. L. Chan, *Advanced Functional Materials* **2017**, 27, 1704173; b) A. A. Bessonov, M. Allen, Y. Liu, S. Malik, J. Bottomley, A. Rushton, I. Medina-Salazar, M. Voutilainen, S. Kallioinen, A. Colli, C. Bower, P. Andrew, T. Ryhänen, *ACS Nano* **2017**, 11, 5547.

[66] Z. Sun, Z. Liu, J. Li, G.-a. Tai, S.-P. Lau, F. Yan, *Advanced Materials* **2012**, 24, 5878.

References

[67] a) D.-H. Kang, S. R. Pae, J. Shim, G. Yoo, J. Jeon, J. W. Leem, J. S. Yu, S. Lee, B. Shin, J.-H. Park, *Advanced Materials* **2016**, 28, 7799; b) H. Wu, H. Si, Z. Zhang, Z. Kang, P. Wu, L. Zhou, S. Zhang, Z. Zhang, Q. Liao, Y. Zhang, *Advanced Science* **2018**, 5, 1801219.

[68] H. S. Jung, N.-g. Park, *SMALL* **2015**, 11, 10.

[69] H. Beneking, *IEEE Transactions on Electron Devices* **1982**, 29, 1420

[70] a) Z. Sun, L. Aigouy, Z. Chen, *Nanoscale* **2016**, 8, 7377; b) M. Sun, Q. Fang, Z. Zhang, D. Xie, Y. Sun, J. Xu, W. Li, T. Ren, Y. Zhang, *ACS Applied Materials & Interfaces* **2018**, 10, 7231; c) Y. Lee, J. Kwon, E. Hwang, C. H. Ra, W. J. Yoo, J. H. Ahn, J. H. Park, J. H. Cho, *Advanced Materials* **2015**, 27, 41; d) L. B. Luo, G. A. Wu, Y. Gao, L. Liang, C. Xie, Z. X. Zhang, X. W. Tong, T. Wang, F. X. Liang, *Advanced Optical Materials* **2019**, DOI: 10.1002/adom.2019002721900272.

[71] a) Y. Sun, J. A. Rogers, *Advanced Materials* **2007**, 19, 1897; b) C. Xie, F. Yan, *Small* **2017**, 13, 1701822.

[72] a) P. C. Y. Chow, T. Someya, **2020**, 1902045, 1; b) J. Zhou, J. Huang, *Advanced Science* **2018**, 5, 1700256.

[73] M. Long, P. Wang, H. Fang, W. Hu, **2019**, 1803807, 1.

[74] A. M. Al-Amri, B. Cheng, J.-H. He, *IEEE Transactions on Nanotechnology* **2019**, 18, 1.

[75] C.-k. Liu, Q. Tai, N. Wang, G. Tang, Z. Hu, F. Yan, *ACS Appl .Mater. Interfaces* **2020**, 12, 18769.

[76] a) J. Yang, B. D. Siempelkamp, D. Liu, T. L. Kelly, *ACS Nano* **2015**, 9, 1955; b) G. Niu, W. Li, F. Meng, L. Wang, H. Dong, Y. Qiu, *J. Mater. Chem. A* **2014**, 2, 705.

[77] V. Q. Dang, G. S. Han, T. Q. Trung, L. T. Duy, Y. U. Jin, B. U. Hwang, H. S. Jung, N. E. Lee, *Carbon* **2016**, 105, 353.

[78] C. Fang, H. Wang, Z. Shen, H. Shen, S. Wang, J. Ma, J. Wang, H. Luo, D. Li, *ACS Applied Materials and Interfaces* **2019**, 11, 8419.

[79] D.-H. Kwak, D.-H. Lim, H.-S. Ra, P. Ramasamy, J.-S. Lee, *RSC Adv.* **2016**, 6, 65252.

[80] a) K. O. Brinkmann, J. Zhao, N. Pourdavoud, T. Becker, T. Hu, S. Olthof, K. Meerholz, L. Hoffmann, T. Gahlmann, R. Heiderhoff, M. F. Oszajca, N. A. Luechinger, D. Rogalla, Y. Chen, B. Cheng, T. Riedl, *Nature Communications* **2017**, 8, 13938; b) Q. Tai, X. Guo, G. Tang, P. You, T.-W. Ng, D. Shen, J. Cao, C.-K. Liu, N. Wang, Y. Zhu, C.-S. Lee, F. Yan, *Angewandte Chemie International Edition* **2019**, 58, 806; c) S. Gupta, D. Cahen, G. Hodes, *The Journal of Physical Chemistry C* **2018**, 122, 13926; d) P. Ramasamy, D.-H. Lim, B. Kim, S.-H. Lee, M.-S. Lee, J.-S. Lee, *Chemical Communications* **2016**, 52, 2067.

[81] R. Yang, R. Li, Y. Cao, Y. Wei, Y. Miao, W. L. Tan, X. Jiao, H. Chen, L. Zhang, Q. Chen, *Advanced Materials* **2018**, 30, 1804771.

[82] H.-l. Loi, J. Cao, X. Guo, C.-k. Liu, N. Wang, J. Song, *Adv. Sci.* **2020**, 2000776, 1.

[83] X. Liu, D. Yu, X. Song, H. Zeng, *Small* **2018**, 14, 1801460.

[84] a) P. Schulz, A.-M. Dowgiallo, M. Yang, K. Zhu, J. L. Blackburn, J. J. Berry, *The Journal of Physical Chemistry Letters* **2016**, 7, 418; b) M. Yuan, L. N. Quan, R. Comin, G. Walters, R. Sabatini, O. Voznyy, S. Hoogland, Y. Zhao, E. M. Beauregard, P. Kanjanaboos, Z. Lu, D. H. Kim, E. H. Sargent, *Nature Nanotechnology* **2016**, 11, 1.

[85] Y. Wang, Y. Zhang, Y. Lu, W. Xu, H. Mu, C. Chen, H. Qiao, J. Song, S. Li, B. Sun, Y.-B. Cheng, Q. Bao, *Advanced Optical Materials* **2015**, 3, 1389.

[86] F. Li, H. Wang, D. Kufer, L. Liang, W. Yu, E. Alarousu, C. Ma, Y. Li, Z. Liu, C. Liu, N. Wei, F. Wang, L. Chen, O. F. Mohammed, A. Fratalocchi, X. Liu, G. Konstantatos, T. Wu, *Advanced Materials* **2017**, 29, 1602432.

[87] a) C. Ma, S. Clark, Z. Liu, L. Liang, Y. Firdaus, R. Tao, A. Han, X. Liu, L. J. Li, T. D. Anthopoulos, M. C. Hersam, T. Wu, *ACS nano* **2020**, 14, 3969; b) J. Zhao, L. Shen, F. Liu, P. Zhao, Q. Huang, H. Han, L. Peng, X. Liang, *Nano Research* **2020**, 13, 1749.

[88] G. Dong, J. Zhao, L. Shen, J. Xia, H. Meng, W. Yu, Q. Huang, H. Han, *Nano Research* **2018**, 11, 4356.

[89] a) A. I. López-Lorente, B. M. Simonet, M. Valcárcel, *Analyst* **2014**, 139, 290; b) K. Kumar, Y.-S. Kim, X. Li, J. Ding, F. T. Fisher, E.-H. Yang, *Chemistry of Materials* **2013**, 25, 3874.

[90] a) M.-K. Li, T.-P. Chen, Y.-F. Lin, C. M. Raghavan, W.-L. Chen, S.-H. Yang, R. Sankar, C.-W. Luo, Y.-M. Chang, C.-W. Chen, *Small* **2018**, 14, 1803763; b) F. Zhang, H. Zhang, L. Zhu, L. Qin, Y. Wang, Y. Hu, Z. Lou, Y. Hou, F. Teng, *Journal of Materials Chemistry C* **2019**, 7, 4004.

[91] a) D.-H. Kang, S. R. Pae, J. Shim, G. Yoo, J. Jeon, J. W. Leem, J. S. Yu, S. Lee, B. Shin, J.-H. Park, *Advanced Materials* **2016**, 28, 7799; b) S. Wei, F. Wang, X. Zou, L. Wang, C. Liu, X. Liu, W. Hu, Z. Fan, J. C. Ho, L. Liao, *Advanced Materials* **2020**, 32, 1907527; c) H. Wu, H. Si, Z. Zhang, Z. Kang, P. Wu, L. Zhou, S. Zhang, Z. Zhang, Q. Liao, Y. Zhang, *Advanced Science* **2018**, 5, 1801219.

[92] F. H. L. Koppens, T. Mueller, P. Avouris, A. C. Ferrari, M. S. Vitiello, M. Polini, *Nature Nanotechnology* **2014**, 9, 780.

References

[93] L. Qian, Y. Sun, M. Wu, D. Xie, L. Ding, G. Shi, *Advanced Materials* **2017**, 29, 1606175.

[94] J. H. Dou, M. Q. Arguilla, Y. Luo, J. Li, W. Zhang, L. Sun, J. L. Mancuso, L. Yang, T. Chen, L. R. Parent, G. Skorupskii, N. J. Libretto, C. Sun, M. C. Yang, P. V. Dip, E. J. Brignole, J. T. Miller, J. Kong, C. H. Hendon, J. Sun, M. Dincă, *Nature Materials* **2021**, 20, 222.

[95] a) L. Chen, Q. Xu, *Matter* **2019**, 1, 57; b) L. E. Kreno, K. Leong, O. K. Farha, M. Allendorf, R. P. Van Duyne, J. T. Hupp, *Chemical Reviews* **2012**, 112, 1105; c) Y. S. Wei, M. Zhang, R. Zou, Q. Xu, *Chemical Reviews* **2020**, 120, 12089.

[96] a) M. S. Yao, X. J. Lv, Z. H. Fu, W. H. Li, W. H. Deng, G. D. Wu, G. Xu, *Angew. Chem. Int. Ed.* **2017**, 56, 16510; b) M. S. Yao, J. J. Zheng, A. Q. Wu, G. Xu, S. S. Nagarkar, G. Zhang, M. Tsujimoto, S. Sakaki, S. Horike, K. Otake, S. Kitagawa, *Angewandte Chemie - International Edition* **2020**, 59, 172.

[97] a) L. Rosi Nathaniel, J. Eckert, M. Eddaoudi, T. Vodak David, J. Kim, M. O'Keeffe, M. Yaghi Omar, *Science* **2003**, 300, 1127; b) T. Qiu, Z. Liang, W. Guo, H. Tabassum, S. Gao, R. Zou, *ACS Energy Letters* **2020**, 5, 520; c) B. Xiao, P. S. Wheatley, X. Zhao, A. J. Fletcher, S. Fox, A. G. Rossi, I. L. Megson, S. Bordiga, L. Regli, K. M. Thomas, R. E. Morris, *Journal of the American Chemical Society* **2007**, 129, 1203; d) Q. Jiang, P. Xiong, J. Liu, Z. Xie, Q. Wang, X. Q. Yang, E. Hu, Y. Cao, J. Sun, Y. Xu, L. Chen, *Angewandte Chemie - International Edition* **2020**, 59, 5273.

[98] a) B. Li, H. M. Wen, Y. Cui, W. Zhou, G. Qian, B. Chen, *Advanced Materials* **2016**, 28, 8819; b) A. Bétard, R. A. Fischer, *Chemical Reviews* **2012**, 112, 1055; c) B. Li, H.-M. Wen, Y. Cui, W. Zhou, G. Qian, B. Chen, *Advanced Materials* **2016**, 28, 8819.

[99] a) M. Wang, R. Dong, X. Feng, *Chemical Society Reviews* **2021**, 50, 2764; b) J. Su, W. He, X. M. Li, L. Sun, H. Y. Wang, Y. Q. Lan, M. Ding, J. L. Zuo, *Matter* **2020**, 2, 711.

[100] a) X. Ren, G. Liao, Z. Li, H. Qiao, Y. Zhang, X. Yu, B. Wang, H. Tan, L. Shi, X. Qi, H. Zhang, *Coordination Chemistry Reviews* **2021**, 435, 213781; b) G. Chakraborty, I. H. Park, R. Medishetty, J. J. Vittal, *Chemical Reviews* **2021**, 121, 3751.

[101] a) G. Wu, J. Huang, Y. Zang, J. He, G. Xu, *Journal of the American Chemical Society* **2017**, 139, 1360; b) B. Wang, Y. Luo, B. Liu, G. Duan, *ACS Applied Materials and Interfaces* **2019**, 11, 35935.

[102] a) D. Sheberla, J. C. Bachman, J. S. Elias, C. J. Sun, Y. Shao-Horn, M. Dincă, *Nature Materials* **2017**, 16, 220; b) W. H. Li, K. Ding, H. R. Tian, M. S. Yao, B. Nath, W. H. Deng, Y. Wang, G. Xu, *Advanced Functional Materials* **2017**, 27, 1702067; c) W. Zhao, T. Chen, W. Wang, S. Bi, M. Jiang, K. Y. Zhang, S. Liu, W. Huang, Q. Zhao, *Advanced Materials Interfaces* **2021**, 8, 2100308.

[103] M. G. Campbell, S. F. Liu, T. M. Swager, M. Dincə, *Journal of the American Chemical Society* **2015**, 137, 13780.

[104] K. Jayaramulu, D. P. Dubal, A. Schneemann, V. Ranc, C. Perez-Reyes, J. Stráská, Š. Kment, M. Otyepka, R. A. Fischer, R. Zbořil, *Advanced Functional Materials* **2019**, 29, 1902539.

[105] a) Y. Liu, Y. Wei, M. Liu, Y. Bai, X. Wang, S. Shang, C. Du, W. Gao, J. Chen, Y. Liu, *Advanced Materials* **2021**, 33, 1; b) M.-S. Yao, X.-J. Lv, Z.-H. Fu, W.-H. Li, W.-H. Deng, G.-D. Wu, G. Xu, *Angewandte Chemie* **2017**, 129, 16737.

[106] H. Li, X. Jiang, W. Ye, H. Zhang, L. Zhou, F. Zhang, D. She, Y. Zhou, S.-T. Han, *Nano Energy* **2019**, 65, 104000.

[107] Y. Liu, Y. Wei, M. Liu, Y. Bai, G. Liu, X. Wang, S. Shang, W. Gao, C. Du, J. Chen, Y. Liu, *Angewandte Chemie - International Edition* **2021**, 60, 17440.

[108] W. Zhao, T. Chen, W. Wang, S. Bi, M. Jiang, K. Y. Zhang, S. Liu, W. Huang, Q. Zhao, *Advanced Materials Interfaces* **2021**, 8, 2100308.

[109] a) J. H. Hildebrand, G. J. Rotariu, *Analytical Chemistry* **1952**, 24, 770; b) H. F. Huber, C. Thies, *Journal of Polymer Science Part A-2: Polymer Physics* **1970**, 8, 71.

[110] J. Hwang, R. Yan, M. Oschatz, B. V. Schmidt, *Journal of Materials Chemistry A* **2018**, 6, 23521.

[111] a) X. Song, X. Wang, Y. Li, C. Zheng, B. Zhang, C.-a. Di, F. Li, C. Jin, W. Mi, L. Chen, W. Hu, *Angewandte Chemie International Edition* **2020**, 59, 1118; b) T. Lee, J.-O. Kim, C. Park, H. Kim, M. Kim, H. Park, I. Kim, J. Ko, K. Pak, S. Q. Choi, I.-D. Kim, S. Park, *Advanced Materials* **2022**, 34, 2107696.

[112] V. Mote, Y. Purushotham, B. Dole, *Journal of theoretical and applied physics* **2012**, 6, 1.

[113] K. Morigaki, S. Kugler, K. Shimakawa, *Amorphous Semiconductors: Structural, Optical, and Electronic Properties*, John Wiley & Sons, **2017**.

[114] I. G. Austin, N. F. Mott, *Polarons in crystalline and non-crystalline materials*, **1969**.

[115] A. Miller, E. Abrahams, *Physical Review* **1960**, 120, 745.

[116] N. F. Mott, *Philosophical Magazine* **1969**, 19, 835.

[117] P. N. Murgatroyd, *Journal of Physics D: Applied Physics* **1970**, 3, 151.

References

[118] S. Mendiratta, M. Usman, K.-L. Lu, *Coordination Chemistry Reviews* **2018**, 360, 77.

[119] D. P. Karim, A. T. Aldred, *Physical Review B* **1979**, 20, 2255.

[120] A. K. Jonscher, *Journal of Non-Crystalline Solids* **1972**, 8-10, 293.

[121] J. Veres, S. D. Ogier, S. W. Leeming, D. C. Cupertino, S. Mohialdin Khaffaf, *Advanced Functional Materials* **2003**, 13, 199.

[122] F. Verstraeten, S. Gielen, P. Verstappen, J. Raymakers, H. Penxten, L. Lutsen, K. Vandewal, W. Maes, *Journal of Materials Chemistry C* **2020**, 8, 10098.

[123] G. Konstantatos, I. Howard, A. Fischer, S. Hoogland, J. Clifford, E. Klem, L. Levina, E. H. Sargent, *Nature* **2006**, 442, 180.

[124] F. Verstraeten, S. Gielen, P. Verstappen, J. Kesters, E. Georgitzikis, J. Raymakers, D. Cheyns, P. Malinowski, M. Daenen, L. Lutsen, K. Vandewal, W. Maes, *Journal of Materials Chemistry C* **2018**, 6, 11645.

[125] D. Lackner, O. J. Pitts, S. Najmi, P. Sandhu, K. L. Kavanagh, A. Yang, M. Steger, M. L. W. Thewalt, Y. Wang, D. W. McComb, C. R. Bolognesi, S. P. Watkins, *Journal of Crystal Growth* **2009**, 311, 3563.

[126] H. Fang, W. Hu, *Advanced Science* **2017**, 4, 1700323.

[127] T.-H. Fang, W.-J. Chang, C.-M. Lin, *Microelectronic engineering* **2005**, 77, 389.

[128] M. Faghihnasiri, M. Izadifard, M. E. Ghazi, *The Journal of Physical Chemistry C* **2017**, 121, 27059.

[129] S. Bertolazzi, J. Brivio, A. Kis, *ACS nano* **2011**, 5, 9703.

[130] J.-W. Jiang, J.-S. Wang, B. Li, *Physical Review B* **2009**, 80, 113405.

[131] S. E. Root, S. Savagatrup, A. D. Printz, D. Rodriquez, D. J. Lipomi, *Chemical Reviews* **2017**, 117, 6467.

[132] N. Duan, Y. Li, H.-C. Chiang, J. Chen, W.-Q. Pan, Y.-X. Zhou, Y.-C. Chien, Y.-H. He, K.-H. Xue, G. Liu, T.-C. Chang, X.-S. Miao, *Nanoscale* **2019**, 11, 17590.

[133] S. Seo, S.-H. Jo, S. Kim, J. Shim, S. Oh, J.-H. Kim, K. Heo, J.-W. Choi, C. Choi, S. Oh, D. Kuzum, H. S. P. Wong, J.-H. Park, *Nature Communications* **2018**, 9, 5106.

[134] a) Y. van de Burgt, E. Lubberman, E. J. Fuller, S. T. Keene, G. C. Faria, S. Agarwal, M. J. Marinella, A. Alec Talin, A. Salleo, *Nature Materials* **2017**, 16, 414; b) E. J. Fuller, F. E. Gabaly, F. Léonard, S. Agarwal, S. J. Plimpton, R. B. Jacobs-Gedrim, C. D. James, M. J. Marinella, A. A. Talin, *Advanced Materials* **2017**, 29, 1604310; c) B.-W. Yao, J. Li, X.-D. Chen, M.-X. Yu, Z.-C. Zhang, Y. Li, T.-B. Lu, J. Zhang, *Advanced Functional Materials* **2021**, 31, 2100069; d) W. Xiao, L. Shan, H. Zhang, Y. Fu, Y. Zhao, D. Yang, C. Jiao, G. Sun, Q. Wang, D. He, *Nanoscale* **2021**, 13, 2502.

[135] S. Lv, W. Gao, C. Ran, D. Li, L. Chao, X. Wang, L. Song, Z. Lin, L. Fu, Y. Chen, *Sol. RRL* **2021**, 5, 2100675.

[136] J. Tong, J. Gong, M. Hu, S. K. Yadavalli, Z. Dai, F. Zhang, C. Xiao, J. Hao, M. Yang, M. A. Anderson, E. L. Ratcliff, J. J. Berry, N. P. Padture, Y. Zhou, K. Zhu, *Matter* **2021**, 4, 1365.

[137] Z. Yang, A. Rajagopal, A. K. Y. Jen, *Adv. Mater.* **2017**, 29, 1704418.

[138] M. T. Klug, R. L. Milot, J. B. Patel, T. Green, H. C. Sansom, M. D. Farrar, A. J. Ramadan, S. Martani, Z. Wang, B. Wenger, J. M. Ball, L. Langshaw, A. Petrozza, M. B. Johnston, L. M. Herz, H. J. Snaith, *Energy Environ. Sci.* **2020**, 13, 1776.

[139] Z. Liang, H. Xu, Y. Zhang, G. Liu, S. Chu, Y. Tao, X. Xu, S. Xu, L. Zhang, X. Chen, B. Xu, Z. Xiao, X. Pan, J. Ye, *Adv. Mater.* **2022**, 34, 2110241.

[140] Z. Xiao, Z. Song, Y. Yan, *Adv. Mater.* **2019**, 31, 1803792.

[141] a) T. J. Smart, H. Takenaka, T. A. Pham, L. Z. Tan, J. Z. Zhang, T. Ogitsu, Y. Ping, *J. Phys. Chem. Lett.* **2021**, 12, 6299; b) Y. Liu, W. Gao, C. Ran, H. Dong, N. Sun, X. Ran, Y. Xia, L. Song, Y. Chen, W. Huang, *ChemSusChem* **2020**, 13, 6477.

[142] G. Xu, P. Bi, S. Wang, R. Xue, J. Zhang, H. Chen, W. Chen, X. Hao, Y. Li, Y. Li, *Adv. Funct. Mater.* **2018**, 28, 1804427.

[143] V. D. Mote, Y. Purushotham, B. N. Dole, *Journal of Theoretical and Applied Physics* **2012**, 6, 6.

[144] a) D. J. Lim, N. A. Marks, M. R. Rowles, *Carbon* **2020**, 162, 475; b) H. Kafashan, *Journal of Electronic Materials* **2019**, 48, 1294; c) P. Scherrer, *Gott. Nachr Math. Phys* **1918**, 2, 98.

[145] P. Giannozzi, S. Baroni, N. Bonini, M. Calandra, R. Car, C. Cavazzoni, D. Ceresoli, G. L. Chiarotti, M. Cococcioni, I. Dabo, *Journal of Physics: Condensed Matter* **2009**, 21, 395502.

[146] J. P. Perdew, K. Burke, M. Ernzerhof, *Physical Review Letters* **1996**, 77, 3865.

[147] P. T. Nguyen, J. Di Rocco, R. Rubei, D. Di Ruscio, presented at 2018 44th Euromicro conference on software engineering and advanced applications (SEAA) **2018**.

[148] S. Agarwal, S. J. Plimpton, D. R. Hughart, A. H. Hsia, I. Richter, J. A. Cox, C. D. James, M. J. Marinella, presented at 2016 International Joint Conference on Neural Networks (IJCNN) **2016**.

[149] C. Wang, P. Cheng, Y. Yao, Y. Yamauchi, X. Yan, J. Li, J. Na, *Journal of hazardous materials* **2020**, 392, 122164.

References

[150] C. Xie, C.-k. Liu, H.-l. Loi, F. Yan, **2019**, 30, 1903907.

[151] N. Aristidou, I. Sanchez-Molina, T. Chotchuangchutchaval, M. Brown, L. Martinez, T. Rath, S. A. Haque, in *Angewandte Chemie International Edition*, Vol. 54, 2015, 8208.

[152] a) S. Li, C. Wang, Y. Yin, E. Lewis, P. Wang, *Nanophotonics* **2020**, 9, 1743; b) X. Zhou, X. Hu, J. Yu, S. Liu, Z. Shu, Q. Zhang, H. Li, Y. Ma, H. Xu, T. Zhai, *Advanced Functional Materials* **2018**, 28, 1706587.

[153] Y. Liu, S. Li, L. Dai, J. Li, J. Lv, Z. Zhu, A. Yin, P. Li, B. Wang, *Angewandte Chemie* **2021**, 133, 16545.

[154] J. Li, Z. Sun, F. Yan, *Advanced Materials* **2012**, 24, 88.

[155] M. Zirkl, B. Stadlober, G. Leising, *Ferroelectrics* **2007**, 353, 173.

[156] M. V. Fischetti, D. A. Neumayer, E. A. Cartier, *Journal of Applied Physics* **2001**, 90, 4587.

[157] Y. Wang, X. Huang, T. Li, L. Li, X. Guo, P. Jiang, *Chemistry of Materials* **2019**, 31, 2212.